

Summer 9-2014

Ion-Cyclotron Resonance Heating of O⁺ in the Topside Ionosphere and Mapping Outflows to the Magnetosphere

Anthony W. Pritchard
Embry-Riddle Aeronautical University

Follow this and additional works at: <https://commons.erau.edu/edt>



Part of the [Atmospheric Sciences Commons](#), and the [Engineering Physics Commons](#)

Scholarly Commons Citation

Pritchard, Anthony W., "Ion-Cyclotron Resonance Heating of O⁺ in the Topside Ionosphere and Mapping Outflows to the Magnetosphere" (2014). *Doctoral Dissertations and Master's Theses*. 234.
<https://commons.erau.edu/edt/234>

This Thesis - Open Access is brought to you for free and open access by Scholarly Commons. It has been accepted for inclusion in Doctoral Dissertations and Master's Theses by an authorized administrator of Scholarly Commons. For more information, please contact commons@erau.edu.

ION-CYCLOTRON RESONANCE HEATING OF O⁺ IN THE
TOPSIDE IONOSPHERE AND MAPPING OUTFLOWS TO THE
MAGNETOSPHERE

BY
ANTHONY W. PRITCHARD

A Thesis
Submitted to the Department of Physical Sciences
and the Committee on Graduate Studies
In partial fulfillment of the requirements
for the degree of
Master in Science in Engineering Physics

09/2014
Embry-Riddle Aeronautical University
Daytona Beach, Florida

© Copyright by Anthony W. Pritchard 2014
All Rights Reserved

ION-CYCLOTRON RESONANCE HEATING OF O⁺ IN THE
TOPSIDE IONOSPHERE AND MAPPING OUTFLOWS TO THE
MAGNETOSPHERE

by
Anthony W. Pritchard

This thesis was prepared under the direction of the candidate's Thesis Committee Chair, Dr. Matthew Zettergren, Assistant Professor, Daytona Beach Campus, and Thesis Committee Members Dr. John Hughes, Associate Professor, Daytona Beach Campus, and Dr. Jonathan Snively, Assistant Professor, Daytona Beach Campus, and has been approved by the Thesis Committee. It was submitted to the Department of Physical Sciences in partial fulfillment of the requirements for

the degree of
Master of Science in Engineering Physics

THESIS COMMITTEE:




Dr. Matthew Zettergren,
Committee Chair




Dr. John Hughes,
Committee Member




Dr. Jonathan Snively,
Committee Member




Dr. Peter Erdman,
Graduated Program Chair,
Engineering Physics



Dr. Terry Oswalt,
Department Chair,
Physical Sciences



Dr. William Grams,
Dean, College of Arts and Sciences



Dr. Robert Oxley,
Associate V.P. for Academics

Abstract

This thesis considers the heavy ion dynamics due to ion-cyclotron resonance energization processes that take place in the turbulent region of the Earth's topside, high latitude ionosphere. We simulate the impact of this transverse heating process upon energies and velocity distribution functions of outflowing oxygen ions (O^+) in the approximate altitude range of 800 km to 15,000 km. To do so most effectively, we use a single particle tracing model that precisely reproduces the small-scale wave-particle interaction of broadband extremely low frequency (BBELF) waves with the ions' cyclotron motions, leading to the upward acceleration of ions in type-II ion outflows and ion conics. Instead of employing the guiding center approximation, as is usually done with single particle tracing models in order to make the outflow simulation less computationally expensive, the trajectories here resolve the ions' full gyro-motion. The model's uncustomary approach is validated by its ability to contribute statistical results via Monte Carlo simulation which reflect, at least qualitatively, previous observations of transversely energized distribution functions—ion conics. The effects of parallel potential drops and coherent energization upon the distribution functions are also examined.

In addition to the above result which uses a simple dipole Earth magnetic field to recreate expected ion conic distribution functions, an adaptation of the model is used to map the trajectories of transversely energized O^+ ions throughout a realistic NASA: BATSRUS Earth magnetosphere in order to determine probabilistic magnetospheric destinations and escape likelihood for the ions. A multiple-particle tracing technique is employed to qualitatively demonstrate the potential of this model for investigating sources and fates of ion outflows. The use of NASA:

CCMC's Kameleon tool to interface with BATSRUS magnetosphere model output resulted in the production of a versatile model that can be used with many CCMC magnetospheric or heliospheric models, with a current specialization for examining the large scale effects of this small-scale resonance energization process in the topside ionosphere and above. The tracer can therefore easily be adapted to other regions of the Earth's magnetosphere and ionosphere, other planets, or the heliosphere.

Acknowledgments

I could not have completed this degree without the invaluable assistance and direction provided to me by Dr. Zettergren throughout the entire endeavor. A special thanks to Dr. Hughes and to Dr. Snively for their time and interest in my project. A big thank you to Dr. Nykyri for her help and support. The model owes its origins to Dr. Liu and his Numerical Methods final project. Meghan Burleigh has helped me endlessly to see this project through to its end. Thanks to Bryan Wright for taking on the degrees' challenges with me throughout our time at ERAU. A thank you to Dave McCall and William Merritt for their selflessness. Thanks to Brian Walsh for his particle tracing advice. A special thanks to Justin Bozzelli and to Dave Shideler for their generosity. Most of all, I want to thank my family for believing in me: thanks to DJ Pritchard for his guidance, Tammy Hane for her care, Dave Pritchard for his motivation, Will Bortz for his brotherhood, Carol Otto for the life and love, and Terri Rutkiewicz and the Rutkiewicz crew for their constant support.

Contents

Abstract	iv
Acknowledgments	vi
1 Introduction	1
2 Particle Tracer Concept	7
2.0.1 Developing the Basic Equations of Motion	9
2.0.2 Numerical Integrator	11
2.0.3 Parallelization	14
2.1 Dipole Earth Magnetic Field	15
2.1.1 Field Line Display	16
2.1.2 Dipole Coordinate System	16
2.2 CCMC: BATSRUS Magnetic Field	19
2.3 Electric Field Environment	22
2.3.1 Transverse Electric Wave Field	22
2.3.2 Field-Aligned Potential Drops	30
2.4 Final Equations of Motion and a Comparison to Guiding Center Equations of Motion	31
2.4.1 Final Equations of Motion	31
2.4.2 Comparison to the Guiding Center Approximation	32
3 Model Validation and Configuration	38
3.1 Model Validation	38

3.2	Configuration	44
4	Results: Mapping to the Magnetosphere	51
4.1	Presentation of Ionosphere-Magnetosphere Coupling Trajectories . .	52
5	Results: Monte Carlo Simulations	59
5.1	Detail in Highly Non-Maxwellian Velocity Distributions	61
5.2	Ion Conics Resulting from Incoherent Transverse Energization	67
6	Conclusions and Future Work	82
6.1	Conclusions	82
6.1.1	Trajectory Mapping	83
6.1.2	Distribution Functions	83
6.2	Future Work	85

List of Tables

2.1	Power Spectral Density Reference Values	26
5.1	List of Cases. Note that cases not displayed in a figure but mentioned in the text, such as the case of fully coherent energization, are not listed here.	61

List of Figures

1.1	Qualitative display of a transversely heated ion conic [Chang, 1991]. The boldface arrows point in the direction of the mirror force which results from the non-thermal transverse velocity and the gradient in the magnetic field strength. The mirror force acts to convert transverse energy to parallel energy and move the distribution upward towards the weaker magnetic field in attempt to maintain the first adiabatic invariant.	3
1.2	[Moore and Horwitz, 2007] Representation of the Earth’s magnetosphere and some possible ionospheric outflow destinations (represented by gray arrows). The outflows have been energized above the gravitational escape energy. The gray region is terrestrial plasma.	5
1.3	[Zettergren et al., 2013] Representation of the ion escape causal chain. Type-I, Joule-heated upflows at lower altitudes raise the ionosphere to altitudes susceptible to transverse heating. The mirror force further elevates these transversely heated ions in type-II outflows. The auroral acceleration region (AAR) represents upwardly oriented, field-aligned potentials that often further accelerate outflows above gravitational escape energy.	6
2.1	Display of the Earth and its dipole magnetic field lines. This figure displays the visual model’s flexibility.	17
2.2	Dipole coordinate system unit vectors	18

2.3	SWX2 visualization of BATSRUS Global Magnetosphere plasma velocity and magnetic field during the geomagnetic storm on April 5, 2010. The streamlines represent the orientation of the Earth's magnetic field, and the color contours represent the x -component of velocity. Grey lines are open geomagnetic field lines, red lines are closed, and yellow lines are the interplanetary magnetic field. The configuration of the magnetic field and the plasma velocity suggests a recent plasmoid ejection from the magnetotail. The K_p index reached 5 during this time, and the geomagnetic storm eventually reached a $K_p = 8$	21
3.1	This is a demonstration of the expected gyro, bouncing, and drift motion that would occur for a non-heated proton in a simple dipole geomagnetic field after 1 hr 7 min with the initial conditions $x_0 = -2.3 R_E$, $y_0 = -3.3 R_E$, $z_0 = 0.55 R_E$, $v_{x0} = v_{y0} = 250 \text{ km s}^{-1}$, and $v_{z0} = 17.8 \text{ km s}^{-1}$. The trajectory drifts from east to west, as expected with the proton. The gyro-motion is counter-clockwise if viewed from below, as expected. A few of the trajectories seen here can actually be seen spiraling about a magnetic field line.	39
3.2	The expected $\vec{E} \times \vec{B}$ drift for an O^+ ion in a constant, uniform magnetic field $\vec{B} = B_z \hat{z}$ and a perpendicular, constant, uniform electric field $ \vec{E} = E_x \hat{x} $. This is the case corresponding to Equation 3.1. The numerical solution uses time-steps that are 1/200 of a gyro-period for these validation cases.	41
3.3	The numerical error after 10 min of tracing using different fractions of the gyro-period for the first case described above and in Figure 3.2	42
3.4	The expected increase in Larmor radius for an O^+ ion in a magnetic field of $\vec{B} = B_z \hat{z}$ and a resonant, LHCP electric field of $\vec{E} = E_x \cos(\Omega_c t) \hat{x} - E_y \sin(\Omega_c t) \hat{y}$. This is the case corresponding to Equation 3.2 with E_z set to zero. The numerical solution uses time-steps that are 1/200 of a gyro-period.	44

3.5	The numerical error after 10 min of tracing using different fractions of the gyro-period for the second case described above and in Figure 3.4.	45
3.6	The expected trajectory of an O^+ ion in a magnetic field of $\vec{B}=B_z\hat{z}$, a resonant, LHCP electric field of $\vec{E} = E_x \cos(\Omega_c t)\hat{x} - E_y \sin(\Omega_c t)\hat{y}$, and constant field-aligned potential $E_z\hat{z}$. This is the case corresponding to Equation 3.2. The numerical solution uses time-steps that are 1/200 of a gyro-period.	46
3.7	The numerical error after 10 min of tracing using different fractions of the gyro-period for the third case described above and in Figure 3.6. Interestingly, this case that has the most terms in the analytical solution has the smallest error of the three cases (although all cases have good error).	47
3.8	Mirror point of an incoherent transversely energized oxygen ion with $E_0^2=10^{-1} \text{ V}^2 \text{ m}^{-2} \text{ Hz}^{-1}$ at an altitude of 1050 km, geographic latitude and longitude 74.9° and 0° , and velocity components $v_{x0}=250 \text{ m s}^{-1}$, $v_{y0}=-300 \text{ m s}^{-1}$, and $v_{z0}=-1 \text{ km s}^{-1}$	48
3.9	Properties of an incoherent transversely heated O^+ ion which leaves the realistic heating region after 13 min. A particle with the same initial conditions reached a peak altitude of $31.4 R_E$ after 2.3 days, and followed the field line back to the southern latitude Earth ionosphere (-75.8°) at 100 km altitude after 4.5 days. Notice the magnetic moment is not constant until the ion leaves the non-adiabatic heating region.	49

4.1	Initial (blue) and final (red) ion positions are displayed here for a study which was used to pinpoint the initialization region boundaries that are most conducive to the production of high energy outflows for the main simulation. Longitude boundaries of this preliminary trace are 192° to 268° (GSM), with geographic latitude boundaries 63.5° to 81.5° , and initial altitudes of 1000 km to 1200 km. The location resulting in the highest final altitudes here were 73.3° to 73.6° latitude and about 231° to 239° longitude.	53
4.2	(Main ion mapping simulation) Spatial visual display of transversely heated outflow trajectories in a BATSRUS magnetosphere mapped throughout a geomagnetic storm which occurred on April 5, 2010. The outflowing ions would continue to the end of the BATSRUS magnetosphere through the north boundary at an altitude near $175 R_E$ if traced further, because of the unusual magnetospheric configuration during this snapshot (see Figure 2.3).	55
4.3	(Main ion mapping simulation) Final ion positions are plotted in this visual display. The field lines shown are not representative of the BATSRUS magnetosphere, but rather serve to display the negative longitudinal curve the outflow follows throughout the magnetosphere (the blue circles are marginally visible).	56
4.4	(Main ion mapping simulation) Relationship of final geographic latitude and GSM longitude with respect to altitude.	57
4.5	(Main ion mapping simulation) Probability of altitude destination for 2280 outflowing O^+ ions during the geomagnetic storm on April 5, 2010. Note again that trajectories were stopped once an altitude of $50 R_E$ was attained. This figure reflects the simulation's purpose to determine probability of ionospheric oxygen ion escape to the magnetosphere due to transverse energization.	58

- 5.1 Case 1. Demonstration of the model’s ability to produce highly detailed, non-Maxwellian distribution functions. The above 15 snapshots in time show the initial development of distribution functions due to partially coherent transverse energization ($\epsilon = \pm \pi/2$ rad) for a simulation of about 2,150,000 particles that are initialized from 1000 to 1750 km and traced for 1 min. The color axis represents the number of particles in each velocity bin. The transverse electric field spectral density reference value $E_0^2 = 2 \times 10^{-5} \text{ V}^2 \text{ m}^{-2} \text{ Hz}^{-1}$ 63
- 5.2 Case 1. Full conic development for the partially coherent case. The above 12 snapshots in time increase in time and in altitude from right-to-left, bottom-to-top. The simulation traced about 150,000 particles that are initialized from 1000 to 1750 km and traced for 25 min (there are many less particles in this simulation than in the last run because of the long runtime used in this particular run). The color axis represents the logarithm of the number of particles in each velocity bin. The transverse electric field spectral density reference value $E_0^2 = 2 \times 10^{-5} \text{ V}^2 \text{ m}^{-2} \text{ Hz}^{-1}$ 64
- 5.3 Case 2. Counterstreaming distribution functions resulting from a downward, parallel potential drop of magnitude $0.00667 \text{ mV m}^{-1}$ from 3000 km to 6000 km combined with partially coherent transverse energization (electric field wave phase $\epsilon = \pm \pi/2$ rad) for a simulation of over 250,000 particles that are initialized from 1000 to 1750 km and traced for 18 min. The color axis represents the logarithm of the number of particles in each velocity bin. The transverse electric field spectral density reference value $E_0^2 = 2 \times 10^{-5} \text{ V}^2 \text{ m}^{-2} \text{ Hz}^{-1}$ 66
- 5.4 Case 3. Incoherent transverse energization of about 300,000 particles initialized from 1000 to 8000 km after 25 min. The color axis represents the logarithm of the number of particles in each velocity bin. The altitude slices are increasing from right-to-left, bottom-to-top. The spectral density reference value $E_0^2 = 2 \times 10^{-4} \text{ V}^2 \text{ m}^{-2} \text{ Hz}^{-1}$. . . 69

5.5	Case 4. Incoherent transverse energization of about 300,000 particles initialized from 1000 to 8000 km after 25 min. The color axis represents the logarithm of the number of particles in each velocity bin. The spectral density reference value $E_0^2 = 3 \times 10^{-5} \text{ V}^2 \text{ m}^{-2} \text{ Hz}^{-1}$ (a magnitude smaller than the previous case).	70
5.6	Case 4. Average particle energy at each time-step for the simulation corresponding to that shown in Figure 5.5. The energizing electric field is turned off after 18 min.	72
5.7	Case 5. Conic development and bulk motion which result from fully incoherent energization of about 100,000 particles that are now initialized from 1000 km to 1750 km with $E_0^2 = 2 \times 10^{-4} \text{ V}^2 \text{ m}^{-2} \text{ Hz}^{-1}$ at $t = 5$ min (left) and $t = 15$ min (right). The color axis represents the logarithm of the number of particles in each velocity bin.	74
5.8	Case 6. Lower energy conic development and bulk motion which result from fully incoherent energization of about 250,000 particles initialized from 1000 km to 1750 km with $E_0^2 = 5 \times 10^{-5} \text{ V}^2 \text{ m}^{-2} \text{ Hz}^{-1}$ (a magnitude smaller than the previous case) at $t = 1.75$ min (left) and $t = 10$ min (right). The color axis represents the logarithm of the number of particles in each velocity bin. This figure serves to show what happens to the lower energy tail of the distribution function at lower altitudes.	75
5.9	Case 7. The above four snapshots in time show the development of distribution functions due to incoherent transverse energization and a downward, gradual parallel potential drop of 0.0067 mV m^{-1} applied over the range of 3000 to 6000 km for a simulation of over 300,000 particles that are initialized from 1000 to 8000 km and traced for 25 min. The color axis represents the logarithm of the number of particles in each velocity bin. The spectral density reference value $E_0^2 = 3 \times 10^{-5} \text{ V}^2 \text{ m}^{-2} \text{ Hz}^{-1}$	79

5.10	Case 7. Average particle energy at each time-step for the simulation corresponding to that shown in Figure 5.9. The energizing electric field is turned off after 18 min.	80
5.11	Case 8. The above five snapshots in time show the development of distribution functions due to incoherent transverse energization and an upward parallel potential pulse of 10 mV m^{-1} applied for 10 ms [Singh and Chan, 1993] for a simulation of nearly 200,000 particles that are initialized from 1000 to 1750 km and traced for 20 min. The color axis represents the logarithm of the number of particles in each velocity bin. The transverse electric field spectral density reference value $E_0^2 = 5 \times 10^{-5} \text{ V}^2 \text{ m}^{-2} \text{ Hz}^{-1}$	81

Chapter 1

Introduction

An ongoing forefront of mankind's collective effort to understand the physics governing the dynamics of his surrounding environment is that of the fluctuating magnetic shield that protects the Earth and its organisms from the sun's energetic barrage of solar wind known as the ionosphere-magnetosphere system. The historical mysteries brought upon by phenomena such as the brilliant displays of the aurora and the dancing of a compass needle has sprung a chain of scientific progress which has propelled our knowledge to a current position wherein only the minor details in the description of the behavior of the magnetic shelter remain. Space physics has achieved this description of magnetospheric dynamics by means of obtaining and correlating observations with theory via physical models. Among the numerous processes and subsets of processes varying predictably in time and space throughout the Earth's space environment, a particularly crucial branch of study concerns the coupling of ionospheric plasma to magnetospheric plasma. Certain processes accelerate the supply of plasma from the ionosphere to the magnetosphere. In the high latitude, dayside cusp and cleft regions and the nightside polar cap boundary (PCB), magnetic turbulence resulting from plasma flow of both solar and ionospheric origin contributes to global changes in magnetospheric configuration and ion composition. These changes dictate how the Earth's protective plasma environment will behave as a whole electromagnetically and are for this reason important topics of study. An essential research topic is ionospheric

ion outflow. In particular, a prominent energization mechanism is wave-particle interaction that occurs between ionospheric plasma and electromagnetic waves in locations of magnetospheric turbulence. This non-thermal plasma acceleration process referred to as ion-cyclotron resonance results in significant mass outflows that have velocity distributions that are not conveniently predicted by global magnetosphere models. It has therefore been a necessity for recent global MHD models to incorporate more realistic ionosphere-magnetosphere coupling by using kinetic simulations at the lower boundary [Winglee, 1999, Wu et al., 2002].

To this end, this thesis considers a kinetic solution to simulate the effects of ion-cyclotron resonance that is known to produce significant ionospheric oxygen ion (O^+) outflows (other acceleration mechanisms such as field-aligned electric potentials are also briefly explored). Particularly, broadband extremely low frequency (BBELF) waves can accelerate O^+ in the approximate region from 1000 to 15,000 km altitude at auroral latitudes (e.g., Bouhram et al. [2002]). The gyrofrequency of O^+ in this region can match the frequency of oscillation of the transverse component of the BBELF electric wave field, which ranges approximately from a few hertz to hundreds of hertz [Knudsen et al., 1998] and is the most common wave in the auroral region [Hamrin et al., 2002]. Observations suggest that about 90% of O^+ transverse heating events are due to BBELF resonance, and 95% of all O^+ outflows are associated with the BBELF field [Norqvist et al., 1998]. Yet, the energization process is not readily incorporated into ionospheric or magnetospheric models due to the suprathermal heating caused by this small-scale wave-particle interaction process. For this reason, the main results of this study obtain velocity distribution functions via a fully kinetic, single particle tracing technique. A single particle tracing model is able to replicate the small-scale energization process and therefore has the capability to predict the non-Maxwellian structures of the resulting distribution functions. These structures in velocity space are referred to as ion conics and are characterized by extended lobes in the transverse direction and a narrow but energetic extent in the field-aligned direction (see Figure 1.1).

Another useful application of the single particle model is its ability to track particular ions which have been energized out to their magnetospheric destination.

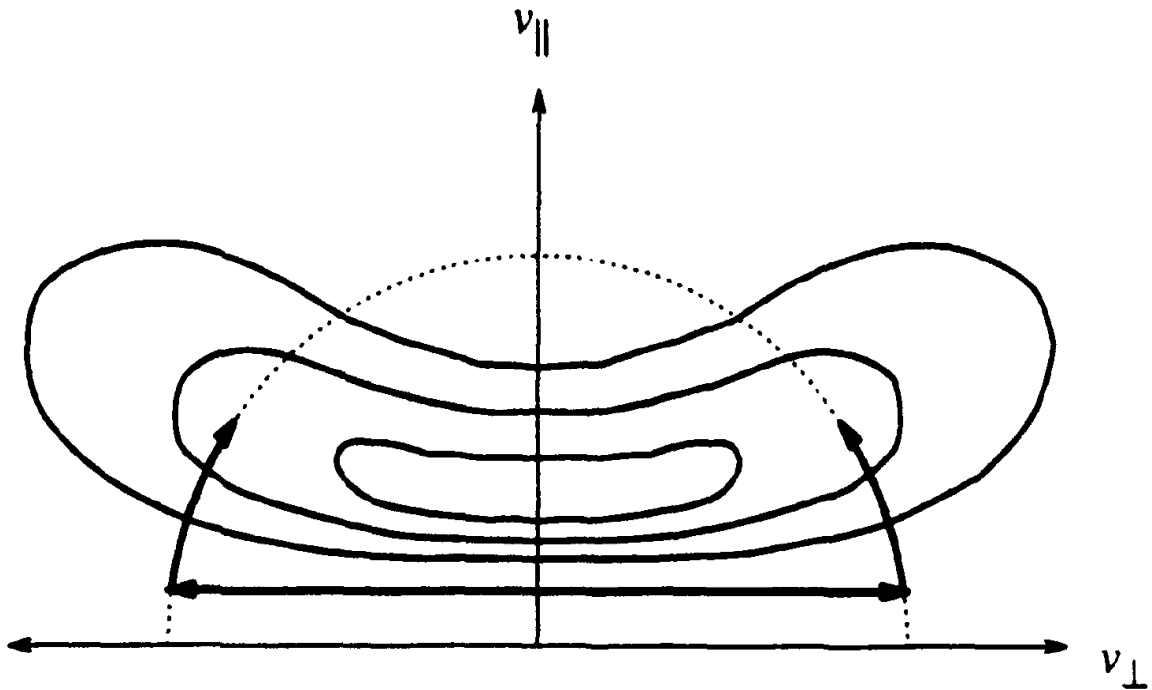


Figure 1.1: Qualitative display of a transversely heated ion conic [Chang, 1991]. The boldface arrows point in the direction of the mirror force which results from the non-thermal transverse velocity and the gradient in the magnetic field strength. The mirror force acts to convert transverse energy to parallel energy and move the distribution upward towards the weaker magnetic field in attempt to maintain the first adiabatic invariant.

This kind of model therefore allows us to correlate source regions and energization processes to their effects upon regional composition in the magnetosphere. It is not possible to accurately model the spatiotemporal dynamics of the magnetosphere without the knowledge of source locations of ions for the different magnetospheric regions. It has been a consensus for a few decades that the ionosphere is at least a significant source of magnetospheric plasma and even the principal source, at times [Chappell et al., 1981]. In particular, O^+ must originate in the ionosphere

because the solar wind does not contain much of this heavy ion. Then, upon consideration that O^+ is sometimes the dominant ion in regions such as the plasma sheet, the ionosphere is the best explanation for their source [Chang et al., 1986, Kintner et al., 1996]. O^+ has been observed in many other regions of the magnetosphere, including the magnetotail lobe, magnetotail, cusp, plasma mantle, and also in the magnetopause [Ebihara et al., 2006]. Another important motivation to map the ion outflows to the magnetosphere is the role of the presence of O^+ upon slowing the rate of magnetic reconnection in the magnetotail [Baker et al., 1982].

Note that the thesis endeavor was dedicated mainly to the ground-up development of a sound, efficient particle tracing model that imposes a novel, physical application of this transverse energization process upon a realistic initial distribution of O^+ ions. Therefore, the description of the model's development and the definition of future goals for this new model are main components of this thesis document. The results portion of the study, then, serves to demonstrate qualitative results which generally align with expectations using the model.

In the following chapters of this thesis, the details of the single particle model are documented, and its capabilities are showcased. Chapter 2 serves to fully describe the physical and numerical theory governing the particle tracing model; the functionality of the model is given an explanation via the full development of the final equations of motion for the test particles. The third chapter provides model validation experiments and an overview of the configuration of the simulation region. In Chapter 4, this study's preliminary results which display the function of the adaptation of the model which maps ions to a realistic magnetosphere are presented. Chapter 5 exhibits the main results of the study with the presentation of ion conic distribution functions (as well counterstreaming distribution functions caused by a downward parallel potential) and their dynamic tendencies in different electromagnetic environments. Chapter 6 suggests some main conclusions that can be drawn from the effort in totality, and it lists future plans and potential applications of the model.

The following figures provide illustrations of the outflow processes of concern. Figure 1.3 serves to distinguish between type-I verses type-II outflows with the

ion escape causal chain.

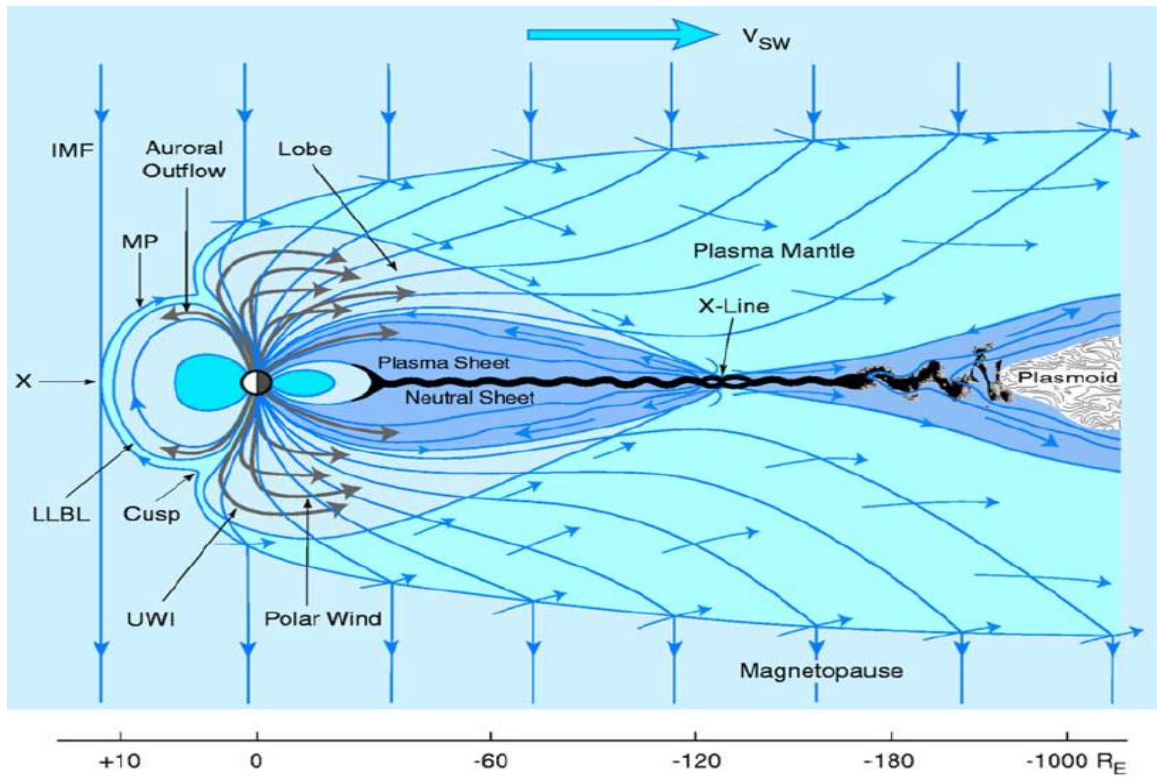


Figure 1.2: [Moore and Horwitz, 2007] Representation of the Earth's magnetosphere and some possible ionospheric outflow destinations (represented by gray arrows). The outflows have been energized above the gravitational escape energy. The gray region is terrestrial plasma.

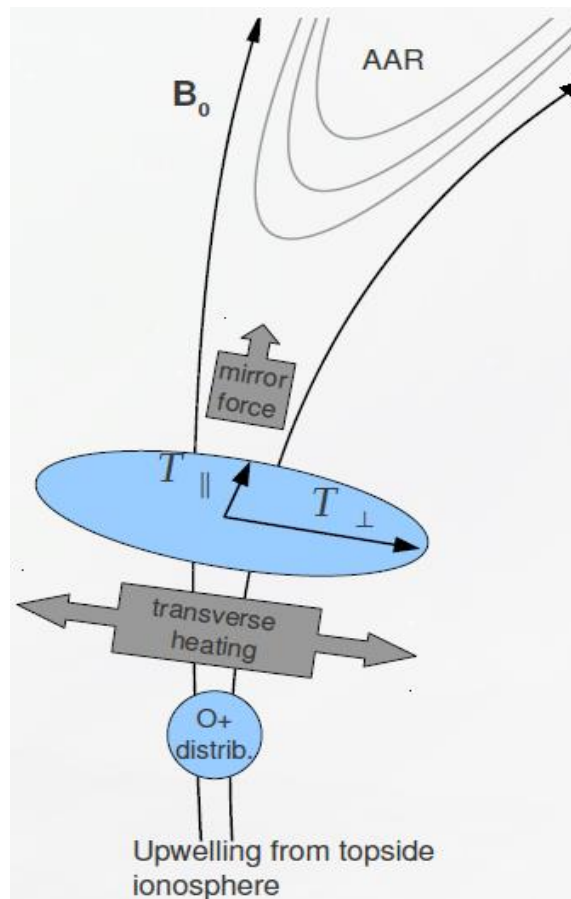


Figure 1.3: [Zettergren et al., 2013] Representation of the ion escape causal chain. Type-I, Joule-heated upflows at lower altitudes raise the ionosphere to altitudes susceptible to transverse heating. The mirror force further elevates these transversely heated ions in type-II outflows. The auroral acceleration region (AAR) represents upwardly oriented, field-aligned potentials that often further accelerate outflows above gravitational escape energy.

Chapter 2

Particle Tracer Concept

The Monte Carlo particle tracing model is an originally created body of code written in Fortran 90 and specialized for this thesis's purpose of reproducing distribution functions of typical type-II O^+ outflows in the high latitude ionosphere which occur during turbulent periods such as geomagnetic storms, substorms, electron precipitation and (most often) auroral arc events due to transverse energization by BBELF waves. Type-II outflows are distinguished from type-I, Joule-heated upflows by their characteristic non-thermal heating mechanisms [Hultqvist et al., 1999]. It is a non-self-consistent kinetic model which uses stochastically generated transverse heating. The heating is reproduced by the addition into the equation of motion a left-handed, circularly polarized (LHCP) electric field wave with a frequency matching the ions' gyrofrequency, but with a randomly generated phase.

The parallelized numerical integrator solves the kinetic equations of motion in tandem for an initial exponentially decaying (with altitude) distribution of particles immersed in an environment replicating the electromagnetics of the Earth's magnetosphere-ionosphere lower cusp or its polar cap boundary (PCB) region, where these type-II outflows are known to frequently occur. The simulation region in the main portion of the study extends from 800 km to 3-4 R_E altitude, while the heating region has boundaries at 1000 km and 10,000 km as well as geographic latitudinal boundaries between 72° and 75° (the use of geomagnetic latitude and

magnetic local time will be implemented into the model in future work). This heating range corresponds to a typically used BBELF altitudinal extent. For example, Zeng et al. [2006] and Wu et al. [1999] both use a BBELF heating region ranging from 1600 km to $2 R_E$.

A single particle tracing model has the advantage of being able to precisely reproduce small-scale plasma phenomena with minimal simplification or empirical relationships. The obvious price of this advantage is computational costliness. With efficiently designed coding mechanisms and parallelized computing processes carried out in the fast execution environment of Fortran, a statistical, single macroparticle tracer approach can be used to simulate realistic transversely energized velocity distribution functions. When effectively extrapolated to the large scale, these sharply defined distribution functions can be used in conjunction with more macroscopic, fluid moment-based models (e.g. dynamic fluid-kinetic models [Winglee, 1999, Wu et al., 1999, 2002, Zeng et al., 2006]). Our method is especially valuable concerning the simulation of the effects of this transverse energization process which results in non-thermal velocity distribution functions. The distribution functions are non-Maxwellian due to an absence of the ability of collisions to force the distribution to thermal equilibrium (the collisional to collisionless transition region is usually from around 1500 km to 2500 km [Zeng et al., 2006]). It is therefore not possible for purely moment-based models to predict the non-thermal, non-Maxwellian distribution functions which result from the transverse heating that occurs at collisionless altitudes [Wu et al., 2002]. In addition, the kinetic model has the ability to produce commonly observed counterstreaming distribution functions which result from suprathermal processes such as downward oriented, field-aligned electric fields, whereas large-scale models generally do not have this capability [Singh and Chan, 1993].

It can be noted here that the effects of collisions can optionally be accounted for in the model, but their application has not yet been developed to a level that justifies inclusion in the physical simulation. Presently, we have in place a simple, uniform random number generator which applies impulses of velocity at a specifiable magnitude and frequency. The frequency of collisions decreases with altitude.

Further adaptations of this portion of the code such as a Gaussian number generator and an accurate representation of the collisional magnitude and frequency change with altitude are necessary.

2.0.1 Developing the Basic Equations of Motion

Inherent in the kinetic approach is a mathematical separation of charged particle dynamics and environmental electromagnetic fields. Although self-consistency can be imposed upon the kinetic model, this feature is not implemented in the present study. However, concerning the altitudes of interest, it is an accurate approximation to treat the particles as test particles within an imposed field. This is because the ratio of energized ionospheric plasma to magnetospheric plasma is small. Regions with a relatively higher such ratio require self-consistency due to the primary role that magnetospheric plasma plays in creating the magnitude, shape, and extent of the near-Earth electromagnetic environment [Bouhram et al., 2003].

The objective to find the trajectory of a particle of specifiable mass and charge (as well as an initial velocity and position) embedded in an electromagnetic field environment is simple, in principle. The Lorentz force equation (solved for acceleration) for an ion takes the form:

$$\vec{a} = \frac{q_i}{m_i}(\vec{E} + \vec{v} \times \vec{B})$$

Here, q_i and m_i signify the ion's charge and mass, respectively. In this study, we will examine singly ionized oxygen, O^+ . Therefore, $m_i = m_o = 2.65676 \times 10^{-26}$ kg and $q_i = e = 1.60218 \times 10^{-19}$ C, the elementary charge. The vectors \vec{a} , \vec{v} , \vec{E} , and \vec{B} respectively indicate the particle's acceleration, its velocity, the electric field it experiences, and the Earth's dipole magnetic field. In geocentric Cartesian coordinates, the components of the Lorentz equation are:

$$a_x = \frac{e}{m_o}(E_x + v_y B_z - v_z B_y)$$

$$a_y = \frac{e}{m_o}(E_y + v_z B_x - v_x B_z)$$

$$a_z = \frac{e}{m_o}(E_z + v_x B_y - v_y B_x)$$

The familiar term for gravitational acceleration looks like:

$$\vec{a}_g = \frac{-GM_E}{r^2} \hat{r}$$

with G the gravitational constant ($6.67384 \times 10^{-11} [\frac{m^3}{kg \cdot s^2}]$), M_E the mass of the Earth ($5.97219 \times 10^{24} [kg]$), r the magnitude of the Cartesian position vector, and unit vector

$$\hat{r} = \frac{\vec{r}}{r} = \frac{x}{\sqrt{x^2 + y^2 + z^2}} \hat{x} + \frac{y}{\sqrt{x^2 + y^2 + z^2}} \hat{y} + \frac{z}{\sqrt{x^2 + y^2 + z^2}} \hat{z}.$$

Therefore, adding in gravity, we have:

$$\begin{aligned} a_x &= \frac{e}{m_o}(E_x + v_y B_z - v_z B_y) - \frac{GM_E x}{(x^2 + y^2 + z^2)^{\frac{3}{2}}} \\ a_y &= \frac{e}{m_o}(E_y + v_z B_x - v_x B_z) - \frac{GM_E y}{(x^2 + y^2 + z^2)^{\frac{3}{2}}} \\ a_z &= \frac{e}{m_o}(E_z + v_x B_y - v_y B_x) - \frac{GM_E z}{(x^2 + y^2 + z^2)^{\frac{3}{2}}} \end{aligned} \quad (2.1)$$

In order to arrive at the final equations of motion, the following sections of this chapter will further develop these basic equations of motion by deriving the magnetic dipole coordinate system unit vectors expressed in geocentric Cartesian, adopting an appropriate transverse electric field and parallel electric field, and accounting for plasma motion in the BATSRUS magnetic field adaptation of the model. Firstly, the following two subsections will briefly outline the mechanisms which comprise the numerical model.

2.0.2 Numerical Integrator

The main challenges concerning the numerical method of this integrator were brought upon by the calculation of a particle motion that is chaotic at a miniscule scale, yet gradual on the larger scale of the Earth and its magnetosphere. It follows by logic and by custom that, in order to resolve the gyro-motion, the trajectories must be modeled using a time-step between consecutive calculations which adjusts to always be a specified fraction of the gyro-period. As will be demonstrated during the validation section of Chapter 3, a transversely energized ion has an increasing Larmor radius and gyro-period throughout the resonance process and throughout its upward trek. A study that was performed during the developmental stage of this project was one in which the time-step's optimal fraction of the gyro-period was determined. A convergence study was performed via the comparison of the trajectories calculated using various fractions of a period to a standard trajectory that was produced by the use of a time-step that was one-hundredth of a gyro-period. Accuracy was maintained for a tracing time of twenty minutes with a maximum step of one twentieth of a gyro-period, and therefore the variable $CycleFraction = 0.05$ in the model. The time-step dt is $CycleFraction$ multiplied by the gyro-period:

$$dt = \frac{2\pi m_0}{eB} \times .05 \text{ [s]}$$

The numerical integrator of choice is a Runge-Kutta fourth-order integration scheme. In a future study, this integrator will be compared to other fourth-order, as well as to higher order, Runge-Kutta schemes. Also, a fourth order predictor-corrector scheme should be compared to these.

To calculate the trajectories from the equations of motion, the three second-order ordinary differential equations were broken into six first-order ordinary differential equations. The dot notation signifies a time derivative.

$$\dot{x} = v_x$$

$$\dot{v}_x = \frac{e}{m_o}(E_x + v_y B_z - v_z B_y) - \frac{GM_E x}{(x^2 + y^2 + z^2)^{\frac{3}{2}}}$$

$$\dot{y} = v_y$$

$$\dot{v}_y = \frac{e}{m_o}(E_y + v_z B_x - v_x B_z) - \frac{GM_E y}{(x^2 + y^2 + z^2)^{\frac{3}{2}}}$$

$$\dot{z} = v_z$$

$$\dot{v}_z = \frac{e}{m_o}(E_z + v_x B_y - v_y B_x) - \frac{GM_E z}{(x^2 + y^2 + z^2)^{\frac{3}{2}}}$$

The Runge-Kutta fourth order scheme was carried out via the following process. Given the initial conditions $x_1, y_1, z_1, \dot{x}_1, \dot{y}_1,$ and \dot{z}_1 , the equations of motion can be solved with the scheme that is listed below for reference.

$$dx1 = dt \cdot \dot{x}_i$$

$$dvx1 = dt \cdot \dot{v}_x(x_i, y_i, z_i, \dot{x}_i, \dot{y}_i, \dot{z}_i, B(x_i, y_i, z_i), t_i)$$

$$dy1 = dt \cdot \dot{y}_i$$

$$dvy1 = dt \cdot \dot{v}_y(x_i, y_i, z_i, \dot{x}_i, \dot{y}_i, \dot{z}_i, B(x_i, y_i, z_i), t_i)$$

$$dz1 = dt \cdot \dot{z}_i$$

$$dvz1 = dt \cdot \dot{v}_z(x_i, y_i, z_i, \dot{x}_i, \dot{y}_i, \dot{z}_i, B(x_i, y_i, z_i), t_i)$$

$$dx2 = dt \cdot (\dot{x}_i + \frac{dx1}{2})$$

$$dvx2 = dt \cdot \dot{v}_x(x_i + \frac{dx1}{2}, y_i + \frac{dy1}{2}, z_i + \frac{dz1}{2}, \dot{x}_i + \frac{dvx1}{2}, \dot{y}_i + \frac{dvy1}{2}, \dot{z}_i + \frac{dvz1}{2}, B(x_i + \frac{dx1}{2}, y_i + \frac{dy1}{2}, z_i + \frac{dz1}{2}), t_i + \frac{dt}{2})$$

$$dy2 = dt \cdot (\dot{y}_i + \frac{dy1}{2})$$

$$dvy2 = dt \cdot \dot{v}_y(x_i + \frac{dx1}{2}, y_i + \frac{dy1}{2}, z_i + \frac{dz1}{2}, \dot{x}_i + \frac{dvx1}{2}, \dot{y}_i + \frac{dvy1}{2}, \dot{z}_i + \frac{dvz1}{2}, B(x_i + \frac{dx1}{2}, y_i + \frac{dy1}{2}, z_i + \frac{dz1}{2}), t_i + \frac{dt}{2})$$

$$dz2 = dt \cdot (\dot{z}_i + \frac{dz1}{2})$$

$$dvz2 = dt \cdot \dot{v}_z(x_i + \frac{dx1}{2}, y_i + \frac{dy1}{2}, z_i + \frac{dz1}{2}, \dot{x}_i + \frac{dvx1}{2}, \dot{y}_i + \frac{dvy1}{2}, \dot{z}_i + \frac{dvz1}{2}, B(x_i + \frac{dx1}{2}, y_i + \frac{dy1}{2}, z_i + \frac{dz1}{2}), t_i + \frac{dt}{2})$$

$$dx_3 = dt \cdot \left(\dot{x}_i + \frac{dx_2}{2} \right)$$

$$dvx_3 = dt \cdot \dot{v}_x \left(x_i + \frac{dx_2}{2}, y_i + \frac{dy_2}{2}, z_i + \frac{dz_2}{2}, \dot{x}_i + \frac{dvx_2}{2}, \dot{y}_i + \frac{dvy_2}{2}, \dot{z}_i + \frac{dvz_2}{2}, B \left(x_i + \frac{dx_2}{2}, y_i + \frac{dy_2}{2}, z_i + \frac{dz_2}{2} \right), t_i + \frac{dt}{2} \right)$$

$$dy_3 = dt \cdot \left(\dot{y}_i + \frac{dy_2}{2} \right)$$

$$dvy_3 = dt \cdot \dot{v}_y \left(x_i + \frac{dx_2}{2}, y_i + \frac{dy_2}{2}, z_i + \frac{dz_2}{2}, \dot{x}_i + \frac{dvx_2}{2}, \dot{y}_i + \frac{dvy_2}{2}, \dot{z}_i + \frac{dvz_2}{2}, B \left(x_i + \frac{dx_2}{2}, y_i + \frac{dy_2}{2}, z_i + \frac{dz_2}{2} \right), t_i + \frac{dt}{2} \right)$$

$$dz_3 = dt \cdot \left(\dot{z}_i + \frac{dz_2}{2} \right)$$

$$dvz_3 = dt \cdot \dot{v}_z \left(x_i + \frac{dx_2}{2}, y_i + \frac{dy_2}{2}, z_i + \frac{dz_2}{2}, \dot{x}_i + \frac{dvx_2}{2}, \dot{y}_i + \frac{dvy_2}{2}, \dot{z}_i + \frac{dvz_2}{2}, B \left(x_i + \frac{dx_2}{2}, y_i + \frac{dy_2}{2}, z_i + \frac{dz_2}{2} \right), t_i + \frac{dt}{2} \right)$$

$$dx_4 = dt \cdot (\dot{x}_i + dx_3)$$

$$dvx_4 = dt \cdot \dot{v}_x \left(x_i + dx_3, y_i + dy_3, z_i + dz_3, \dot{x}_i + dvx_3, \dot{y}_i + dvy_3, \dot{z}_i + dvz_3, B \left(x_i + dx_3, y_i + dy_3, z_i + dz_3 \right), t_i + dt \right)$$

$$dy_4 = dt \cdot (\dot{y}_i + dy_3)$$

$$dvy_4 = dt \cdot \dot{v}_y \left(x_i + dx_3, y_i + dy_3, z_i + dz_3, \dot{x}_i + dvx_3, \dot{y}_i + dvy_3, \dot{z}_i + dvz_3, B \left(x_i + dx_3, y_i + dy_3, z_i + dz_3 \right), t_i + dt \right)$$

$$dz_4 = dt \cdot (\dot{z}_i + dz_3)$$

$$dvz_4 = dt \cdot \dot{v}_z \left(x_i + dx_3, y_i + dy_3, z_i + dz_3, \dot{x}_i + dvx_3, \dot{y}_i + dvy_3, \dot{z}_i + dvz_3, B \left(x_i + dx_3, y_i + dy_3, z_i + dz_3 \right), t_i + dt \right)$$

$$\begin{aligned}
x_{i+1} &= x_i + \frac{dx1 + 2 \cdot dx2 + 2 \cdot dx3 + dx4}{6} \\
\dot{x}_{i+1} &= \dot{x}_i + \frac{dvx1 + 2 \cdot dvx2 + 2 \cdot dvx3 + dvx4}{6} \\
y_{i+1} &= y_i + \frac{dy1 + 2 \cdot dy2 + 2 \cdot dy3 + dy4}{6} \\
\dot{y}_{i+1} &= \dot{y}_i + \frac{dvy1 + 2 \cdot dvy2 + 2 \cdot dvy3 + dvx4}{6} \\
z_{i+1} &= z_i + \frac{dz1 + 2 \cdot dz2 + 2 \cdot dz3 + dz4}{6} \\
\dot{z}_{i+1} &= \dot{z}_i + \frac{dvz1 + 2 \cdot dvz2 + 2 \cdot dvz3 + dvz4}{6}
\end{aligned}$$

2.0.3 Parallelization

Pursuing efficiency, it is necessary to parallelize the model to run it on multiple computing cores at once. The use of the Fortran's implementation of the message passing interface Open MPI was employed to achieve this. The fastest execution of the code is performed by writing as little information as possible. The model only writes each particle's current position, velocity, and time-stamp—each of which get updated every time-step. Therefore, only three vectors that are the length of the amount of particles per process are stored. At specified intervals, the number of particles in each bin of the parallel and perpendicular velocity grid is determined, and the command *MPI_Reduce* is used to combine the partial distributions onto the root process. This total distribution function is then written to a text file. A necessary future enhancement of the model is to instead write the distribution function output in binary format as opposed to ASCII in order to decrease writing time and output file size (the current output files can reach over seven GB for a run of about 2,000,000 particles traced for 25 min). The ERAU Physical Sciences Department's multiple core system Levity was utilized in this study; the department's new cluster will be operational and used by the particle tracer in the near future.

Certain assumptions about the particles' electromagnetic environment restrict

the justification of the model and its results. These assumptions are outlined in the sections to follow.

2.1 Dipole Earth Magnetic Field

The Monte Carlo simulations produced by this model had to be carried out using a simple, mathematical dipole Earth magnetic field. Interpolations that are necessary to perform a simulation using, for instance, a BATSRUS model's magnetic field output file via NASA: CCMC's Kameleon interface are too time consuming with the computing power available (Kameleon will be discussed further in the following section, but it should be mentioned here that the tool has been optimized by CCMC for efficient interpolation performance). Moreover, it is not necessary to use a realistic, quantitative magnetic field model since only a qualitative display of the model's capabilities are sought for the results of this study. The dipolar field is not completely physical, but is sufficient at least for the altitudes of the heating region of interest [Zeng et al., 2006]. This field is one which would naturally occur in the absence of the currents brought upon by the magnetosphere's interaction with the interplanetary magnetic field; it is the magnetic field of the solitary Earth—a field engrained within the planet largely due to the electromagnetic physics of core motion and crustal formation.

For a dipole Earth magnetic field, we can express the Cartesian components as

$$\begin{aligned} B_x &= \frac{3Mxz}{r^5} \\ B_y &= \frac{3Myz}{r^5} \\ B_z &= \frac{M(3z^2 - r^2)}{r^5} \end{aligned} \quad (2.2)$$

[Kivelson and Russel, 1995]

M represents the Earth's magnetic dipole moment. Its value was taken to be 7.94×10^{15} [T·m³] [Kivelson and Russel, 1995]. Note that longitude is irrelevant in

this symmetric magnetic field.

2.1.1 Field Line Display

For purposes of scale and presentation, a display of the dipole field lines was created simply by plotting the transformation equations that transform from Cartesian to spherical coordinates, multiplied by sine-squared of θ (the angle from the positive z axis), and multiplied by a magnitude constant. The specified magnitude constant indicates the distance away from the center of the Earth that a particular dipole field line corresponds to. The mathematical simplicity of this geometrical representation of magnetic dipole field lines is surprising, and an accurate and easily manipulated visual model was thus developed. The plotting loop's step-size and range as well as the number of field lines and their spacing can be changed with three corresponding variables. A three-dimensional visual display of the dipole field model is represented in Figure 2.1.

2.1.2 Dipole Coordinate System

In order to apply the electric field in the parallel and perpendicular directions as well as to analyze perpendicular and parallel velocity and energy components, it is necessary to develop the dipole coordinate system unit vectors in Cartesian—that is, the \hat{q} , \hat{p} , and $\hat{\phi}$ unit vectors which represent the field-aligned and two transverse directions, respectively (see Figure 2.2).

The ϕ direction of the dipole coordinate system is the same unit vector as the spherical coordinate system's azimuthal unit vector. Expressed in Cartesian components,

$$\hat{\phi} = -\sin(\phi)\hat{x} + \cos(\phi)\hat{y}$$

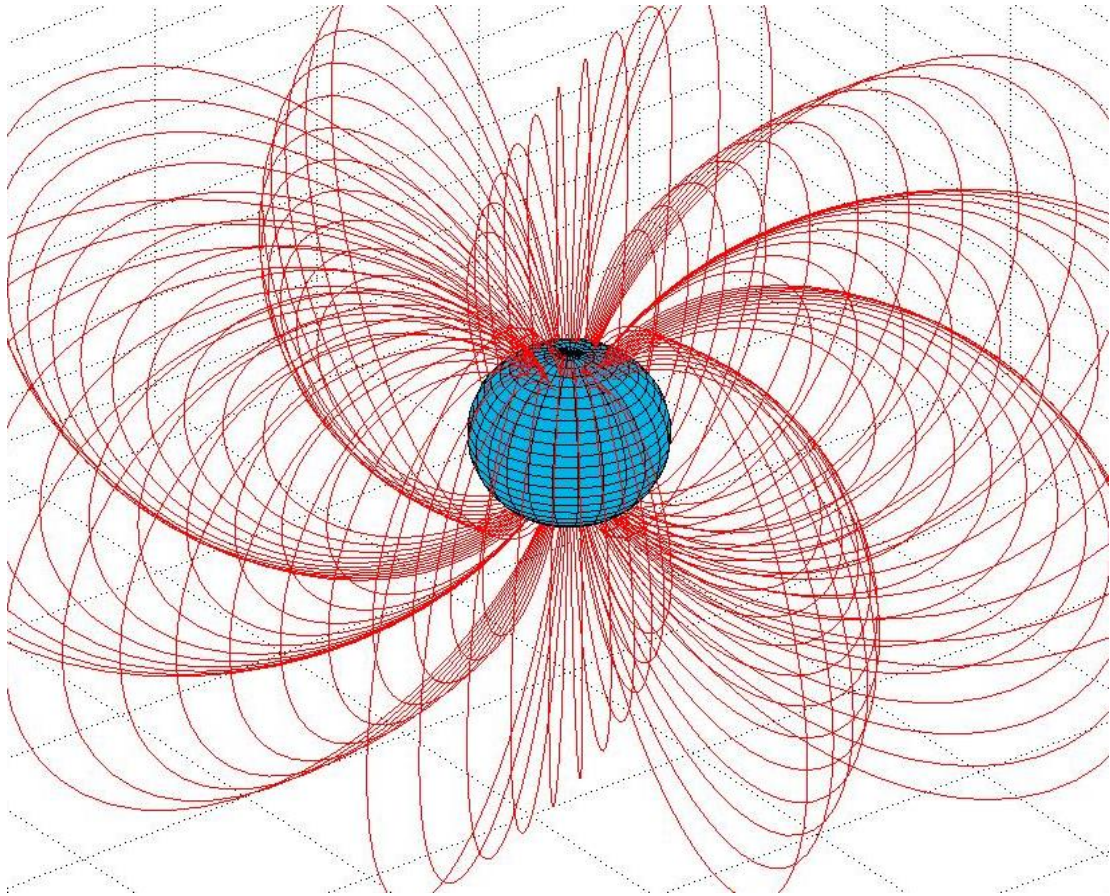


Figure 2.1: Display of the Earth and its dipole magnetic field lines. This figure displays the visual model's flexibility.

From geometry,

$$\hat{\phi} = \frac{-y}{\sqrt{x^2 + y^2}}\hat{x} + \frac{x}{\sqrt{x^2 + y^2}}\hat{y} \quad (2.3)$$

In the direction parallel to the magnetic field, since we already have the three components of the magnetic field, we can divide the magnetic field vector by its

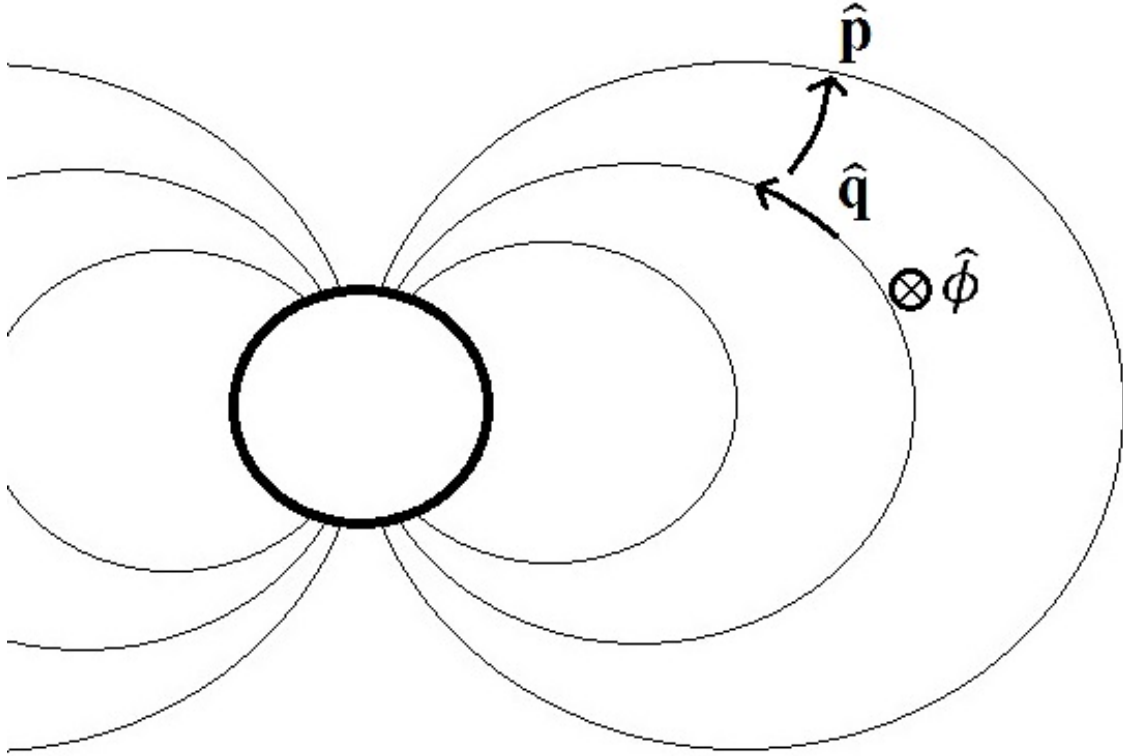


Figure 2.2: Dipole coordinate system unit vectors

magnitude (B) to obtain the appropriate unit vector.

$$\hat{q} = \frac{\vec{B}}{B} = \frac{B_x}{B}\hat{x} + \frac{B_y}{B}\hat{y} + \frac{B_z}{B}\hat{z} \quad (2.4)$$

The third direction, which is perpendicular to the previously stated directions, is defined as:

$$\hat{p} = \hat{\phi} \times \hat{q} = \frac{1}{B\sqrt{x^2 + y^2}} [xB_z\hat{x} + yB_z\hat{y} - (yB_y + xB_x)\hat{z}] \quad (2.5)$$

2.2 CCMC: BATSRUS Magnetic Field

As it turns out, because the \hat{q} direction is derived from the applied magnetic field, and since the \hat{p} unit vector is derived from \hat{q} and the geometrical $\hat{\phi}$, these unit vectors are also valid for irregular dipole fields such as the Earth's actual field—as long as the field is azimuthally symmetric. In other words, because the $\hat{\phi}$ direction is always perpendicular to an azimuthally symmetric Earth magnetic field, the dipole unit vectors described above are valid even for imperfect dipole magnetic fields with the assumption of a negligible azimuthal asymmetry. Therefore, this assumption allows for the heating to be applied in the transverse directions with the BATSRUS magnetic field using the same unit vector equations that are described in Section 2.1.2.

To increase the model's versatility, to prepare it for more quantitative studies, and to add the functionality of mapping outflow trajectories to a realistic magnetosphere, the tracer was adapted so that it is able to immerse its particles within any NASA: Community Coordinated Modeling Center (CCMC) modeled magnetic field that is compatible with Kameleon (CTIP, BATSRUS, OpenGGCM, MAS, ENLIL, LFM). Kameleon is a body of interfacing software which converts magnetospheric and heliospheric model output into one common data format (.cdf files) for researchers to more easily use. The tool allows convenient access to modeled data, and it also calculates additional metadata during the format conversion process. Included in the package are pre-made, generalized wrappers for researchers to interface their Fortran or IDL models with Kameleon's interpolator package, which is written in C (the latest distribution which is not employed in this study is written in C++). Although all wrappers are not included with the package, the Kameleon tool is usable with any other C-compatible programming language (such as Matlab, Python, Java, etc.). The availability of the pre-made wrappers was a factor in the decision to translate the original Monte Carlo model from Matlab to Fortran during the thesis endeavor (although the main motivation for this translation was the fast operating environment provided by Fortran). (Obtained from <http://ccmc.gsfc.nasa.gov/downloads/kameleon.php>)

The BATSRUS, or Block-Adaptive-Tree-Roe-Upwind-Scheme, Global Magnetosphere (GM) model is a NASA: CCMC model that was initially developed by the Center for Space Environment Modeling (CSEM). The magnetospheric model's boundaries are at altitude ranges from $33 R_E$ sunward to $250 R_E$ tailward. Inputs to the model include the solar wind plasma velocity components, density, temperature, and magnetic field components; the magnetospheric boundary conditions are obtained from CCMC's Inner Heliosphere (IH) model in order to solve the three-dimensional MHD equations for magnetospheric plasma parameters such as number density, pressure, velocity, magnetic field, currents, and ionospheric parameters such as electric potential and Hall and Peterson conductances. The inner boundary of the GM model uses CCMC's Inner Magnetosphere (IM) and Ionospheric Electrodynamics (IE) models. The model uses varying grid space intervals at different regions of the magnetosphere. The BATSRUS model is in the Geocentric Solar Magnetic (GSM) coordinate system, which has its positive x -axis fixated towards the sun, while the positive z -axis adheres to the direction of the northwardly extending magnetic dipole axis. (Obtained from <http://ccmc.gsfc.nasa.gov/models/modelinfo.php?model=BATS-R-US>)

NASA: CCMC's Java visualization program called Space Weather Explorer 2 (SWX2) works in conjunction with Kameleon's .cdf files to display an interactive, two-dimensional map of a specified time slice of a given model. The program is still undergoing development, but nonetheless has the ability to create a descriptive figure which can plot most model output quantities. Figure 2.3 uses SWX2 to show the plasma velocity and the magnetic field for the BATSRUS output file used in the results of Chapter 4 (Results: Mapping to the Magnetosphere). An obvious density wave was released (this is viewable using NASA: CCMC's tool, iSWA).

This adaptation of this thesis's model, which uses the Kameleon interpolation interface to map particles throughout a realistic BATSRUS magnetosphere, extracts both the local magnetic field value and the local plasma motion from the NASA model. In order to replicate the actual Lorentz force experienced by a particle in this realistic BATSRUS environment, the motional plasma electric field which results from the relative velocity difference of the motion of the particle and the

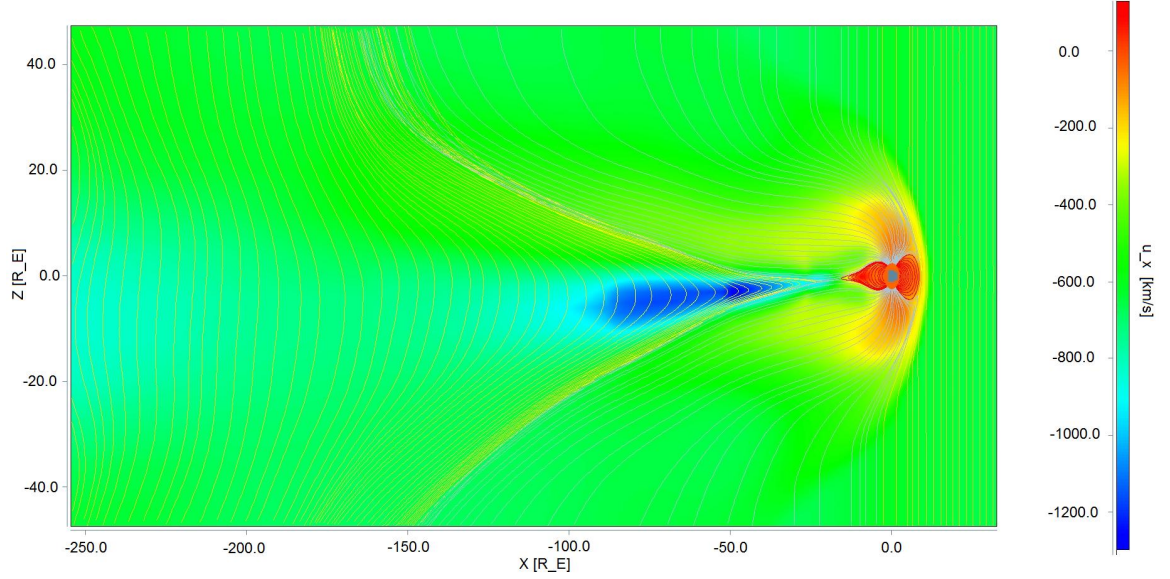


Figure 2.3: SWX2 visualization of BATSURUS Global Magnetosphere plasma velocity and magnetic field during the geomagnetic storm on April 5, 2010. The streamlines represent the orientation of the Earth’s magnetic field, and the color contours represent the x -component of velocity. Grey lines are open geomagnetic field lines, red lines are closed, and yellow lines are the interplanetary magnetic field. The configuration of the magnetic field and the plasma velocity suggests a recent plasmoid ejection from the magnetotail. The K_p index reached 5 during this time, and the geomagnetic storm eventually reached a $K_p = 8$.

(Obtained from <http://ccmc.gsfc.nasa.gov/swx2>)

motion of the background plasma is accounted for by adding the term $\vec{E}_{plasma} = -\vec{u} \times \vec{B}$. Here, $\vec{u} = u_x \hat{x} + u_y \hat{y} + u_z \hat{z}$ denotes the Cartesian components of the background plasma in GSM coordinates.

In this case, our basic equations of motion take the form:

$$\begin{aligned}
 a_x &= \frac{e}{m_o} (E_x + v_y B_z - v_z B_y - u_y B_z + u_z B_y) - \frac{GM_E x}{(x^2 + y^2 + z^2)^{\frac{3}{2}}} \\
 a_y &= \frac{e}{m_o} (E_y + v_z B_x - v_x B_z - u_z B_x + u_x B_z) - \frac{GM_E y}{(x^2 + y^2 + z^2)^{\frac{3}{2}}} \\
 a_z &= \frac{e}{m_o} (E_z + v_x B_y - v_y B_x - u_x B_y + u_y B_x) - \frac{GM_E z}{(x^2 + y^2 + z^2)^{\frac{3}{2}}}
 \end{aligned} \tag{2.6}$$

Here, B_x , B_y , B_z , u_x , u_y , and u_z , are the interpolated values extracted from the BATSUS .cdf file. It is relatively computationally costly to interpolate on the .cdf output file at every time-step for these six values. At a twentieth of a gyro-period, the time-step can be as small as 0.85 ms in the region of interest, and trajectory tracing times are up to 25 min in this study.

2.3 Electric Field Environment

This section serves to explain how the transverse and parallel electric fields were applied to the test particles. Note here that, in the main study, all electric fields were turned off after 18 min of tracing.

2.3.1 Transverse Electric Wave Field

The physical region of interest is of auroral latitudes at altitudes containing observed BBELF wave turbulence that is resonant with the gyro-motion of the O^+ ion, which varies, but is often resonant in the approximate range of 1000 km to 15,000 km altitude. This wave-particle interaction phenomenon energizes the ions at varying rates, because the energizing transverse electric field magnitude varies with frequency, and the gyrofrequency varies with altitude. Particularly, the BBELF field intensity is larger at larger frequencies, and the gyrofrequency increases with altitude, and therefore the resonant BBELF field intensity is greater for ions at greater altitudes. As suggested in Chapter 1, many studies have presented observations suggesting that most O^+ transverse heating events observed below 4000 km in this auroral region are associated with simultaneous enhancements of BBELF turbulence [Norqvist et al., 1998, Lund et al., 2000]. The oscillating electric field waves are assumed to have associated magnetic fields which may be considered negligible in comparison to the Earth's magnetic field [Chang et al., 1986]. In addition, it is not possible to properly account for the associated magnetic field without knowledge of the BBELF wave mode and phase velocity [Hultqvist et al., 1999]. Since we make the assumption that only the portion of the electric field

wave which is resonant with the particle affects the particle's motion [Chang et al., 1986], a simple LHCP transverse electric field wave that oscillates at the ion's gyrofrequency was constructed in order to induce the ion heating and energization effects. Thus, into the equations of motion is added a time-dependent transverse electric field with $\hat{\phi}$ and \hat{p} components:

$$\vec{E}_{\perp} = -E_{\phi} \sin(\Omega_c t + \epsilon) \hat{\phi} + E_p \cos(\Omega_c t + \epsilon) \hat{p} \quad (2.7)$$

Ω_c signifies the familiar cyclotron frequency given by $\frac{eB}{m_0}$ rad s⁻¹, and t is the time of tracing in seconds. The phase of the electric field wave, ϵ , is the source of stochastic heating; it is a random value in the range from $\pm\pi$. This stochastic nature of the electric field wave phase value relative to the phase of the ion motion is referred to as incoherency (the other stochastic aspect of the simulation is the randomized initial velocity and position, to be explained more fully in Chapter 3; stochastic collisions are optionally turned on at lower altitudes, but their effects have not yet been accurately accounted for). E_{ϕ} and E_p signify the transversely oriented components of the simulated BBELF wave. The Cartesian unit vectors in the direction of these transverse electric field components will be developed in the following section.

The range of the randomized wave phase ϵ varied over the course of the study. This is because, during the developmental stage of the study, the expected qualitative results were seen to develop after a maximum of 10 minutes of tracing only when partial or full coherency ($\epsilon = \pm\pi/2$ or 0, respectively). It should be stressed that a much more in depth analysis of the BBELF autocorrelation time would be necessary in order to determine the correct amount of coherency between the energizing wave phase and the ion cyclotron motion phase; the application over the range of physical possibility was an ad hoc parameter that also served to assist in the model development process. For the fully incoherent case, the transverse energy peaks within the first few seconds of energization, but is quickly dampened, and the magnitude of energization takes at least 15 minutes to reach the

same magnitude as the partially or fully coherent simulation with otherwise equivalent parameters (but it does eventually produce a similar magnitude of energization). The transverse energy of the partially coherent or fully coherent case initially peaks, but there is not a large subsequent damping of energy. Therefore coherency allows for the procurement of qualitatively correct distribution functions using short model runtimes.

Although coherency of energization—that is, the energizing wave’s range of randomized phase ϵ is not equal to $\pm\pi$ —may not be a realistic process, some degree of incoherency is to be expected. How much incoherency to be expected is unclear, though, so this study simply explores the response of distribution functions for a wide range of cases (coherent, partially coherent, and incoherent). Each particle experiences a different, randomized value of ϵ at each time-step.

To obtain these transverse electric field components of Equation 2.7 in Cartesian coordinates, we multiply the dipole components by their unit vectors $\hat{\phi}$ and $\hat{\rho}$ expressed in Cartesian (given by Equations 2.3 and 2.5). Equation 2.7 therefore becomes

$$\vec{E}_{\perp} = \frac{-E_{\phi} \sin(\Omega_c t + \epsilon)}{\sqrt{x^2 + y^2}} (-y\hat{x} + x\hat{y}) + \frac{E_p \cos(\Omega_c t + \epsilon)}{B\sqrt{x^2 + y^2}} [xB_z\hat{x} + yB_z\hat{y} - (yB_y + xB_x)\hat{z}]$$

Or, alternatively, the Cartesian components of the transverse electric field wave for insertion into the equations of motion take the form:

$$\begin{aligned} E_x &= E_{\phi} \sin(\Omega_c t + \epsilon) \frac{y}{\sqrt{x^2 + y^2}} + E_p \cos(\Omega_c t + \epsilon) \frac{xB_z}{B\sqrt{x^2 + y^2}} \\ E_y &= -E_{\phi} \sin(\Omega_c t + \epsilon) \frac{x}{\sqrt{x^2 + y^2}} + E_p \cos(\Omega_c t + \epsilon) \frac{yB_z}{B\sqrt{x^2 + y^2}} \\ E_z &= -E_p \cos(\Omega_c t + \epsilon) \frac{yB_y + xB_x}{B\sqrt{x^2 + y^2}} \end{aligned} \quad (2.8)$$

This method of energization is a novel approach in that it computes the effects of the wave-particle interaction directly from the fundamental equations of motion. Instead of incorporating a heating rate term, which reproduces an observed

consequence of the wave-particle interaction process, the exact resonance process that produces the energization is reproduced. The usual approach in, for instance, guiding center tracing models, is to apply this energization rate which has been observed and determined to be correlated to the transverse energization process. The final section of this chapter will demonstrate the details of this comparison of energization methods.

The magnitude of the transverse BBELF electric field turbulence in the polar cap boundary and cusp region is known to change with frequency according to a power law spectrum [Kintner, 1976, Gurnett et al., 1984]. A widely utilized empirical relationship for the BBELF electric wave field spectral density is given by

$$|\vec{E}_{\perp}(\omega)|^2 = E_0^2 \left(\frac{\omega_0}{\omega} \right)^{\alpha}. \quad (2.9)$$

[Crew et al., 1990, Retterer et al., 1994, Brown et al., 1995, Wu et al., 1999, 2002, Zeng et al., 2006]

Here, $|\vec{E}_{\perp}(\omega)|^2$ has units of $\text{V}^2 \text{m}^{-2} \text{Hz}^{-1}$ and is the power spectral density of the transverse BBELF wave field at frequency ω in Hz. E_0^2 is the reference value for the wave spectral density at a reference frequency ω_0 . The reference values that are assumed to be correct for a typical BBELF wave field in this study are the values used by Zeng et al. [2006]: $E_0^2 = 0.3 \times 10^{-6} \text{V}^2 \text{m}^{-2} \text{Hz}^{-1}$ at $\omega_0 = 6.5 \text{Hz}$. This frequency value is the O^+ gyrofrequency at 1 R_E in the model used by Zeng et al. [2006]. The gyrofrequency at 1 R_E in the simple dipole model of this study is 7.2 Hz, which suggests that the magnetic field value at 1 R_E is 111.0% of Zeng's magnetic field, providing an explanation (or a contributor) for the less energetic outflows that are produced by the model of this study when using this spectral density reference value. As a consequence, the spectral density reference value was used as a changing parameter in this study in order to produce appreciably energized, qualitative distribution functions (as will be seen in Chapter 5). Most of the model runs therefore used spectral density reference values that are two

to three magnitudes larger than Zeng et al.'s value. Some spectral densities from other studies are listed in Table 2.1. The parameter α is the power law index and is taken to be 1.7, which is the value used by Zeng et al. [2006], Crew et al. [1990], and Wu et al. [1999, 2002]. The power law index α can be a variable parameter for investigation in a future application of this model.

Table 2.1: Power Spectral Density Reference Values

Study	E_0^2 [$V^2 \text{ m}^{-2} \text{ Hz}^{-1}$]	ω_0 [Hz]	Altitude
Zeng et al. '06	3×10^{-7}	6.5	1 R_E
Bouhram et al. '02	1.7×10^{-7}	25	2000 km
Wu et al. '99, '00	10^{-8}	6.5	1 R_E
Brown et al. '95	10^{-8}	6.5	1 R_E
Crew et al. '90	1.2×10^{-6}	5.6	1.2 R_E
Chang et al. '86	2.2×10^{-8}	45	1 R_E

A simplification made in the model is the extraction of the electric field intensity magnitude, E_{\perp} , from this power spectral density power law relationship of Equation 2.9. This same simplification is commonly made, for example, in particle tracing methods which use a heating rate that is derived from the electric wave field spectral density at the gyrofrequency Chang et al. [1986], Chang [1991], Retterer et al. [1994], Zeng et al. [2006]. To use an electric field magnitude which changes with frequency according to the above spectral density power law relationship, it was necessary to impose the assumption that BBELF waves above and below the O^+ gyrofrequency cause insignificant effects upon the wave-particle interaction process in comparison to the waves which are oscillating exactly at the resonant gyrofrequency. Accordingly, when integrating the power law spectrum over all frequencies in order to remove its frequency dependence, the Dirac delta function was employed to extract the electric field intensity at only the local O^+ gyrofrequency. The use of the delta function for the extraction of the intensity at only the resonant frequency is also justified in Chang [1991] and Retterer et al. [1994]. For example, in Retterer et al. [1994], the group also uses the delta function

to remove the energizing effects of any electric field waves which have a transverse phase speed that is not equal to the ion speed (waves with frequencies other than the gyrofrequency), which is an equivalent procedure as employed in this study. The method employed is outlined in the following description.

To remove the frequency dependence from the electric field spectral density and obtain the spectrum's total electric field intensity, one integrates the spectral density over the spectrum's range of frequencies. To obtain the intensity at the only the gyrofrequency, the following useful property of the Dirac delta function was used.

$$\int_{-\infty}^{\infty} f(\tau)\delta(\tau - \chi)d\tau = f(\chi)$$

Here, τ and χ are analogous to ω and Ω_c , respectively. Applied to the power law spectrum, the above property produces

$$|\vec{E}_{\perp}(\Omega_c)|^2 = \int_0^{\infty} |\vec{E}_{\perp}(\omega)|^2 \delta(\omega - \Omega_c) d\omega = \int_0^{\infty} E_0^2 \left(\frac{\omega_0}{\omega}\right)^{\alpha} \delta(\omega - \Omega_c) d\omega = E_0^2 \left(\frac{2\pi\omega_0}{\Omega_c}\right)^{\alpha}$$

Note again here that Ω_c is in rad s^{-1} .

Therefore, our assumption that only the resonant portion of the transverse BBELF spectrum is significant for the energization process produces the following relationship for the electric field intensity (V m^{-1}) experienced by the ion.

$$E_{\perp} \approx E_0 \left(\frac{2\pi\omega_0}{\Omega_c}\right)^{\alpha/2} \quad (2.10)$$

Note here that another, different justification of this estimated removal of frequency dependence is provided in the 1986 paper by Chang et al., where they use the estimation that the change in frequency during one time-step multiplied by the time-step is approximately equal to one. This approximation is made to remove frequency dependence during the derivation of the guiding center approximation's heating rate due to transverse energization.

However, in reality the spectral density is not only a function of frequency—it is also a function of the wave vector. Therefore this extracted electric field intensity produces a transverse energization rate which does not hold at high velocities, and thus the high-energy tail of the ion conic is not accurately represented [Retterer et al., 1994]. This is true for this model’s method of tracing the exact equations of motion as well as in the case of the guiding center approximation, because the guiding center method also uses this approximation.

It follows from the magnitude of the perpendicular LHCP electric field vector that is listed in Equation 2.7,

$$|\vec{E}_\perp| = \sqrt{E_\phi^2 \sin^2(\Omega_c t + \epsilon) + E_p^2 \cos^2(\Omega_c t + \epsilon)}$$

Due to the imposed circular polarization condition, the transverse electric field is distributed evenly in both the $\hat{\phi}$ and \hat{p} directions; then, the sine and cosine portions of the magnitude are removed due to the Pythagorean trigonometric identity, and we have:

$$E_\phi = E_p = E_0 \left(\frac{2\pi\omega_0}{\Omega_c} \right)^{\alpha/2} \quad (2.11)$$

Because observations such as those of Cluster have suggested that the BBELF waves which produce the transverse energization undergo a saturation at wavelengths larger than a few tens of km, a finite radius transverse heating criterion is introduced [Bouhram et al., 2004]. The transverse energization in the model of this study therefore gets turned off if the ion’s Larmor radius exceeds 10 km. The environmental parameters of the current study—even with the transverse energization—would lead one to believe that a Larmor radius of this size is prohibited; however, the maximum Larmor radius in model’s current environment can reach well over 10 km throughout the heating process. This happens when the energization rate is gradual enough to keep ions in the heating region for a long residence time, yet large enough to add energy with an incoherent wave field. This situation where

the energizing field magnitude is optimally sized concerning the balance of residence time and energization rate seems to be the situation which causes the most total energization. This creates the condition that too strong of a perpendicular field will actually have the net effect of making the outflows less energetic. More investigations into the quantitative details of this effect can be investigated with the model in the future.

Another rough method of calculating the electric field intensity as it changes with frequency and altitude was formulated during this thesis endeavor via the realization from observations that the logarithm of the frequency and the logarithm of the power spectral density of the BBELF energizing wave field are linearly related [Gurnett et al., 1984, Chang et al., 1986, Bouhram et al., 2002] (this is because of the power law the spectral density follows). An adjustable estimate of the BBELF wave field intensity's trend with frequency was produced by analyzing and reproducing the general linear trend. Therefore, the electric field intensity's variations with altitude and gyrofrequency could be constructed from fitting a line to observed spectral density and by using a similar assumption as was made above which allowed us to remove frequency dependence and extract the function value at the gyrofrequency by integrating the spectral density multiplied by with the Dirac delta function. This formulated BBELF electric field function is similar to the electric field intensity (Equation 2.11) which was extracted from the spectral density power law spectrum of Equation 2.9, in that that this function also has specifiable reference values and a power law. Surprisingly, the electric field intensity experienced by a transversely heated ion using the following relationship exhibits a similar trend of magnitude change as does the electric field from the commonly used power law spectrum above.

$$E_{\perp} = 10^{b_0/2} \left(\frac{\Omega_c}{2\pi} \right)^{m_0/2} \quad (2.12)$$

Here, b_0 and m_0 signify respectively the intercept and the slope values for the line equation from a plot which relates a BBELF wave field's logarithm of the

electric field power spectral density versus the logarithm of the wave frequency. Some reference values of m_0 and b_0 which were obtained from Bouhram et al. [2002]’s depiction of a BBELF field enhancement associated with a heating event are $m_0 = -1.640$ and $b_0 = -4.506$. Equation 2.12 provides a convenient way to the extract an estimate of electric field magnitude at the gyrofrequency from an observed power spectral density spectrum which follows a power law in frequency.

2.3.2 Field-Aligned Potential Drops

The inclusion of a parallel, field-aligned electric potential (the electric field component $E_q \hat{q}$) would be physically justifiable only if the ions of the simulation could be treated self-consistently [Bouhram et al., 2003]. This feature of self-consistency was not imposed in the current model of this study, but plans have been initialized to implement it in the future. The effects of typically modeled parallel electric fields were included only to demonstrate the model’s potential to produce qualitative velocity distribution functions which take into account multiple modes of acceleration.

Two instances of parallel potential drops are explored briefly (they were examined both separately and combined, but only examples of their separate effects are documented here). As was discussed in Singh and Chan [1993], one kind of parallel electric field is a field-aligned potential pulse that occurs either in the parallel or antiparallel direction. These pulses result from the transversely heated flux tube’s development of upper and lower shocks. The pulses are simulated in this study with impulses of 10 mV m^{-1} for 10 ms at a time (by example of Singh and Chan [1993]). This roughly corresponds to a potential drop of 0.1 V (depending upon the magnitude of parallel velocity). The pulses are applied during the initial peak in transverse energy (this peak is a signature of this transverse energization process). Other pulse magnitudes were briefly studied, but these simulations are not presented in this work.

A more commonly modeled parallel electric field takes the form of a gradual,

downward parallel potential drop. These potentials have been observed in the turbulent cusp/cleft, PCB and auroral regions of variable magnitude. In this study, it was estimated that the typical ion experiences a peak energy of ~ 20 eV in the transverse direction (which gets converted to upward parallel energy), and therefore a potential of 20 V was applied to the O^+ ions via a 0.0067 mV m^{-1} that was applied in the positive \hat{q} direction (downward) from 3000 to 6000 km altitude. The idea was to apply a voltage drop which caused a similar downward energization as that of the transverse energization so as to produce counterstreaming distribution functions. This field-aligned potential drop simulation can be viewed in Figures 5.9 and 5.10. Note here that the estimate of 20 eV for the typical transverse energy peak was slightly too low compared with most of the study's simulations (it should have been around three times this size in order to match the average particle's transverse energy peak).

The x , y , and z components of the parallel electric field are simply expressed by substituting the Cartesian components of the \hat{q} vector:

$$\vec{E}_q = E_q \hat{q} = \frac{E_q}{B} (B_x \hat{x} + B_y \hat{y} + B_z \hat{z}) \quad (2.13)$$

2.4 Final Equations of Motion and a Comparison to Guiding Center Equations of Motion

2.4.1 Final Equations of Motion

For substitution into our general equations of motion, the Cartesian components of the transverse, field-aligned, and motional plasma electric fields are:

$$\begin{aligned} E_x &= E_\phi \sin(\Omega_c t + \epsilon) \frac{y}{\sqrt{x^2 + y^2}} + E_p \cos(\Omega_c t + \epsilon) \frac{x B_z}{B \sqrt{x^2 + y^2}} + \frac{E_q B_x}{B} - u_y B_z + u_z B_y \\ E_y &= -E_\phi \sin(\Omega_c t + \epsilon) \frac{x}{\sqrt{x^2 + y^2}} + E_p \cos(\Omega_c t + \epsilon) \frac{y B_z}{B \sqrt{x^2 + y^2}} - u_z B_x + u_x B_z \\ E_z &= -E_p \cos(\Omega_c t + \epsilon) \frac{y B_y + x B_x}{B \sqrt{x^2 + y^2}} - u_x B_y + u_y B_z \end{aligned} \quad (2.14)$$

Substituting these electric field components into Equations 2.1, we have:

$$\begin{aligned}
a_x &= \frac{e}{m_0} \left[E_\phi \sin(\Omega_c t + \epsilon) \frac{y}{\sqrt{x^2 + y^2}} + E_p \cos(\Omega_c t + \epsilon) \frac{x B_z}{B \sqrt{x^2 + y^2}} + \frac{E_q B_x}{B} + v_y B_z \right. \\
&\quad \left. - v_z B_y - u_y B_z + u_z B_y \right] - \frac{GM_{Ex}}{(x^2 + y^2 + z^2)^{\frac{3}{2}}} \\
a_y &= \frac{e}{m_0} \left[-E_\phi \sin(\Omega_c t + \epsilon) \frac{x}{\sqrt{x^2 + y^2}} + E_p \cos(\Omega_c t + \epsilon) \frac{y B_z}{B \sqrt{x^2 + y^2}} + \frac{E_q B_y}{B} + v_z B_x - v_x B_z \right. \\
&\quad \left. - u_z B_x + u_x B_z \right] - \frac{GM_{Ey}}{(x^2 + y^2 + z^2)^{\frac{3}{2}}} \\
a_z &= \frac{e}{m_0} \left[-E_p \cos(\Omega_c t + \epsilon) \frac{y B_y + x B_x}{B \sqrt{x^2 + y^2}} + \frac{E_q B_z}{B} + v_x B_y - v_y B_x - u_x B_y + u_y B_z \right] - \frac{GM_{Ez}}{(x^2 + y^2 + z^2)^{\frac{3}{2}}}
\end{aligned} \tag{2.15}$$

where the magnetic field components B_x, B_y, B_z and total magnitude B are obtained either from the dipole field (Equations 2.2) or from interpolations upon the BATSRUS magnetosphere output. In the dipole model, $u_x = u_y = u_z = 0$. The transverse electric field magnitudes E_ϕ and E_p vary according to the power law given in Equation 2.11. Equations 2.15 are the final equations of motion used in this study.

2.4.2 Comparison to the Guiding Center Approximation

For comparative purposes, the equations of motion for the guiding center particle trace method were sought. It was found that, in order to achieve with the guiding center approximation the same accurate three-dimensional, transversely heated particle trace that is described in the outline of this chapter, some extensively sophisticated equations of motion must be invoked, and these require many more magnetic field interpolations per time-step. Although the equations of motion for the guiding center were derived, the method was not applied in this study. They are not discussed here; however, a typical guiding center trace approximation used to simulate this transverse heating process in one-dimension is presented below. A future goal is to compare and to balance the accuracy and the efficiency of the two methods of three-dimensional tracing.

The guiding center approximation for charged particle motion traces a so-called mean-particle which is located at the center point of the gyro-motion as it moves throughout the background magnetic field. The method is convenient for modeling this transverse acceleration process because its coordinate system is set in the geomagnetic field's parallel \hat{q} direction (as well as the perpendicular $\hat{\phi}$ and \hat{p} directions for three-dimensional tracing equations described previously). This is useful because ion outflows are in general frozen to the magnetic field lines, allowing for a one-dimensional approximation in the field-aligned direction to suffice when analyzing the outflows.

The classic guiding center approximation traditionally uses the field-aligned acceleration equation in conjunction with the transverse drift velocity terms in order to describe adiabatic motion. This traditional method extracts and retains only first order terms from the exact equations of motion, although higher degrees of approximation are possible [Northrop, 1961, 1963, 1966]. The approximation also only applies for particle immersed in electromagnetic fields which vary slowly in space and time.

Since type-II outflows are non-adiabatic, a certain adaptation to the classic guiding center equations of motion needs to be made in order to properly incorporate the effects of the transverse energization. This following relation is an example typical of the application of the guiding center approximation to the transverse heating process, and it is the particular equation of motion from Bouhram et al. [2003].

$$m_i \dot{v}_{\parallel} = q_i E_{\parallel} - m_i g(s) - W_{\perp} \left[\frac{d \ln(B)}{ds} \right] \quad (2.16)$$

Here, s is the distance along the magnetic field line, $g(s)$ is the field-aligned component of gravity, and W_{\perp} is the transverse energy. As was derived by Chang and Coppi [1981], the transverse heating rate translates to parallel motion via the last term of the equation. The term is the effective field-aligned mirror force which results from an increase in perpendicular velocity.

The perpendicular energy, W_{\perp} , from Equation 2.16 above is found by integrating the relationship below:

$$\dot{W}_{\perp} = W_{\perp} v_{\parallel} \left[\frac{d \ln(B)}{ds} \right] + \dot{W}_{\perp, res} \quad (2.17)$$

[Chang et al., 1986]

The main point of this comparison is to demonstrate some relative disadvantages of the guiding center approximation in relation to solving the exact equations of motion of Equations 2.15. The obvious advantage of the guiding center approximation is its relative efficiency as compared to integrating the exact equations of motion. The most obvious disadvantage of the guiding center approximation occurs when the Larmor radius is large enough to have a significant difference of magnetic field values one Larmor radius apart in the transverse direction. At 10 R_E altitude, the oxygen ion's Larmor radius can be distances of 20 km. A quantitative investigation into the error resulting from this incorrect magnetic field value which occurs when the gyro-motion is not resolved should be performed in the future. Also, the outflows have significant field-aligned components of velocity, and upon consideration that the oxygen ion's gyro-period can be as much as 25 s at 10 R_E altitude, hundreds of kilometers in the parallel direction can be traversed over one gyro-period, conceivably resulting in appreciable compounding of error if the magnetic environment is dynamic. The guiding center approximation is therefore much less accurate compared to resolving gyro-motion (Equations 2.15) when mapping trajectories to significant altitudes in the magnetosphere.

Efficiency is the motivation behind the formulation of the guiding center approximation. It is the method's goal to trace particles with as little computation as possible, i.e., with as large of time-step as possible which maintains accuracy. The advantage of guiding center tracing from a statistical standpoint is illustrated by, for example, Wu et al. [1999]'s smallest time-step used in their simulation of 0.5 s. This is over 500 times larger than the size of the smallest time-step of this study (≈ 0.85 ms). A rough estimate, then, suggests that Wu et al. [1999] could trace over 500 times more particles in the same amount of runtime. However, although the

larger time-step has the potential to cause a statistical advantage if runtimes are equal, this large of a time-step means that the outflowing ions can travel on the order of a few kilometers in the upwardly parallel direction between time-steps. This large altitudinal change between time-steps is a source of the guiding center approximation's relative disadvantage in accuracy as compared to the method employed in this study, and it is described immediately below.

The simplification made in Section 2.3.1 in Equation 2.10 where the spectral density is evaluated at a singular frequency is the manifestation of the aforementioned source of inaccuracy caused by the large time-step. The guiding center method also uses the idea that the spectral density can be evaluated at the gyrofrequency in this way. Their large changes of altitude between large time-steps will cause appreciable changes in gyrofrequency, and therefore the change in electric field intensity is not accounted for throughout the kilometer(s) traversed during a single time-step. Although this subtle source of inaccuracy may be insignificant and still allows for the calculation of at least semi-quantitative results using the guiding center trace, trajectories of the method have at least a finite relative surplus of error in comparison to Equations 2.15. If a quantitative result which takes into account large changes in BBELF intensity on altitude scales less than a few kilometers is sought, Equations 2.15 are more advantageous in this sense. An error analysis for this situation should be performed in the future. Note here that Equations 2.15 also have the potential to create a relatively more closely quantitative result than the guiding center trace because the trajectories are traced in all three dimensions, whereas it becomes relatively involved to accurately account for all three dimensions using the guiding center method.

Also, because the guiding center approximation uses the same assumption that the spectral density can be evaluated at a single gyrofrequency, both methods are subject to the limitations of the assumption. As mentioned in Section 2.3.1, the spectral density is a function of both the frequency and the wave vector. This leads to a break down of the aforementioned assumption at high velocities, and the use of an incorrect spectral density to calculate the energization rate. Thus the high-energy tail of the ion conic is not accurately represented [Retterer et al., 1994].

There have been studies such as Crew and Chang [1985], Retterer et al. [1994], and Barghouthi et al. [1998] which have developed a complicated method of calculating a velocity-dependent energization rate, but these methods depend on the measurement of the perpendicular wavelength of BBELF fields, which is a difficult attainment [Zeng et al., 2006]. Therefore, studies such as Bouhram et al. [2003] and Zeng et al. [2006] have resorted to the simpler relationship for the energization rate that is based upon the spectral density which is solely frequency dependent, described previously (Equation 2.9).

Lastly, it will be shown that the exact equations of motion used in this study have another advantage (or an additional versatility) as compared to the guiding center approximation via a brief summary of the derivation of the heating rate caused by the resonant wave-particle interaction process.

Identical to the transverse heating mechanism employed in this study is the velocity impulse which begins the derivation of the guiding center transverse heating rate:

$$\Delta\vec{v}_\perp = \left(\frac{q_i \vec{E}_\perp}{m_i} \right) \Delta t \quad (2.18)$$

It follows that the increase in transverse energy experienced by the particle from the impulse in transverse velocity is equal to

$$\Delta W_{\perp, res} = \frac{1}{2} m_i (\vec{v}_\perp + \Delta\vec{v}_\perp)^2 - \frac{1}{2} m_i v_\perp^2 = m_i \vec{v}_\perp \cdot \Delta\vec{v}_\perp + \frac{1}{2} m_i \Delta v_\perp^2$$

[Chang et al., 1986, Bouhram et al., 2003]

Then, in pursuit of the heating rate \dot{W}_{res} for use in the Equation 2.17, the guiding center approximation makes use of a necessary initial condition in which the ions are distributed gyrotropically. In this case, the ions are distributed uniformly about a symmetric magnetic field so that, on average, there is always an ion-ion pair having equal but opposite magnitudes of perpendicular velocity which cancel out. The first term on the right-hand side of the previous relationship disappears in a gyrotropic environment, and the energy rate becomes the following expression,

where $|\Delta\vec{v}|$ from Equation 2.18 has been substituted.

$$\Delta W_{\perp, res} = \frac{1}{2} \frac{q^2 E_{\perp}^2}{m} \Delta t^2$$

[Chang et al., 1986]

Before going on for completeness to find the resonant heating rate necessary for the guiding center motion, it should be stated that the previous gyrotropic requirement is not necessary in the model of this study which solves the exact equations of motion in a three-dimensional Cartesian environment without using this energization rate simplification. This allows for any initial, realistic distribution to be traced accurately, even if the distribution is not gyrotropic. This adds versatility and removes any inaccuracies which may come from an initial distribution that is not exactly gyrotropic in the guiding center approximation. This versatility could be useful in regions with non-gyrotropic distributions, such as the low E-region of the ionosphere St-Maurice and Schunk [1979]

Chang et al. [1986] goes on to substitute the spectral density at the gyrofrequency, make use of the relationship $\Delta f \Delta t \approx 1$, and cite Schulz and Lanzerotti [1981] in order to derive the commonly used resonant, transverse heating rate for the guiding center particle:

$$\dot{W}_{\perp, res} \approx \frac{q_i^2 |E(\Omega_c)|}{2m_i} \quad (2.19)$$

Chapter 3

Model Validation and Configuration

3.1 Model Validation

As an initial verification of the particle tracer's abilities, the following figure (Figure 3.1) displays three characteristic motions expected of magnetospheric ions: gyro, mirror, and drift motion (of a proton). Interestingly, since the initial conditions of this demonstration give the proton a surplus of transverse energy, each reflection point as the particle moves westward is farther along the field line as the particle's transverse energy decreases and gets converted to field-aligned energy. The mirror force takes longer and longer to reflect the particle which has less and less transverse energy.

Following, the tracer's numerical integrator and heating mechanism will be validated by the comparison to the analytical solutions of three different situations. The intermediate steps leading to the analytical solution of the second order ordinary differential equations are not included here, for brevity. Both situations include a uniform in space, constant in time magnetic field of magnitude $|\vec{B}|=|B_z\hat{z}|=60,000$ nT in a Cartesian environment. The first case includes a constant, perpendicular electric field, the second case includes a resonant, LHCP electric field wave in the transverse directions, and the third case includes the LHCP wave and a constant, parallel potential drop.

The first case involves a second order ordinary differential equation initial value

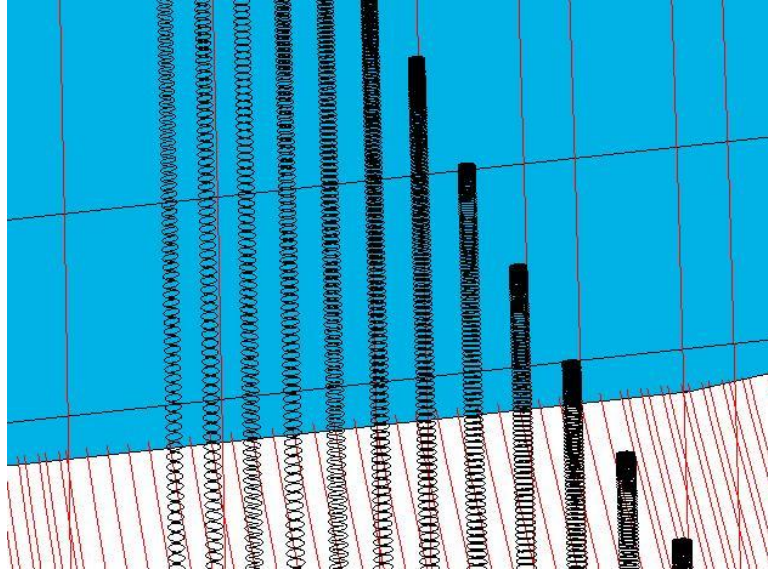


Figure 3.1: This is a demonstration of the expected gyro, bouncing, and drift motion that would occur for a non-heated proton in a simple dipole geomagnetic field after 1 hr 7 min with the initial conditions $x_0 = -2.3 R_E$, $y_0 = -3.3 R_E$, $z_0 = 0.55 R_E$, $v_{x0} = v_{y0} = 250 \text{ km s}^{-1}$, and $v_{z0} = 17.8 \text{ km s}^{-1}$. The trajectory drifts from east to west, as expected with the proton. The gyro-motion is counter-clockwise if viewed from below, as expected. A few of the trajectories seen here can actually be seen spiraling about a magnetic field line.

problem. With a constant electric field $|\vec{E}| = |E_x \hat{x}| = 1.5 \text{ mV m}^{-1}$, the initial conditions for the test O^+ ion are:

$$\vec{r} = x_0 \hat{x} + y_0 \hat{y} + z_0 \hat{z}$$

$$\vec{v} = v_{\perp} \hat{y}$$

Note here that all three cases presented below use a value of $v_{\perp} = -300 \text{ m s}^{-1}$ and begin at the origin.

The Lorentz force equations of motion for this first case are (note that $\Omega_c = \frac{eB_z}{m_o}$):

$$\begin{aligned}\frac{dv_x}{dt} &= \Omega_c \left(\frac{E_x}{B_z} + v_y \right) \\ \frac{dv_y}{dt} &= -\Omega_c v_x \\ \frac{dv_z}{dt} &= 0\end{aligned}$$

Solving, it can be shown that the position equations take form:

$$\begin{aligned}x(t) &= \frac{v_{\perp} + \frac{E_x}{B_z}}{\Omega_c} [1 - \cos(\Omega_c t)] + x_0 \\ y(t) &= \frac{-E_x}{B_z} t + \frac{v_{\perp} + \frac{E_x}{B_z}}{\Omega_c} \sin(\Omega_c t) + y_0 \\ z(t) &= z_0\end{aligned}\tag{3.1}$$

Figure 3.2 (constant magnetic field, constant transverse electric field) shows the expected $\vec{E} \times \vec{B}$ drift and the agreement between the analytical and numerical solutions. Figure 3.3 shows the accumulated numerical error as compared to the analytical solution of Equation 3.1 using time-steps which are different fractions of a gyro-period.

The second and third cases involve a similar second order initial value problem. The test O^+ ion experiences the same magnetic field as the previous case. The resonant LHCP electric field wave takes the form

$$\vec{E}_{\perp} = E_x \cos(\Omega_c t) \hat{x} - E_y \sin(\Omega_c t) \hat{y}$$

Here, $E_x = E_y = 1.5 \text{ mV m}^{-1}$. In the third case, there is a constant, field-aligned potential drop. Therefore the parallel electric field component E_z will be included in the following analytical solution which applies to both the second and third cases (with E_z set to zero in the second case). The total electric field, then, takes the

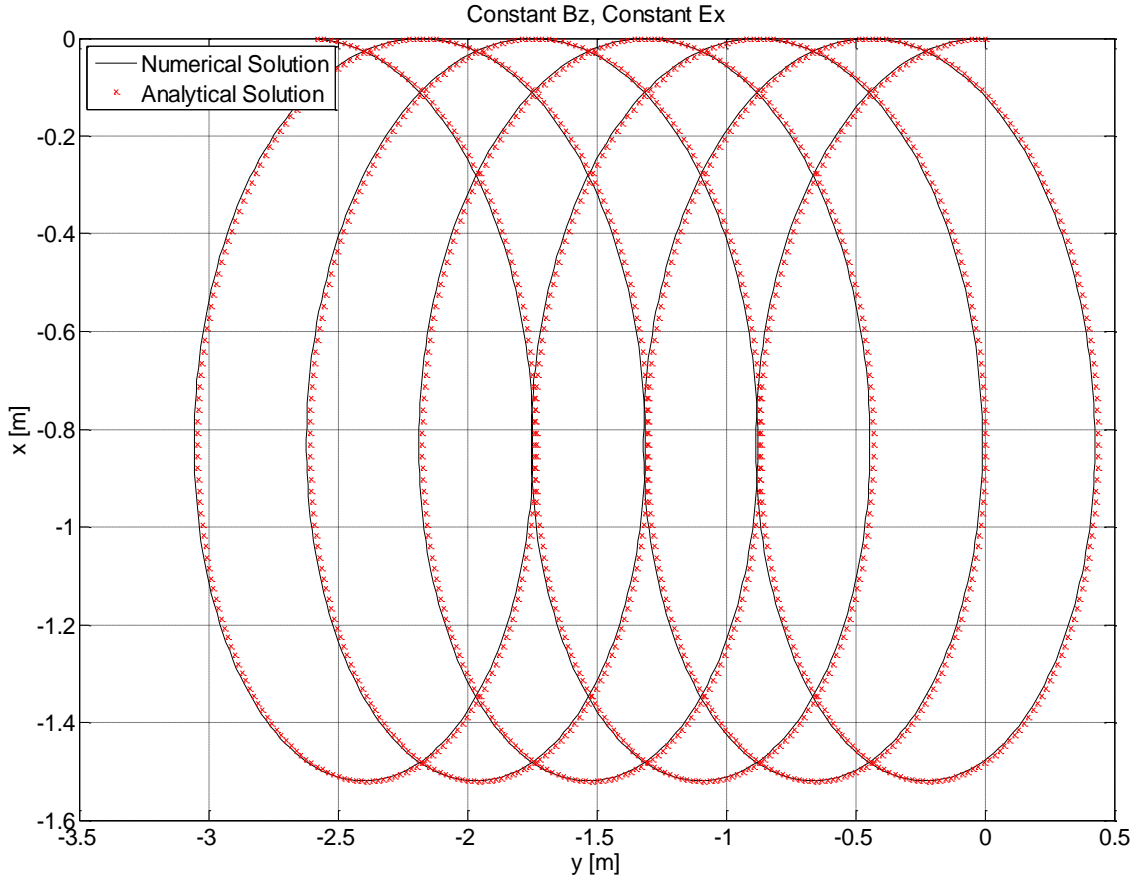


Figure 3.2: The expected $\vec{E} \times \vec{B}$ drift for an O^+ ion in a constant, uniform magnetic field $\vec{B}=B_z\hat{z}$ and a perpendicular, constant, uniform electric field $|\vec{E}| = |E_x\hat{x}|$. This is the case corresponding to Equation 3.1. The numerical solution uses time-steps that are $1/200$ of a gyro-period for these validation cases.

form:

$$\vec{E} = E_x \cos(\Omega_c t)\hat{x} - E_y \sin(\Omega_c t)\hat{y} + E_z\hat{z},$$

with $E_z=0$ in the second case and $E_z=0.1 \text{ mV m}^{-1}$ in the third case.

With the same initial conditions of position and velocity as the first case (above),

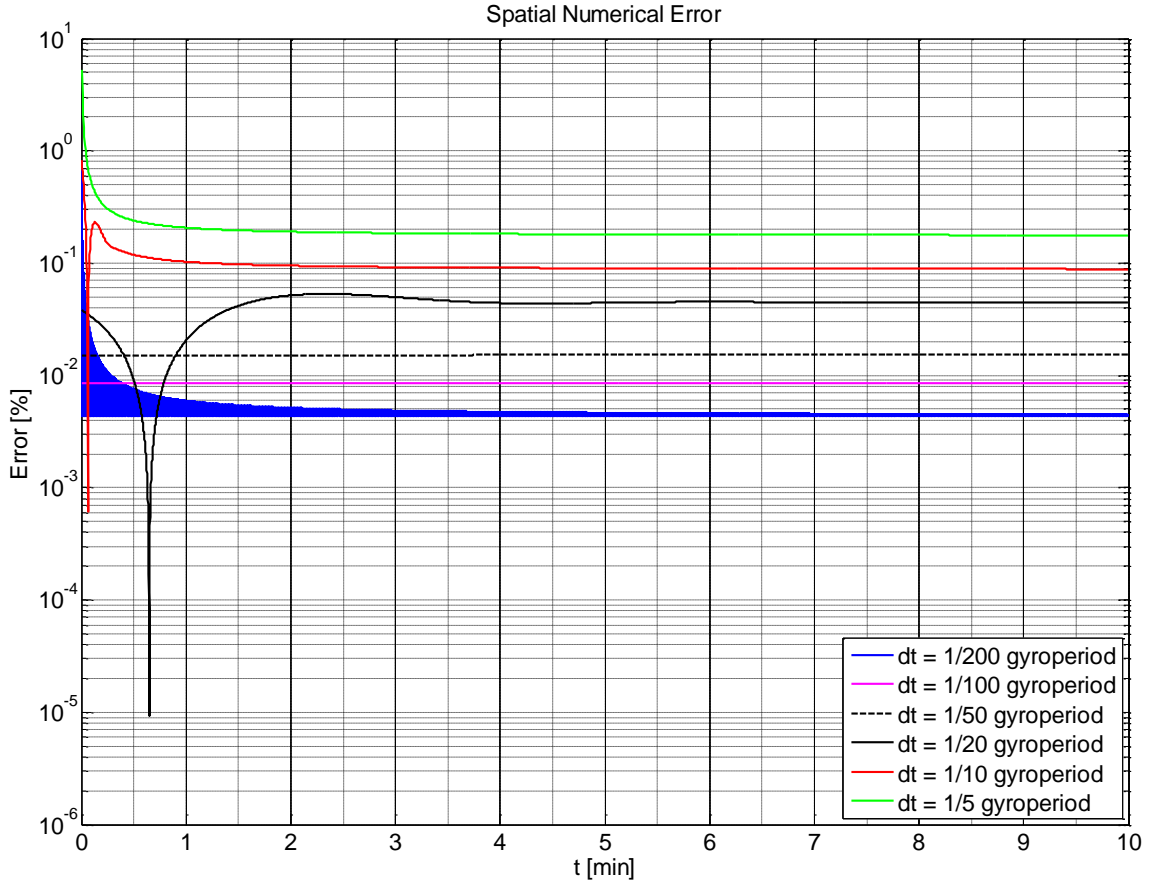


Figure 3.3: The numerical error after 10 min of tracing using different fractions of the gyro-period for the first case described above and in Figure 3.2

the equations of motion take the form:

$$\begin{aligned}\frac{dv_x}{dt} &= \Omega_c \left[\frac{E_x}{B_z} \cos(\Omega_c t) + v_y \right] \\ \frac{dv_y}{dt} &= -\Omega_c \left[\frac{E_y}{B_z} \sin(\Omega_c t) + v_x \right] \\ \frac{dv_z}{dt} &= \Omega_c \frac{E_z}{B_z}\end{aligned}$$

Solving, it can also be shown that the position equations for this situation take

form:

$$\begin{aligned}
 x(t) &= \frac{E_x + E_y}{2B_z} t \sin(\Omega_c t) + \left(\frac{E_y}{B_z \Omega_c} - \frac{v_\perp}{\Omega_c} \right) \cos(\Omega_c t) + \frac{v_\perp}{\Omega_c} - \frac{E_y}{B_z \Omega_c} + x_0 \\
 y(t) &= \frac{E_x + E_y}{2B_z} t \cos(\Omega_c t) + \left(\frac{v_\perp}{\Omega_c} - \frac{E_x + E_y}{2\Omega_c B_z} \right) \sin(\Omega_c t) + y_0 \\
 z(t) &= \frac{\Omega_c E_z}{2B_z} t^2 + z_0
 \end{aligned} \tag{3.2}$$

The second case (constant magnetic field, transverse electric wave field) which is shown in Figure 3.4 displays the expected increase in Larmor radius due to the transverse resonance heating by the LHCP electric field wave and the agreement between the analytical and numerical solutions. Figure 3.5 shows the accumulated numerical error as compared to the analytical solution of Equation 3.2 using time-steps which are different fractions of a gyro-period.

The third case which is shown in Figure 3.6 (constant magnetic field, resonant transverse electric field, field-aligned potential drop) displays the expected trajectory and the agreement between the analytical and numerical solutions. Figure 3.7 shows the accumulated numerical error as compared to the analytical solution of Equation 3.2 using time-steps which are different fractions of a gyro-period.

Next, a mirror point during incoherent energization in a simple dipole geomagnetic field is shown in Figure 3.8. In order to more easily zoom in on a mirror point, the transverse electric field reference value in this demonstration was increased to $|E_0|=10^{-1} \text{V}^2 \text{m}^{-2} \text{Hz}^{-1}$, at least 5 magnitudes larger than a typically used reference value (e.g. Zeng et al. [2006]).

Finally, the trajectory and properties of an O^+ ion which gets heated and leaves the heating region will be shown. A realistic reference value for the spectral density of $E_0^2=10^{-7} \text{V}^2 \text{m}^{-2} \text{Hz}^{-1}$ was used (the same as Zeng et al. [2006]). It has initial conditions: altitude = 7500 km, geographic latitude = 74.9° , longitude = 0° , $v_{x0} = 250 \text{m s}^{-1}$, $v_{y0} = -300 \text{m s}^{-1}$, $v_{z0} = 1.2 \text{km s}^{-1}$.

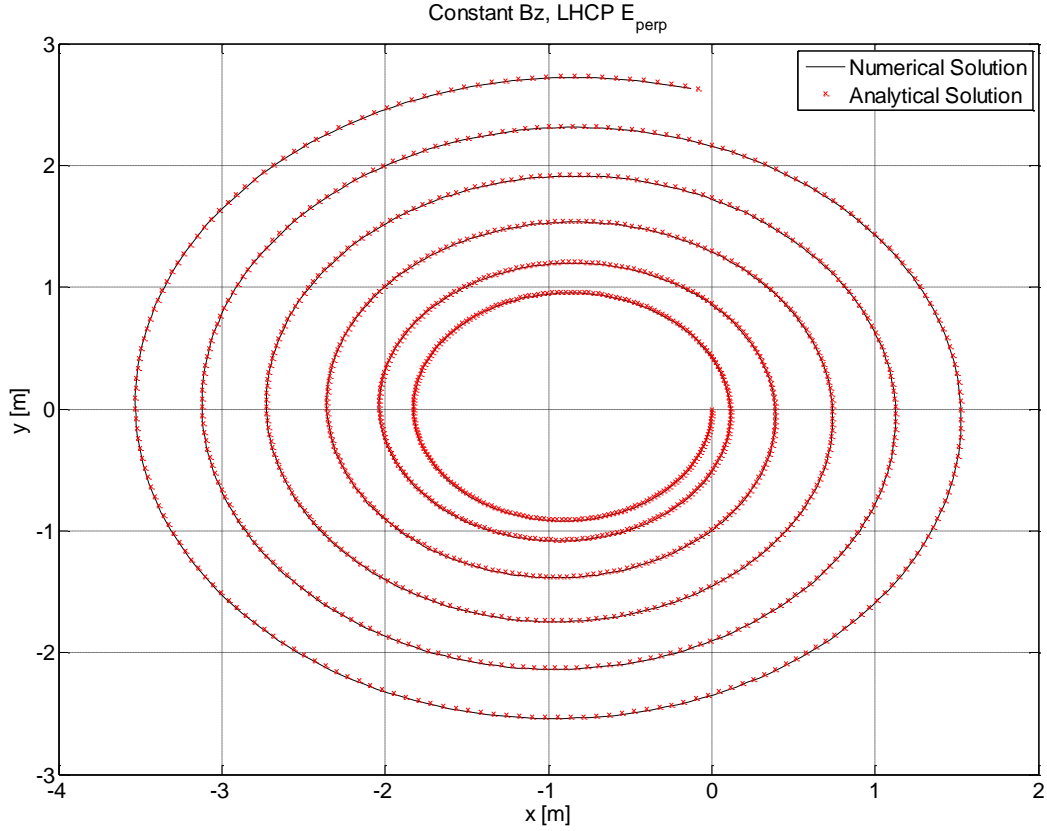


Figure 3.4: The expected increase in Larmor radius for an O^+ ion in a magnetic field of $\vec{B}=B_z\hat{z}$ and a resonant, LHCP electric field of $\vec{E} = E_x \cos(\Omega_c t)\hat{x} - E_y \sin(\Omega_c t)\hat{y}$. This is the case corresponding to Equation 3.2 with E_z set to zero. The numerical solution uses time-steps that are 1/200 of a gyro-period.

3.2 Configuration

Note first that, during the main study (Chapter 5), the flux tube that makes up the simulation region extends from 800 km to 3-4 R_E altitude and 0.001° in geographic latitude and longitude (geomagnetic latitude and magnetic local time are impending future modifications). Within the flux tube, the initialization region extends either from 1000 km to 1750 km or from 1000 km to 8000 km altitude, and the transverse heating region extends from 1000 km to 10,000 km altitude as well as from 72° to 75° longitude [Bouhram et al., 2004]. The altitudinal extent of these

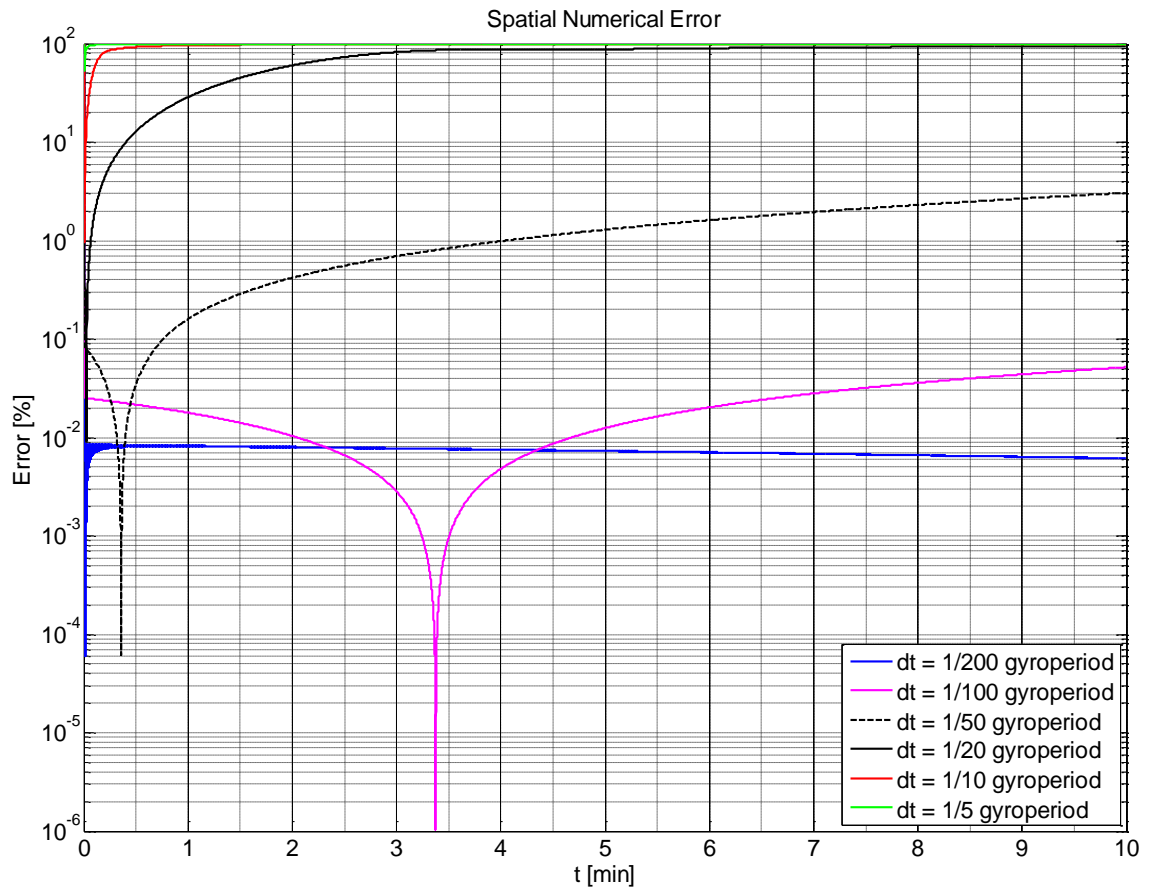


Figure 3.5: The numerical error after 10 min of tracing using different fractions of the gyro-period for the second case described above and in Figure 3.4.

regions are similar to those used by, for example, Wu et al. [2002] and Bouhram et al. [2002].

In order to procure physically meaningful distribution functions with a single particle model, a realistic initial distribution of ions needs to be constructed. To this end, efforts were made to replicate a real plasma environment by imposing a number density which decays exponentially with altitude upon the initial ion distribution in the following way.

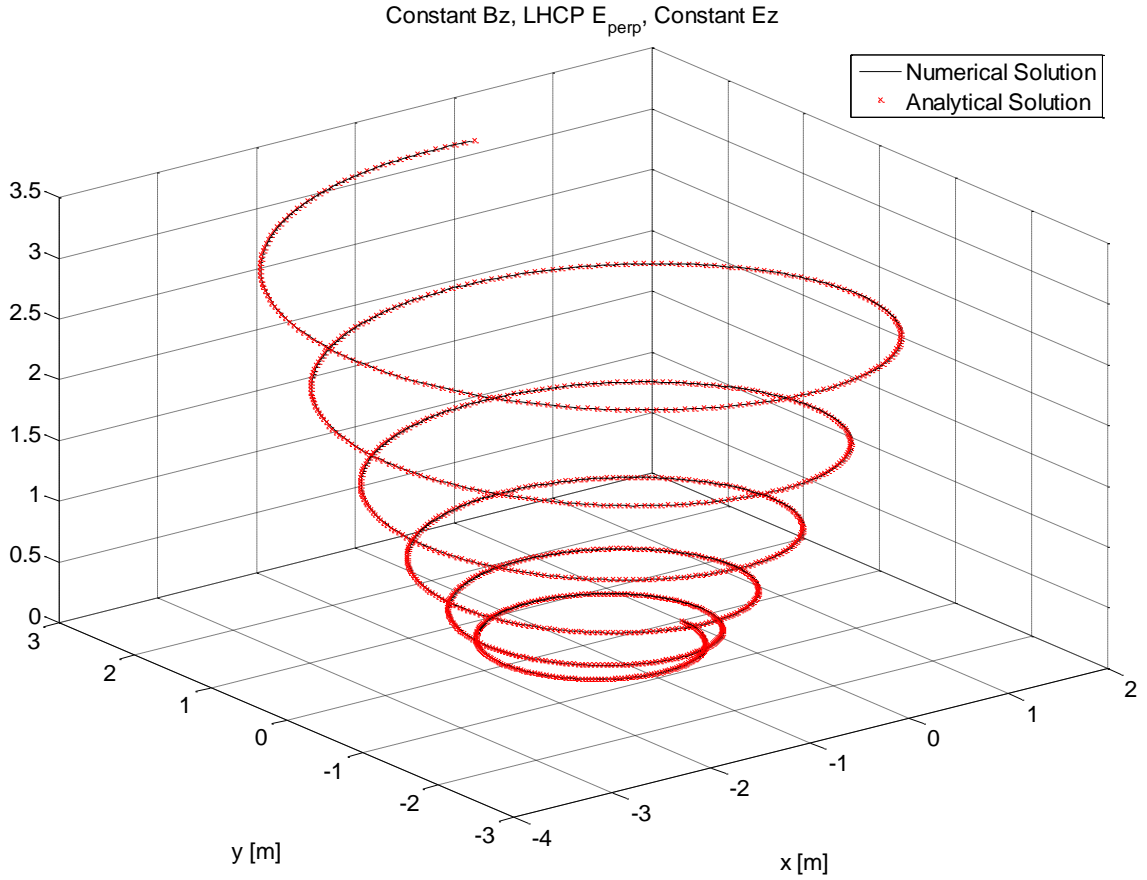


Figure 3.6: The expected trajectory of an O^+ ion in a magnetic field of $\vec{B}=B_z\hat{z}$, a resonant, LHCP electric field of $\vec{E} = E_x \cos(\Omega_c t)\hat{x} - E_y \sin(\Omega_c t)\hat{y}$, and constant field-aligned potential $E_z\hat{z}$. This is the case corresponding to Equation 3.2. The numerical solution uses time-steps that are $1/200$ of a gyro-period.

Firstly, the number density of O^+ was assumed to change according to

$$n(r) = n_0 e^{-\frac{(r-r_0)GM_E m_0}{k_B T_0 r^2}}. \quad (3.3)$$

[Kivelson and Russel, 1995]

Here, n_0 and T_0 are reference values of oxygen ion number density and temperature at $r_0 = 1000 \text{ km} + 1 R_E$ geocentric distance. The currently used temperature

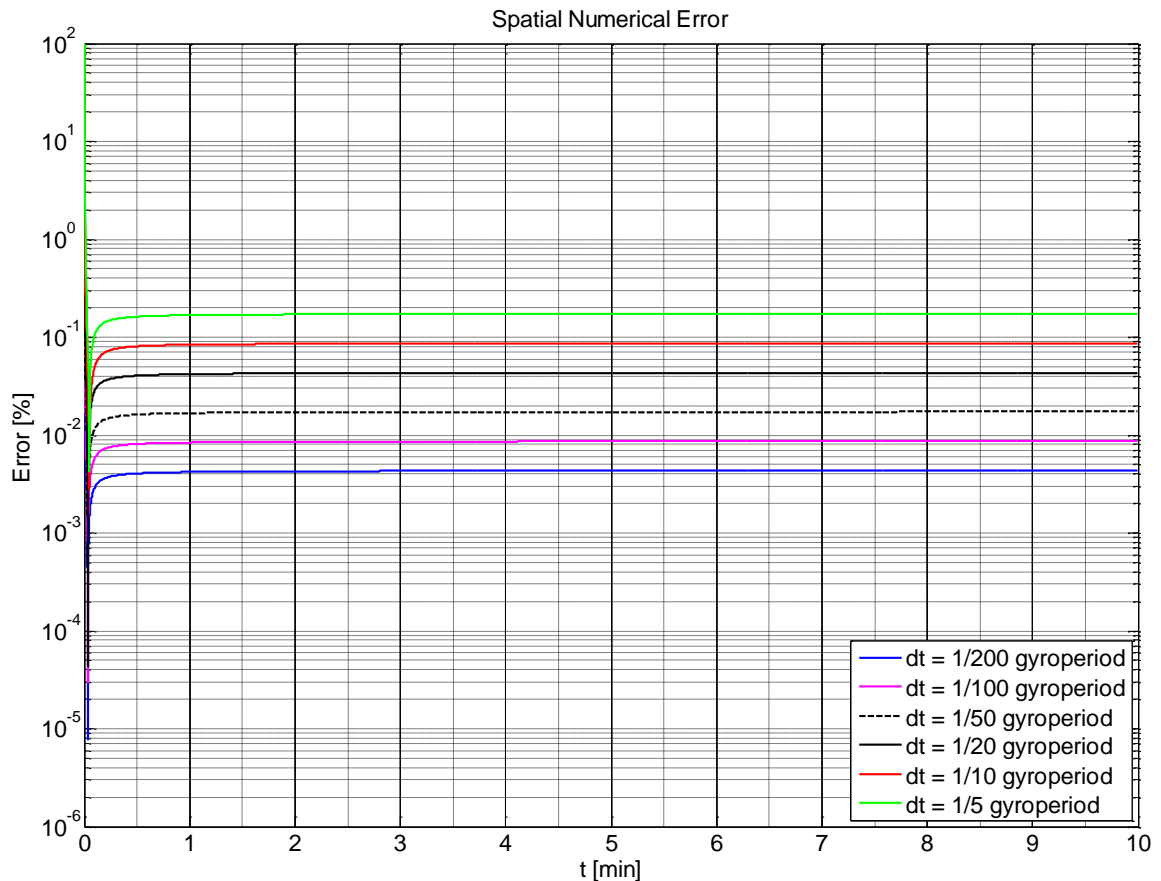


Figure 3.7: The numerical error after 10 min of tracing using different fractions of the gyro-period for the third case described above and in Figure 3.6. Interestingly, this case that has the most terms in the analytical solution has the smallest error of the three cases (although all cases have good error).

value is $T_0 = 4000$ K at r_0 , while n_0 is used as an adjustable parameter which specifies the size of the simulation. G is the gravitational constant, and k_B is Boltzmann's constant. Number density reference values used were typically in the range of 50 to 1200 macroparticles km^{-3} in order to keep simulation runtimes around 24 hours for traces up to 25 minutes. The total number of macroparticles ranged from about 100,000 to 2,150,000, depending upon the particular simulation.

The initialization region, which is delimited by geocentric latitude and longitude in the current model, was divided into either 20 cells for the region extending

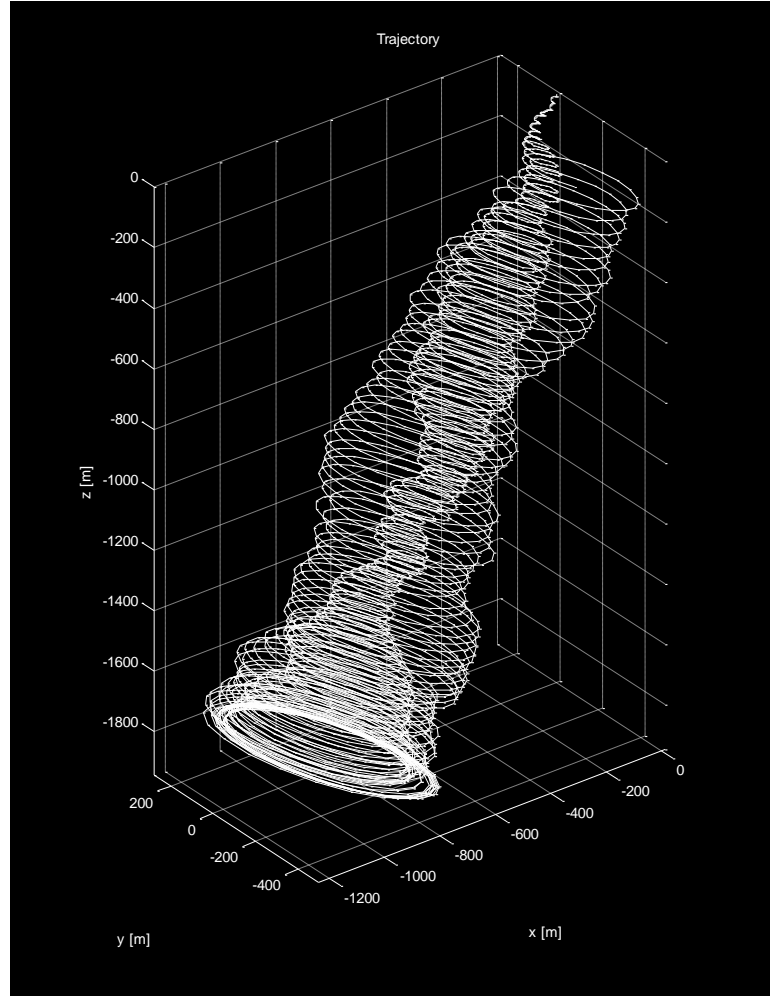


Figure 3.8: Mirror point of an incoherent transversely energized oxygen ion with $E_0^2=10^{-1} \text{ V}^2 \text{ m}^{-2} \text{ Hz}^{-1}$ at an altitude of 1050 km, geographic latitude and longitude 74.9° and 0° , and velocity components $v_{x0}=250 \text{ m s}^{-1}$, $v_{y0}=-300 \text{ m s}^{-1}$, and $v_{z0}=-1 \text{ km s}^{-1}$.

from 1000 km to 1750 km or 100 cells for the initialization region between 1000 km to 8000 km. The number of particles in each cell was found via the relationship

$$N_{cell} \approx V_{cell} \cdot n(r_{cell}),$$

where r_{cell} is the geocentric distance to the mid-altitude point of each cell. Each cell is in the shape of a spherical element because it is created by a finite expanse of

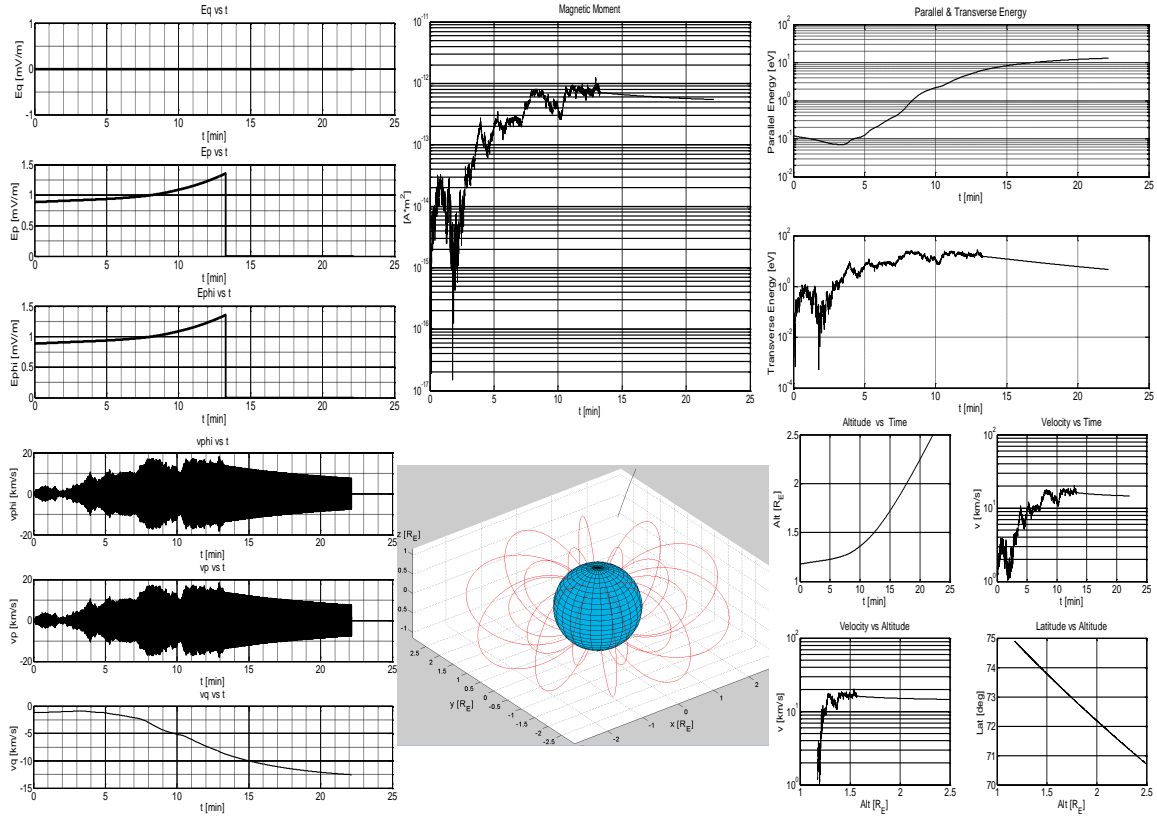


Figure 3.9: Properties of an incoherently heated O^+ ion which leaves the realistic heating region after 13 min. A particle with the same initial conditions reached a peak altitude of $31.4 R_E$ after 2.3 days, and followed the field line back to the southern latitude Earth ionosphere (-75.8°) at 100 km altitude after 4.5 days. Notice the magnetic moment is not constant until the ion leaves the non-adiabatic heating region.

each spherical direction. Therefore, the volume of each element should be found by the relationship

$$V_{cell} = \int_{r_b}^{r_t} \int_{\theta_1}^{\theta_2} \int_{\phi_1}^{\phi_2} r^2 \sin \theta dr d\theta d\phi = \frac{r_t^3 - r_b^3}{3} (\cos \theta_1 - \cos \theta_2) (\phi_2 - \phi_1) \frac{\pi}{180}.$$

Here, θ_1 and θ_2 are the lower and upper latitude boundaries. ϕ_1 and ϕ_2 are the longitudinal boundaries (in degrees). The terms r_b and r_b are the radial distances to the bottom and the top of the spherical element altitude cell. For the results of

this study, the volume of a truncated pyramid was used as an estimate instead. This estimation is fairly accurate, but it is not necessary to estimate the volume. The change to the more accurate spherical element volume has been made in the model for future simulations.

Each cell's initial ion distribution was calculated with a uniform, random number generator over the range of geographic latitude, longitude, and altitude. Although these ions are not initialized gyrotropically (uniform in the transverse directions), the heating mechanism is still valid (as described in Section 2.4.2).

The initial conditions of velocity for all simulations of this study are chosen to resemble that of a particular type-I, Joule-heated upflow, which would likely be the source of the O^+ to the transverse heating region. With a uniform, random number generator, the initial $v_z = 1 \text{ km s}^{-1} \pm 0.1 \text{ km s}^{-1}$, while $v_x = v_y = \pm 0.5 \text{ km s}^{-1}$ [Kosch et al., 2010]. This initial velocity corresponds to an initial total energy of 0.124 eV. These initial conditions are subject to two future modifications: initializing the velocities in field-aligned and transverse directions, and using a Gaussian random number generator to produce the initial velocities.

Chapter 4

Results: Mapping to the Magnetosphere

This short chapter serves to briefly demonstrate the preliminary results from the adaptation of the model which uses CCMC: BATSRUS Global Magnetosphere model output in order to show this model's ability to trace transversely heated, outflowing ions throughout a realistic magnetosphere. This particle tracer has an advantage over the guiding center approximation for this aspect of the study which maps ions far into the magnetosphere; the large Larmor radii at large altitudes cause error in the trajectory calculation for the guiding center particle if there is a significant difference in magnetic field value over the distance of one Larmor radius.

The BATSRUS model uses GSM coordinates, and therefore the positive x -axis is oriented toward the sun, with the positive z -axis coincident with the northward magnetic dipole axis of the Earth's magnetosphere. The interpolation, as mentioned in Section 2.1, is relatively computationally costly as compared to the dipole model (it can only trace around three orders of magnitude less particles than the dipole model during an equivalent runtime). It was therefore not possible to run simulations large enough to be classified as Monte Carlo simulations due to the limited time to obtain results with the current amount of available computation power. So, a multiple-trajectory, single particle trace of hundreds of particles were performed to provide a qualitative demonstration of the model's potential to map

a large amount of particles throughout a realistic magnetosphere. Determining the ionospheric outflow's destination is a useful capability for topics of research such as the effects of ionospheric O^+ outflows upon ionosphere and magnetosphere composition changes or upon the process of magnetic reconnection that occurs in the magnetotail, as discussed in Chapter 1. The main result of this aspect of the study, besides a qualitative demonstration of the model's potential capabilities, is an approximation of escape probability for topside ionospheric O^+ ions.

4.1 Presentation of Ionosphere-Magnetosphere Coupling Trajectories

The BATSRUS .cdf output file chosen depicts the Earth's magnetosphere during a geomagnetic storm which occurred on April 5, 2010. The particular snapshot is at 09:15:00. At this time, a plasmoid has just been ejected (the file is displayed in Figure 2.3). The K_p index reached 5 during this time, and a maximum of 8 during geomagnetic storm. (Obtained from <ftp://ftp.gfz-potsdam.de/pub/home/obs/kp-ap/wdc/>)

In order to decide upon initial conditions for the main particle trace, the region of the high latitude, topside ionosphere which is most apt to produce outflows was sought. A simulation which traced about 10,000 incoherently transversely energized O^+ ions for five minutes was run with an initialization region which includes all longitudes and a geographic latitude range from 45° to 85° . The latitude and longitude position with the highest average final altitude after five minutes of transverse heating was found to be from about 73.3° to 73.6° latitude and about 231° to 239° longitude (a snapshot of the three-dimensional visual model from a simulation that was used to narrow down these boundaries is shown in Figure 4.1).

These boundaries agree with the expectation of the high energy outflows which tend to occur in the high latitude, midnight polar cap boundary region (here, the pre-dawn sector). These boundaries were therefore used as the latitudinal and

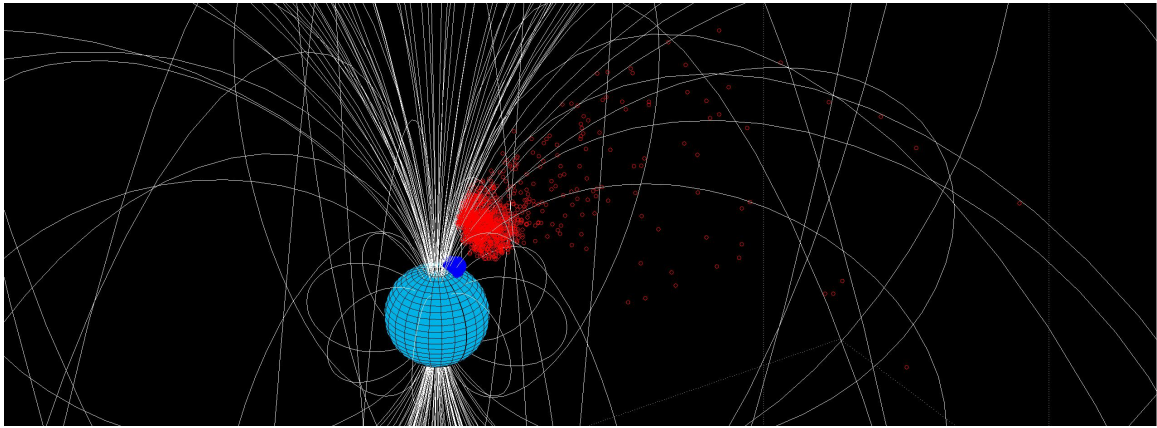


Figure 4.1: Initial (blue) and final (red) ion positions are displayed here for a study which was used to pinpoint the initialization region boundaries that are most conducive to the production of high energy outflows for the main simulation. Longitude boundaries of this preliminary trace are 192° to 268° (GSM), with geographic latitude boundaries 63.5° to 81.5° , and initial altitudes of 1000 km to 1200 km. The location resulting in the highest final altitudes here were 73.3° to 73.6° latitude and about 231° to 239° longitude.

longitudinal dimensions of this chapter's main simulation's initialization region. The altitude range in this test simulation was from 1000 to 10,000 km, and it was found that total altitude gain increased approximately linearly with initial altitude. However, an altitude range of 1125 to 1135 km was used in the simulation. This range was used for comparative purposes; many of the results of the Monte Carlo simulations of Chapter 5 also used this altitude range.

With the above initial latitudinal, longitudinal, and altitudinal boundaries of 73.3° to 73.6° , 231° to 239° , and 1125 km to 1135 km, 2280 transversely heated O^+ ions were traced for 35 min throughout the BATSRUS magnetosphere during geomagnetic storm described above. The initial x and y components of velocity ranged randomly and uniformly from $\pm 500 \text{ m s}^{-1}$, and the z component of velocity ranged from $1000 \pm 100 \text{ m s}^{-1}$ (in attempt to roughly imitate the conditions of an O^+ supplying ionospheric upflow [Kosch et al., 2010]). The heating region extended from 1000 to 15,000 km and from 71° to 74° geographic latitude (particles decrease in geographic latitude as they increase in altitude due to the incongruency between the geometrically determined latitude and the magnetically determined

geomagnetic latitude). The spectral density reference value used was $10^{-5} \text{ V}^2 \text{ m}^{-2} \text{ Hz}^{-1}$. The maximum Larmor radius was limited to 10 km due to the BBELF wave finite radius effects mentioned in Chapter 2.

With this small, demonstrative study, the probability of ionospheric ion escape resulting from incoherent transverse acceleration was found (see Figure 4.5). The particles would either traverse to the edge to the BATSRUS .cdf file in the magnetotail which is stretched to the northward BATSRUS boundary as shown in Figure 2.3 (over $175 R_E$), or they would become trapped along field lines in the high latitude region below $1 R_E$ altitude. For this reason, computational expense was saved by stopping the tracing of particles which reach altitudes greater than $50 R_E$. After the 35 min, 78.5% of the energized ions remained gravitationally bound below $1 R_E$ altitude between geographic latitudes of 66° to 73° and GSM longitudes of 230° to 239° , 3.25% of the ions were in transit to the $50 R_E$ outflow termination altitude, and the remaining 18.25% passed through the $50 R_E$ between geographic latitudes of 7.5° to 9° and GSM longitudes of 188° to 190.5° (see Figures 4.2, 4.3, and 4.4).

Notice that the energetic outflow trajectories remained closely together in their transit to $50 R_E$. In reference to Figure 4.4, it can be observed that the magnetic field lines spanning the approximate range of 65° to 73° geocentric latitude below $1.5 R_E$ altitude must converge to the latitude range of about 8° to 8° at $50 R_E$ altitude. Future applications should quantitatively determine regional probabilities of outflow destination in the magnetosphere (and should therefore use the full extent of the BATSRUS .cdf file's magnetotail).

The simulation presented in this chapter is not really conducive to make many valid or effective comparisons to other, similar particle traces of these transversely heated O^+ ions such as Huddleston et al. [2005] and Ebihara et al. [2006] simulations. For example, Ebihara gives probabilistic destinations of outflowing ions for the regions: atmosphere, ring current, magnetopause, and magnetotail. In this study, probably due to the BATSRUS magnetosphere's configuration and its recent release of a plasmoid, the ions either stay below $1 R_E$ or they escape to the distant magnetotail that is northwardly elevated (in the positive z direction) due to the simultaneously occurring severe magnetic reconnection and geomagnetic storm.

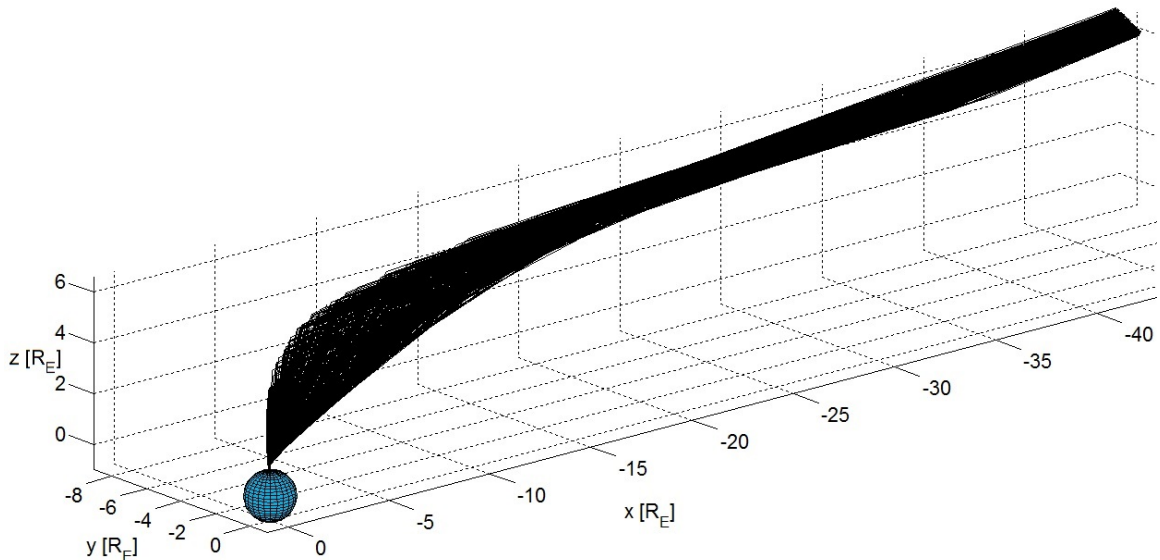


Figure 4.2: (Main ion mapping simulation) Spatial visual display of transversely heated outflow trajectories in a BATSUS magnetosphere mapped throughout a geomagnetic storm which occurred on April 5, 2010. The outflowing ions would continue to the end of the BATSUS magnetosphere through the north boundary at an altitude near $175 R_E$ if traced further, because of the unusual magnetospheric configuration during this snapshot (see Figure 2.3).

These regional probabilities do not really align with Ebihara's regional probabilities due to the different magnetosphere situations. The most similar magnetospheric condition in Ebihara's paper was at solar maximum and $K_p = 8$. The destination probabilities in this case were: Magnetopause 41%, Distant tail 8.6%, Ring current 49%, and Atmosphere 0.8%.

Also, the scope of this aspect of the study did not analyze the energies of the particles that were mapped to the magnetosphere (the current model only output the particle position and time), so a comparison to Ebihara or Huddleston's energies without doing some additional analysis and estimation upon the output files is necessary. Further adapting the model to output ion velocity is the alternative option.

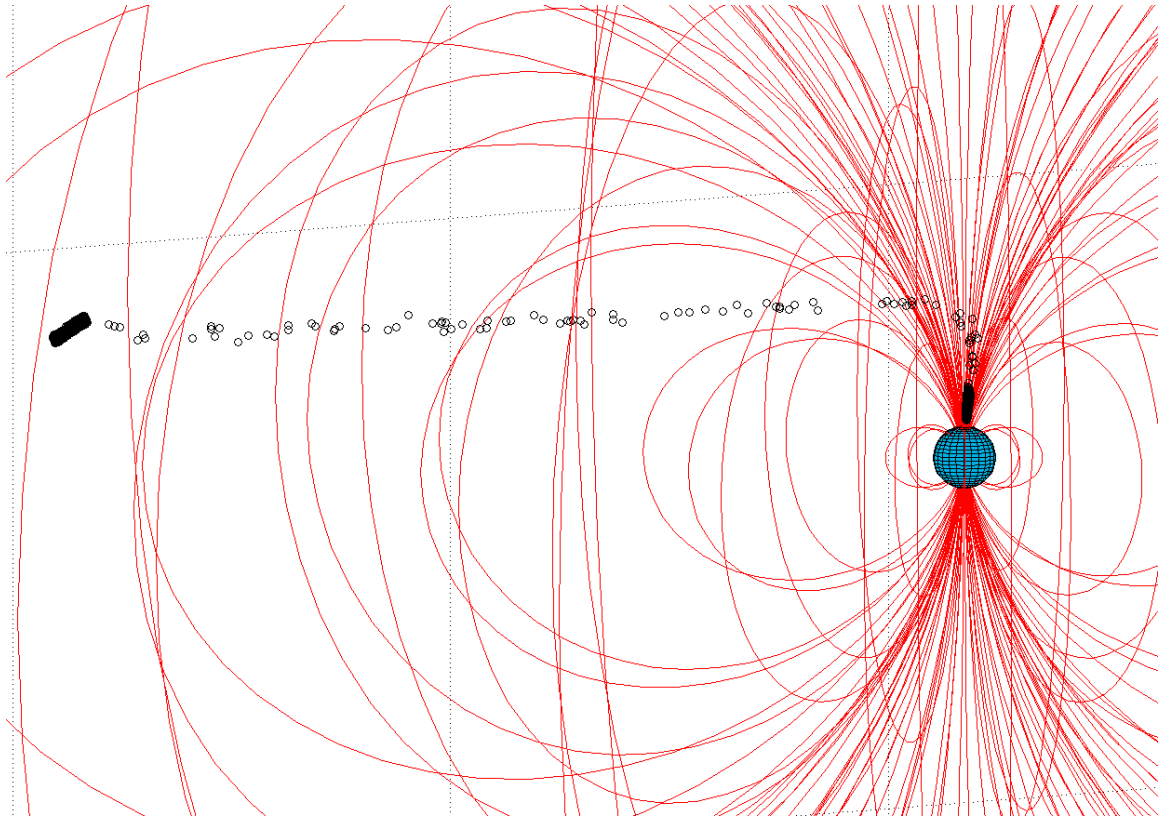


Figure 4.3: (Main ion mapping simulation) Final ion positions are plotted in this visual display. The field lines shown are not representative of the BATSRUS magnetosphere, but rather serve to display the negative longitudinal curve the outflow follows throughout the magnetosphere (the blue circles are marginally visible).

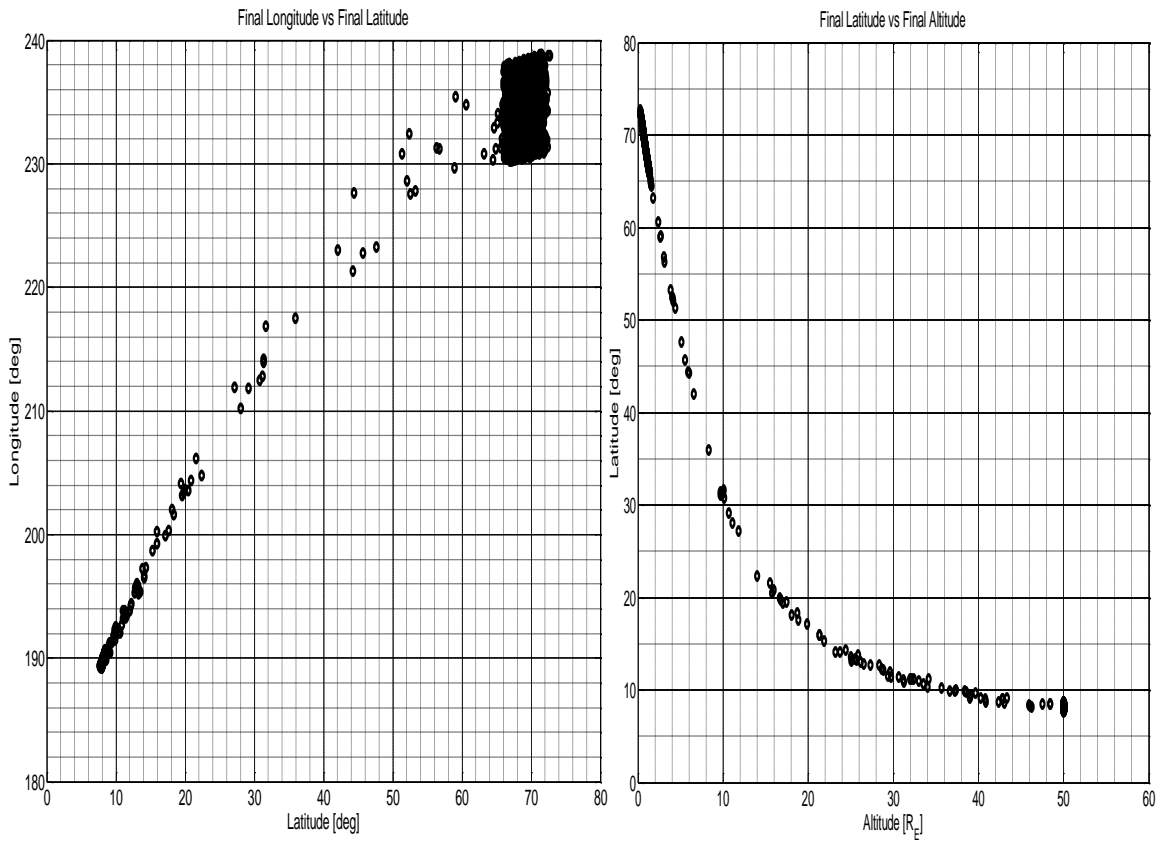


Figure 4.4: (Main ion mapping simulation) Relationship of final geographic latitude and GSM longitude with respect to altitude.

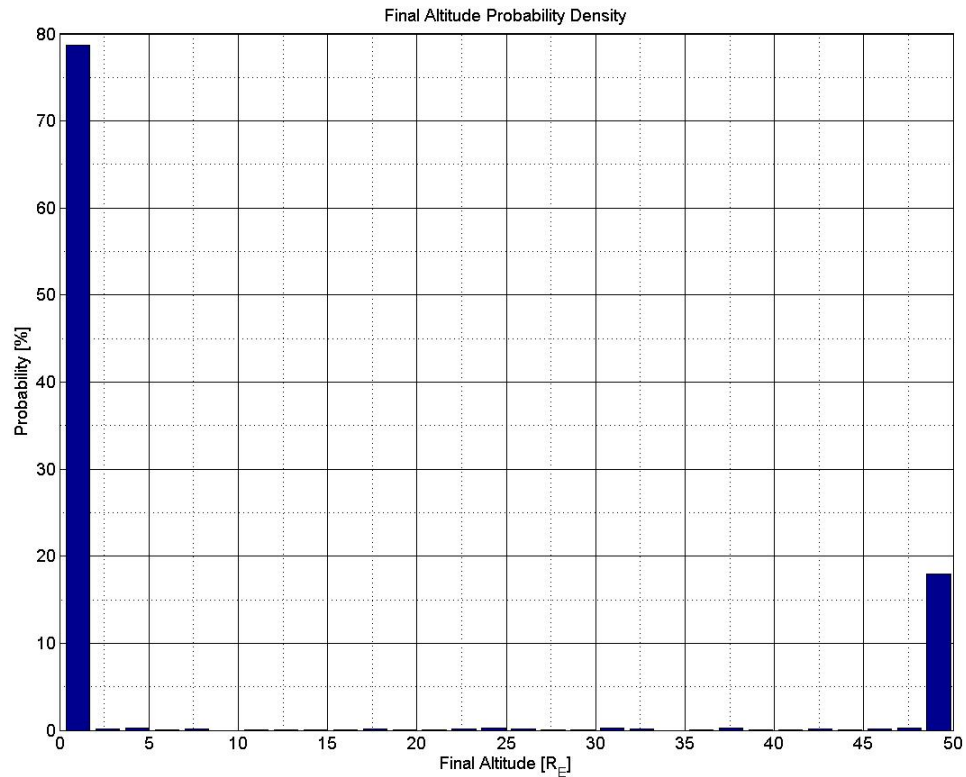


Figure 4.5: (Main ion mapping simulation) Probability of altitude destination for 2280 outflowing O^+ ions during the geomagnetic storm on April 5, 2010. Note again that trajectories were stopped once an altitude of $50 R_E$ was attained. This figure reflects the simulation's purpose to determine probability of ionospheric oxygen ion escape to the magnetosphere due to transverse energization.

Chapter 5

Results: Monte Carlo Simulations

This chapter serves to demonstrate the capabilities of the tracer by first presenting a qualitative display of some highly detailed, non-Maxwellian velocity distribution functions followed by the presentation of some more quantitative, realistic results. The distribution functions display the number of particles in each velocity bin at each altitude and time-step. Each Monte Carlo simulation calculated the trajectories of some total number of particles between about 100,000 and 2,150,000 macroparticles, depending upon the particular simulation (numbers of particles outside of this range of numbers were used but are not documented in the figures presented here). If a realistic ion density at 1000 km altitude is considered to be about 100 cm^{-3} , the macroparticles in the very best case represented at least 10^{11} particles. Although this macroparticle correlation may not seem likely to produce high quality statistics, only the shape of the distribution function was sought in this qualitative study, and the fact that many particles are in each altitude bin for the output presented below suggests that the number of particles launched were sufficient for the qualitative intentions of this study. In order to produce quantitative results, the distribution functions must be normalized. This would entail dividing the unnormalized distribution functions by the velocity and altitude bin sizes as well as discarding particles which leave the simulation's velocity and altitude bin limits, and a more realistic number density would then be desirable.

The first, more qualitative section of this chapter uses partially or fully coherent energization wave fields, while the more quantitative result of the following section uses a more realistic, fully-incoherent energizing wave field. Some additional results show some possible effects of a parallel potential drop or pulse. The perpendicular velocity component in the simulations of this chapter is the v_p component.

The appropriate model parameters to obtain results that most closely resembled the expected results were not found until the end of the effort. That is, the altitudinal extent of the particle initialization region was increased from the range of 1000 to 1750 km to a range of 1000 to 8000 km toward the end of the study. This change created much more energetic outflows because of the weaker gravitational and transversely energizing electric fields which the ions experience at higher altitudes.

The heating region extends from 1000 km to 10,000 km. Its geographic latitudinal limits are 72° and 75° . The particles, if sufficiently energized, usually exit the heating region (but not the simulation region) through the lower latitude boundary before they reach the top of the region at 10,000 km. If not sufficiently energized, the particles will either remain in the heating region for the entire duration of the simulation or exit the heating region at the lower altitude boundary. Particles that were accelerated outside of the altitudinal or velocity components' bin boundaries were discarded, because these are the three parameters being examined. As mentioned in previous chapters, the initial conditions of velocity are chosen to resemble that of a particular type-I, Joule-heated upflow, which would likely be the source of the O^+ to the transverse heating region. With a uniform, random number generator, the initial $v_z = 1 \text{ km s}^{-1} \pm 0.1 \text{ km s}^{-1}$, while $v_x = v_y = \pm 0.5 \text{ km s}^{-1}$ [Kosch et al., 2010].

Table 5.1 provides a list of the different cases in this chapter and their distinguishable properties.

Table 5.1: List of Cases. Note that cases not displayed in a figure but mentioned in the text, such as the case of fully coherent energization, are not listed here.

Case	Figure	ϵ Range	E_0^2 [$V^2 \text{ m}^{-2} \text{ Hz}^{-1}$]	E_q [mV m^{-1}]	Initialization Altitudes
1	5.1, 5.2	$\pm \frac{\pi}{2}$ rad	2×10^{-5}	0	1000 - 1750 km
2	5.3	$\pm \frac{\pi}{2}$ rad	2×10^{-5}	0.0067	1000 - 1750 km
3	5.4	$\pm \pi$ rad	2×10^{-4}	0	1000 - 8000 km
4	5.5, 5.6	$\pm \pi$ rad	2×10^{-5}	0	1000 - 8000 km
5	5.7	$\pm \pi$ rad	2×10^{-4}	0	1000 - 1750 km
6	5.8	$\pm \pi$ rad	5×10^{-5}	0	1000 - 1750 km
7	5.9, 5.10	$\pm \pi$ rad	3×10^{-5}	0.0067	1000 - 8000 km
8	5.11	$\pm \pi$ rad	5×10^{-5}	-10	1000 - 1750 km

5.1 Detail in Highly Non-Maxwellian Velocity Distributions

The simulations of this section are presented to demonstrate the model's capability to produce some highly non-Maxwellian structures which make up velocity distribution functions that result from this transverse heating process. The initialization region used in the simulations of this section is from 1000 km to 1750 km. The cases examined below have a range of phase incoherency of the energizing LHCP wave is $\epsilon = \pm \pi/2$ rad; this particular range of phase incoherency will be referred to as partially coherent, because the transverse wave field has a randomized phase which is limited to a range of incoherency. Some interesting substructures form during the development of the ion conic distribution functions. Some conclusions that can be drawn from the observed effects of coherency upon the energization rate and energization magnitude will be discussed here as well as in Chapter 6. In general, the coherency causes a faster conversion from transverse to parallel energy, but the magnitude of energization is not significantly larger than with the fully incoherent case.

The physical justification for any coherency is questionable. Due to the developmental state of the model during the results phase of this thesis effort, many of the results that were obtained used the unjustifiable assumption of partial coherency in order to produce appreciable outflows with a relatively short runtime; nearer the end of the effort, it was discovered that the model still predicts similar outflows using full incoherency, if initialized properly. Exploring the effects of a wide range of degrees of coherency also allowed for the display of some effects upon distribution functions for the range of physical possibility within $\epsilon = \pm\pi$ rad.

The first simulation to be presented here in Figure 5.1, Case 1, is the case using partially coherent transverse energization ($\epsilon = \pm \pi/2$ rad). The distribution functions presented in the 15 snapshots in time increase in time (not at a constant rate) from left-to-right, top-to-bottom for the constant altitude bin which spans the range from 1000 km to 1140 km (note that following figures will not have this same layout). 2,150,000 O^+ ions that are initialized from 1000 to 1750 km are traced for 1 min with a spectral density value of $E_0^2 = 2 \times 10^{-5} \text{ V}^2 \text{ m}^{-2} \text{ Hz}^{-1}$.

The complex substructures seen during the first minute of transverse energization in Figure 5.1 are apparently a result of coherency; any coherency in the energization process causes certain ions to be in phase with other ions at certain times. This is because the ions are initialized with energies that are effectively negligible in comparison to the energies obtained from energization, and therefore the energizing wave that has a randomized phase which is restricted to the range $\epsilon = \pm \pi/2$ rad will energize all of the ions only to certain allowed energies. The substructures do not form during fully incoherent energization because the phase of the energizing wave—and therefore the phase of the energized ions—does not restrict the range of possible energies.

Further examination of Figure 5.1 shows that the parallel velocity steadily increases and remains roughly constant in span throughout this initial minute of energization. Interestingly, this partially coherent case uniquely exhibits a series of expansions and contractions in transverse velocity space; more specifically, the distribution function shows an initial expansion in the range of transverse velocity

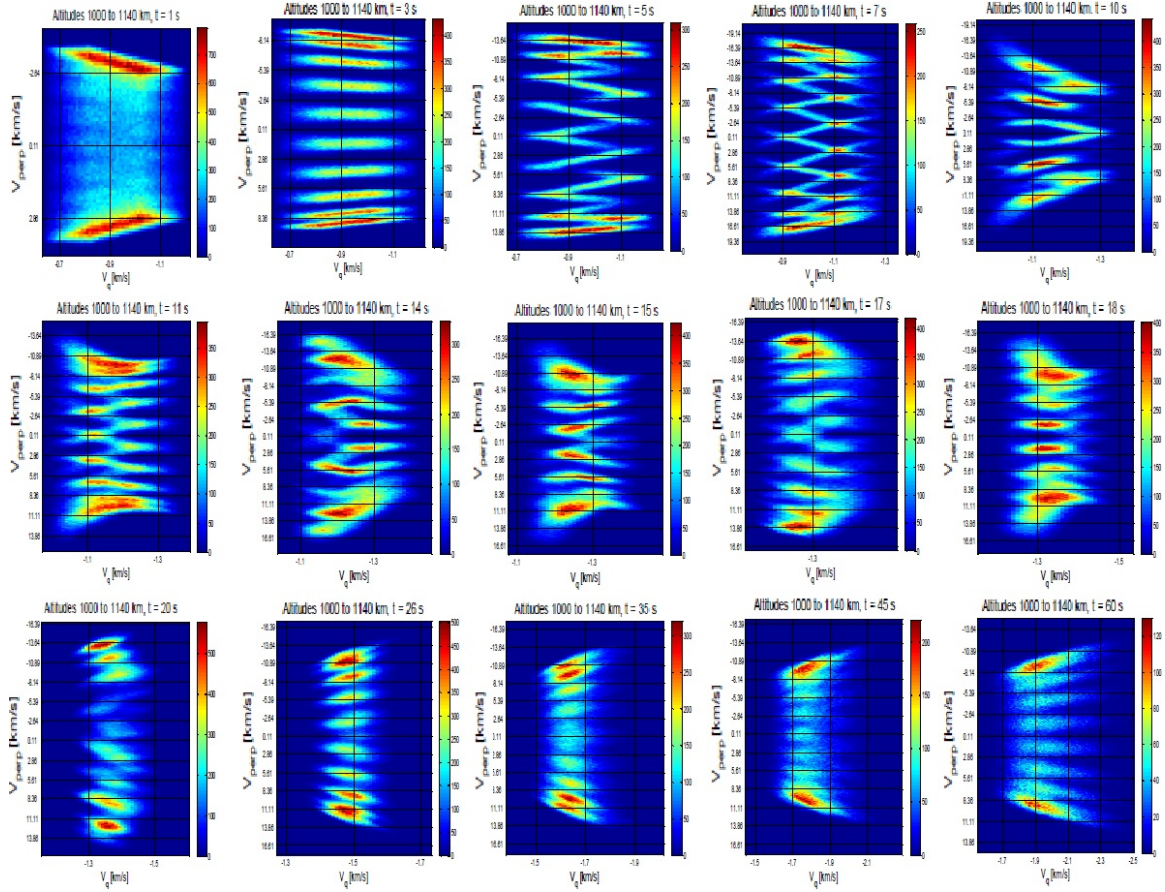


Figure 5.1: Case 1. Demonstration of the model's ability to produce highly detailed, non-Maxwellian distribution functions. The above 15 snapshots in time show the initial development of distribution functions due to partially coherent transverse energization ($\epsilon = \pm \pi/2$ rad) for a simulation of about 2,150,000 particles that are initialized from 1000 to 1750 km and traced for 1 min. The color axis represents the number of particles in each velocity bin. The transverse electric field spectral density reference value $E_0^2 = 2 \times 10^{-5} \text{ V}^2 \text{ m}^{-2} \text{ Hz}^{-1}$.

to a maximum of approximately $\pm 19 \text{ km s}^{-1}$ after 7 s, a subsequent contraction in transverse velocity space to $\pm 10.5 \text{ km s}^{-1}$ after 11 s, then another increase to about $\pm 16.5 \text{ km s}^{-1}$ after 14 s, then another less subtle contraction and expansion, and only after 20 s do we see the expected gradual decrease in transverse velocity as it gets converted to parallel velocity and begins to form the expected conic. The following figure shows the further development of the conic distribution function

for this situation.

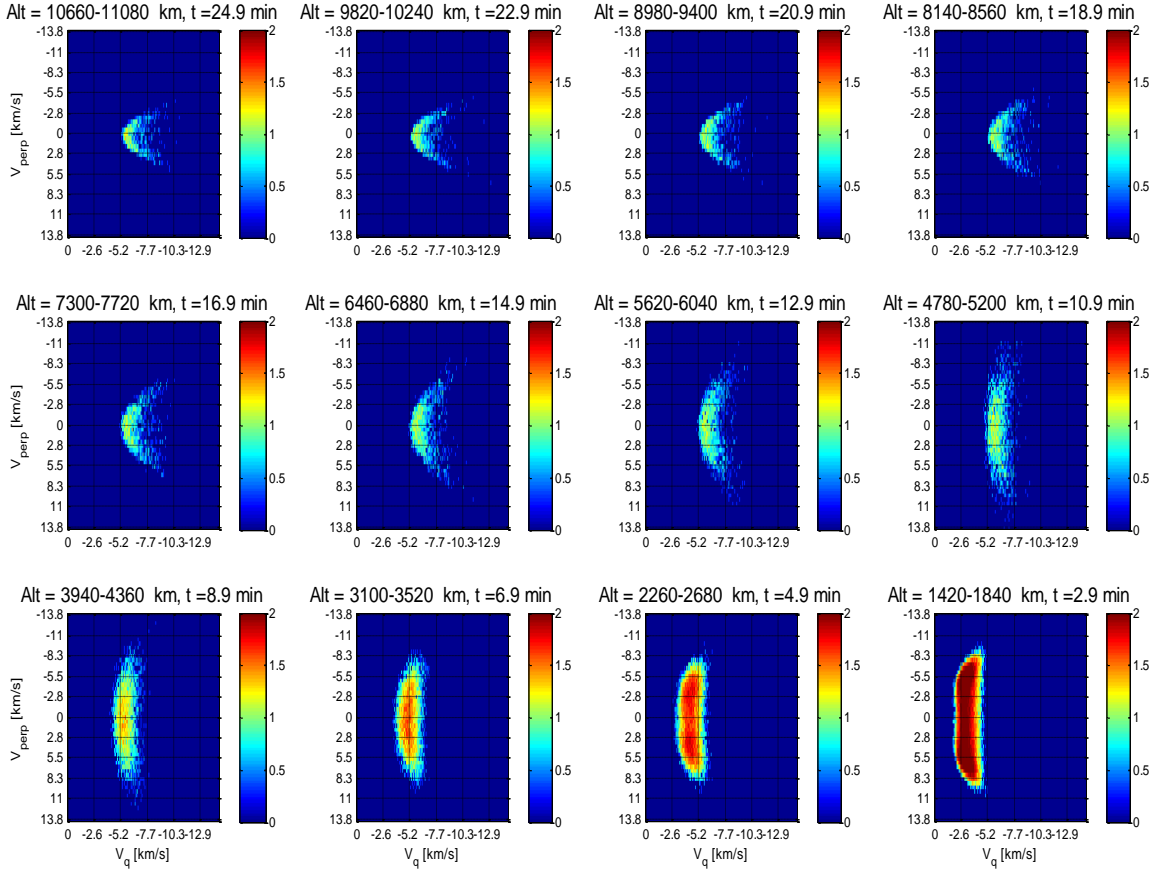


Figure 5.2: Case 1. Full conic development for the partially coherent case. The above 12 snapshots in time increase in time and in altitude from right-to-left, bottom-to-top. The simulation traced about 150,000 particles that are initialized from 1000 to 1750 km and traced for 25 min (there are many less particles in this simulation than in the last run because of the long runtime used in this particular run). The color axis represents the logarithm of the number of particles in each velocity bin. The transverse electric field spectral density reference value $E_0^2 = 2 \times 10^{-5} \text{ V}^2 \text{ m}^{-2} \text{ Hz}^{-1}$.

It is seen in Figure 5.2 that the partially coherent case does eventually result in the expected conic distribution. The velocity-space snapshots increase in altitude as well as time from bottom-to-top, right-to-left in attempt to follow the bulk of the high energy component of the outflow. The simulation traces 150,000 O^+ ions

that for 25 min with equivalent parameters as the simulation shown in Figure 5.1. The expected pitch angle folding is seen here as the conic progresses in time and altitude.

Examining Figure 5.2, the parallel velocity generally increases in altitude, as expected (although it is seen here to eventually remain relatively constant due to the figure's attempt to follow the same ions during and after heating). The figure displays folding that occurs during the conic distribution's conversion from transverse to parallel velocity throughout the conic development; the parallel velocity spans from about -2.5 km s^{-1} to -5 km s^{-1} at the altitude bin from 1420 km to 1840 km after 2.9 min and expands and increases to the range from about -5.2 km s^{-1} to -9 km s^{-1} at the altitude bin from 10,660 km to 11,080 km after 24.9 min, and the transverse velocity spans from about $\pm 9 \text{ km s}^{-1}$ at the altitude bin from 1420 km to 1840 km after 2.9 min and contracts to the range from about $\pm 3 \text{ km s}^{-1}$ at the altitude bin from 10,660 km to 11,080 km after 24.9 min.

Figure 5.3 (Case 2) shows a good qualitative example of what can happen when a gradual, downward potential is applied to the transversely heated conic. The particle initialization region is from 1000 to 1750 km, and the gradual downward potential extends from 3000 km to 6000 km (remember that the heating region is from 1000 km to 10,000 km). The choice for the magnitude of the drop ($E_q = 0.00667 \text{ mV m}^{-1}$ in the downward, positive \hat{q} direction) is explained more fully in the following section when the gradual potential is applied to the incoherent case (the reasoning behind the magnitude choice was to match the initial peak in transverse energy of the incoherent case and does not necessarily apply to this particular case—an equivalent value was used for comparative purposes). Figure 5.3 shows the altitude range from just below the heating region to just above the potential drop region. The layout of Figure 5.3 consists of consecutive altitude slices which increase from the bottom of the simulation region from right-to-left, bottom-to-top. This is the state of the distribution after the 18 min of tracing that was performed upon more than 250,000 O^+ ions with a spectral density value of $E_0^2 = 2 \times 10^{-5} \text{ V}^2 \text{ m}^{-2} \text{ Hz}^{-1}$.

Some interesting characteristics arise from this application of the downward

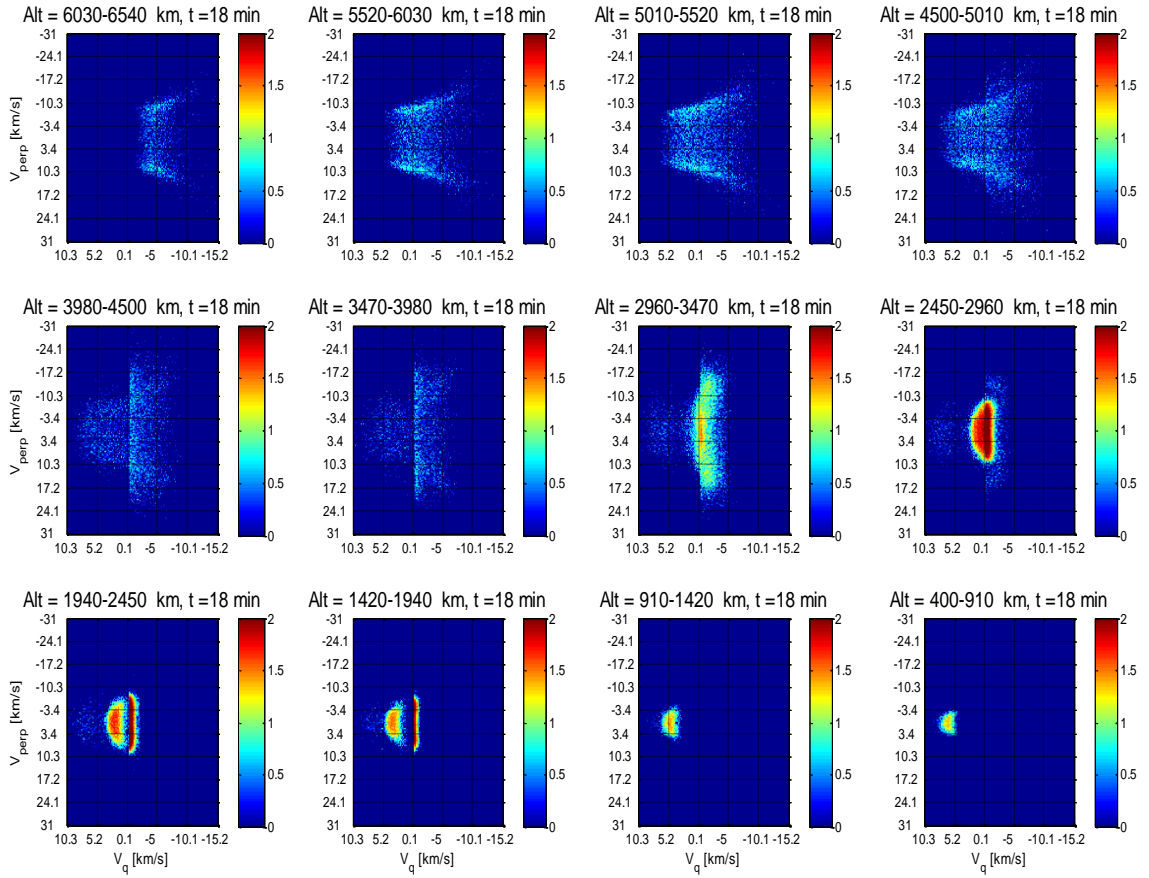


Figure 5.3: Case 2. Counterstreaming distribution functions resulting from a downward, parallel potential drop of magnitude $0.00667 \text{ mV m}^{-1}$ from 3000 km to 6000 km combined with partially coherent transverse energization (electric field wave phase $\epsilon = \pm \pi/2$ rad) for a simulation of over 250,000 particles that are initialized from 1000 to 1750 km and traced for 18 min. The color axis represents the logarithm of the number of particles in each velocity bin. The transverse electric field spectral density reference value $E_0^2 = 2 \times 10^{-5} \text{ V}^2 \text{ m}^{-2} \text{ Hz}^{-1}$.

potential in Figure 5.3. A comparison of the average outflowing ion energies between the cases with and without the gradual potential drop will be performed in Section 5.2. This figure demonstrates qualitatively some counterstreaming effects that can result from this situation. Up to three different counterstreams can be seen clearly at least from the altitudes of 1420 km to 4500 km. At the lower end of this altitude range, the high energy, upwardly directed outflowing stream spans the

largest transverse velocity range, whereas the counterstream which is relatively slowly moving upward obtains a similar transverse velocity span at the higher end of this altitude range—this range reaches a maximum that is greater than $\pm 20 \text{ km s}^{-1}$, a value much higher than the maximum seen in the previous case without the downward potential. This suggests the presence of a re-heating process due to the increased residence time in the heating region caused by the potential. The third counterstream seen in this range is the high energy, downwardly directed stream. Notice that this stream reaches a maximum downward velocity nearing 10 km s^{-1} , which is similar to the velocity of high energy upward stream seen just above the potential drop region in the top-left snapshot.

For the case of full coherency, in which the range of the phase of the energizing LHCP wave is $\epsilon = 0 \text{ rad}$, the results are qualitatively very similar to the partially coherent case presented above. No figure is displayed here for brevity due to the similarity of the case with the partially coherent case. One case study showed that the energization rate for the fully coherent case is slightly larger than that for the partially coherent case (the total, average rate of energy increase for the partially coherent case was 89% of that of the fully coherent case over 14 min of heating). Similar substructures are apparent. Interestingly, in this case of full coherency, these initial substructures do not have multiple contractions in the perpendicular direction before settling to a conic as is seen in the during the initial temporal evolution of the partially coherent case shown in Figure 5.1—it has one such expansion and contraction in the transverse direction of velocity space.

5.2 Ion Conics Resulting from Incoherent Transverse Energization

The six simulations of this section are presented to demonstrate the model's capability to produce the expected conic distribution function which results from this transverse heating process with the full range of phase incoherency of the energizing LHCP wave $\epsilon = \pm \pi \text{ rad}$. In particular, the effects of two different spectral

density magnitudes are examined in the first two simulations for the initialization region from 1000 km to 8000 km. The third and fourth simulations mimic the first and second but use the shorter initialization region from 1000 km to 1750 km. The fifth simulation shows the effects of a gradual, downward parallel potential, and the sixth shows the effects of a short-duration, upwardly directed potential pulse.

The first case of the section which corresponds to Figure 5.4, Case 3, shows the classic ion conic produced by transverse ion heating. Figure 5.4 shows the distribution functions after 25 min of tracing 300,000 O^+ ions. The snapshots increase in altitude from right-to-left, bottom-to-top. The initialization region is now from 1000 to 8000 km, the spectral density reference value is $E_0^2 = 2 \times 10^{-4} \text{ V}^2 \text{ m}^{-2} \text{ Hz}^{-1}$, and the phase of the energizing wave field is fully incoherent. This magnitude is three magnitudes larger than the value used by Zeng et al. [2006] because it demonstrates a better qualitative result that can be produced during a relatively short model run. Eventually, the computer model will be run off of more computing power and for longer amounts of time. It will then produce better, quantitative statistics as well as a higher degree of detail in its distribution functions by using at least many tens of millions of particles. More future plans are outlined in Chapter 6.

A typical particle of the simulation in Figure 5.4 was heated for about 8 min (they exit the lower geographic latitude limit). The expected velocity-space conic with two upwardly flowing lobes extended in the perpendicular direction is shown here at different altitudes. Note that the average upward parallel velocity increases with altitude.

The next Monte Carlo simulation, Case 4, is displayed in Figure 5.5 for comparative purposes and to present the output which results from a more realistic BBELF wave magnitude; it is the same run as is presented in Figure 5.4, except that the spectral density reference value is $E_0^2 = 3 \times 10^{-5} \text{ V}^2 \text{ m}^{-2} \text{ Hz}^{-1}$ (a magnitude smaller). This magnitude is a factor of 100 larger than the value of Zeng et al. [2006]. Good qualitative results still developed with this relatively short model run. An even more realistic (smaller) spectral density would eventually show appreciable energization as well, with longer runtimes. The results of this simulation

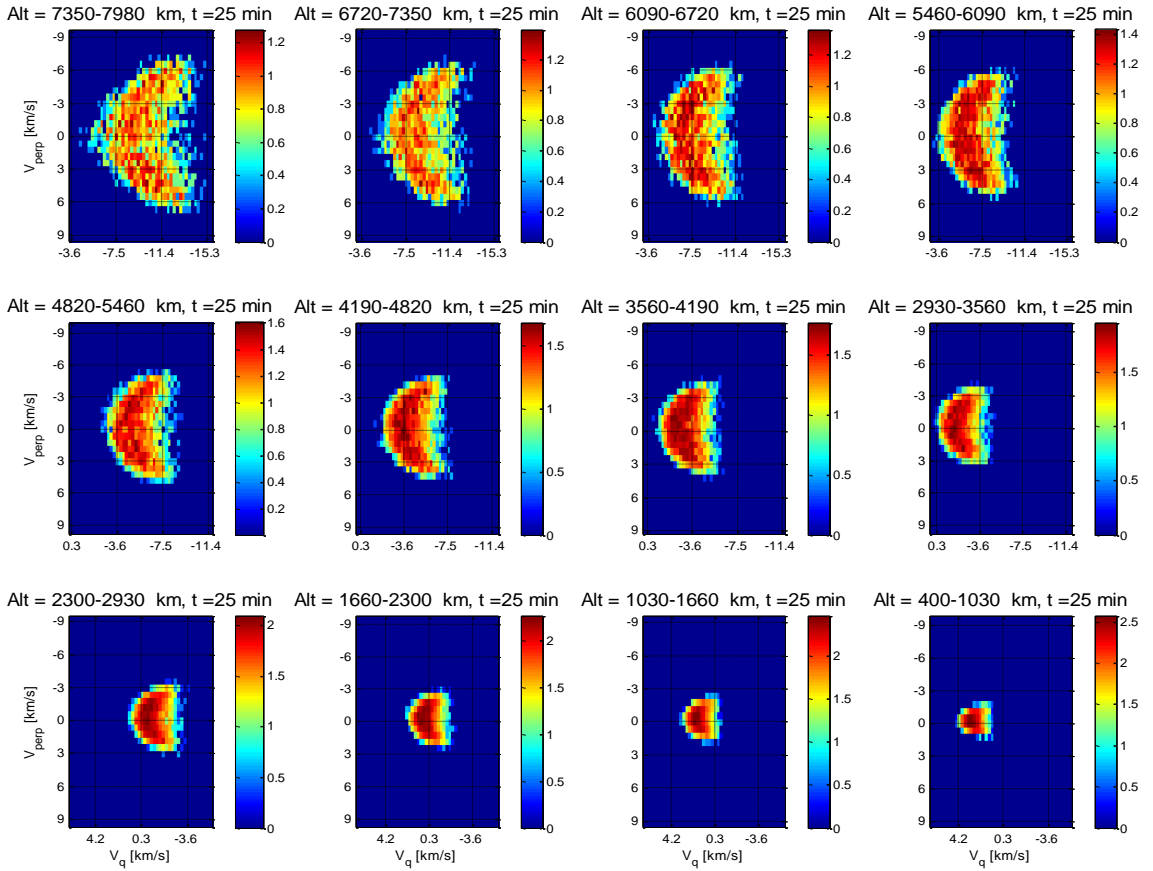


Figure 5.4: Case 3. Incoherent transverse energization of about 300,000 particles initialized from 1000 to 8000 km after 25 min. The color axis represents the logarithm of the number of particles in each velocity bin. The altitude slices are increasing from right-to-left, bottom-to-top. The spectral density reference value $E_0^2 = 2 \times 10^{-4} \text{ V}^2 \text{ m}^{-2} \text{ Hz}^{-1}$.

are considered to be the most closely quantitative in comparison to any other result of the study [Singh and Chan, 1993, Kintner et al., 1996, Norqvist et al., 1998, Wu et al., 1999, Hamrin et al., 2002, Zeng et al., 2006].

A typical particle of this simulation (Figure 5.5, Case 4) was heated for about 10 min (this is a longer heating time than in the last simulation because it takes these particles a longer time to exit the heating region due to the smaller relative transverse electric field magnitude). The expected velocity-space conic is also seen here. The area in velocity space is seen to be smaller here than that of the previous case

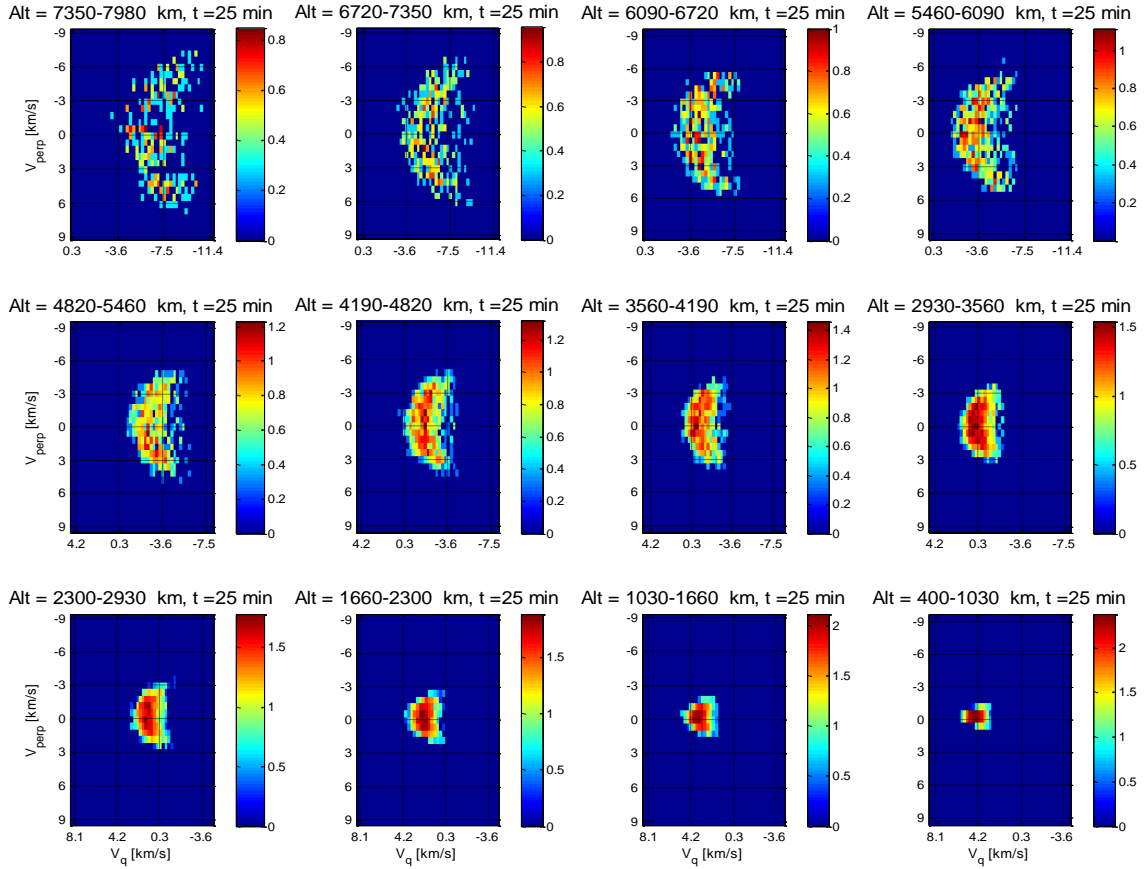


Figure 5.5: Case 4. Incoherent transverse energization of about 300,000 particles initialized from 1000 to 8000 km after 25 min. The color axis represents the logarithm of the number of particles in each velocity bin. The spectral density reference value $E_0^2 = 3 \times 10^{-5} \text{ V}^2 \text{ m}^{-2} \text{ Hz}^{-1}$ (a magnitude smaller than the previous case).

in Figure 5.4, which had a larger electric field magnitude. The average velocity in this case is 2 to 4 km s^{-1} slower in the upward direction (negative \hat{q} direction) over the displayed range from less than 1000 km to nearly 8000 km altitude, with a larger difference at higher altitudes. The maximum upward velocity at 7500 km altitude is about 11 km s^{-1} in the upward direction (corresponding to an energy of 10.0 eV), as compared to the previous simulation's maximum of about 15 km s^{-1} (corresponding to an energy of 18.7 eV) at the same altitude. Note here that there is a much higher energy constituent in all of these simulations at higher altitudes

than is presented—some with velocities greater than 40 km s^{-1} , or 130 eV —but the statistics are too sparse to form any kind of qualitative distribution function here (note also that even if only 1000 macroparticles in this simulation get energized to the energies seen in the highest energy constituent, they will not produce good form in the distribution function since they are often spread among multiple altitude bins, but they still make up 3% of the outflow). In addition to not producing good statistics, many of the high energy particles left the simulation region at the upper altitude boundary. Also, at 7500 km there is a maximum of about $\pm 7 \text{ km s}^{-1}$ in the transverse directions, which is only about 0.5 km s^{-1} smaller than the transverse velocity span at 7500 km altitude for the previous simulation.

Presented below is a display of the average particle energy components at each time-step for this case. The energy values from the first case above, which uses the larger electric field, were not shown in a figure because they follow the same trend as seen in the energy values shown in Figure 5.6, but the conversion from transverse to parallel energy happens slightly faster, similar to but not as dramatic as the effects of coherency. The final average energy per particle was a factor of approximately 1.8 larger when using larger spectral density value. It should be noted here that coherency has proven to cause a much faster energy transition than is evident in the comparison of the two incoherent case with electric field values that are different by a magnitude. It can also be noted here that the shorter initialization region (shown in the following two simulations) produces these same trends, but there are two differences. The final energy magnitudes are roughly a magnitude smaller, and the average ion's transition from transverse to parallel energy takes longer than is seen with the taller initialization region.

The average particle energy per time-step was calculated via the application of the following relationship at each time-step for the transverse and parallel energy components.

$$\langle W \rangle = \frac{1}{2} m_o \frac{\Sigma v^2}{N}$$

Here, W and v denote either the transverse or parallel energy and velocity, and the average total energy per particle was found by summing the transverse and parallel energies. N is the total number of particles in the simulation at each time-step. Some trends seen on the energy plots of this chapter can be explained upon realization that many of the highest and lowest energy particles leave the simulation region. The average initial energy per particle is 0.124 eV for the initial conditions of every simulation in this study.

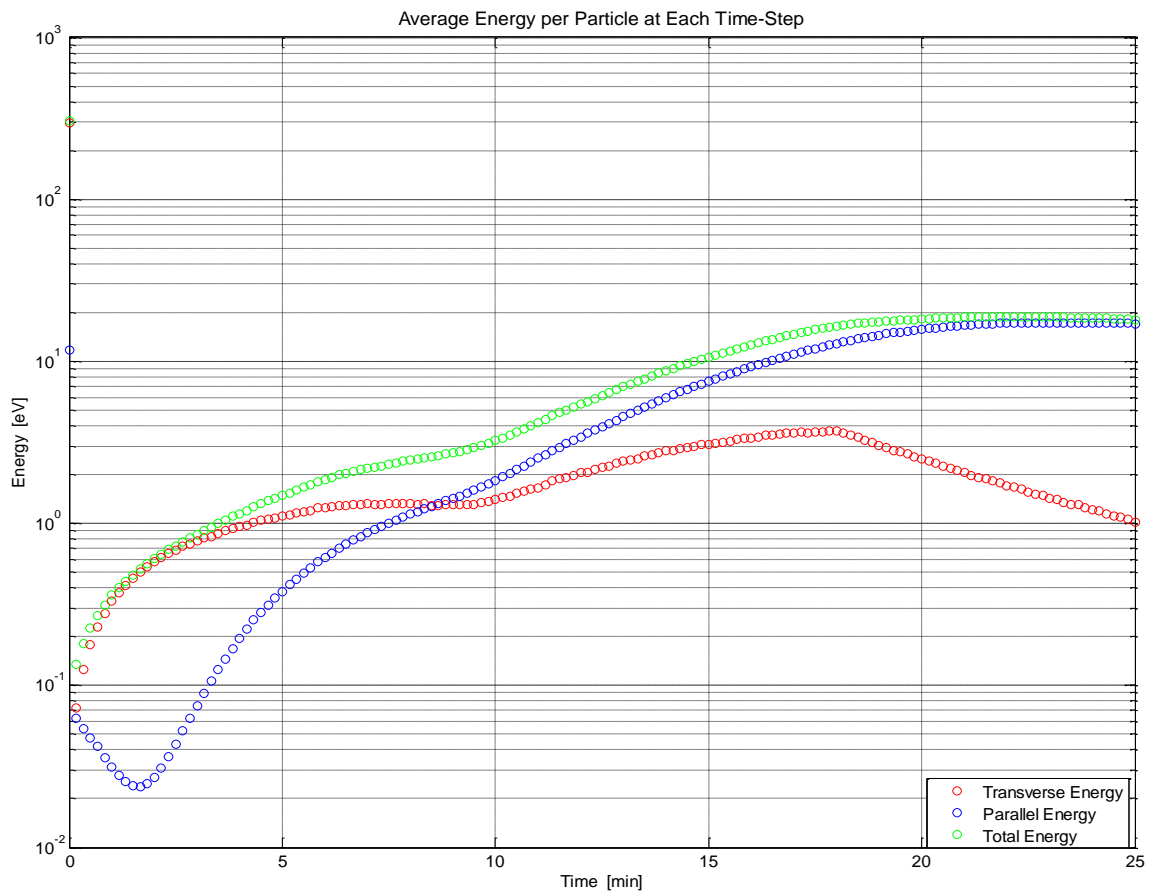


Figure 5.6: Case 4. Average particle energy at each time-step for the simulation corresponding to that shown in Figure 5.5. The energizing electric field is turned off after 18 min.

For this incoherently energized case (Figure 5.5) with average particle energies

per time-step that are shown in Figure 5.6, it is seen that after an initial absolute maximum in the average ion's transverse energy of about 300 eV, there is a decrease followed by an increase in the transverse energy, reaching another local maximum of 1.2 eV after tracing for 7 min, and a final peak of 3.7 eV after 18 min. Analyses reveal that the first damping of transverse energy is due to incoherency (it is not seen in with any degree of coherency). The second peak is only due to insufficiently energized particles leaving the lower altitude boundary, and the final peak is due to the electric fields all being turned off after 18 min. As the transverse energy gets converted to parallel energy, the parallel energy nears an absolute maximum of about 17 eV after 22 min of tracing. This peak occurs after the average ion's remaining transverse energy is converted to parallel energy after the electric field turn-off, which takes around 4 min, and the linear trend seen thereafter suggests that the conversion roughly follows a power law trend with time. The total energy remains constant after the electric field turn-off, as expected. The final, total average energy per particle is effectively all in the parallel direction at a value of 18 eV.

The following two simulations, Case 5 and Case 6, serve to quickly document the distribution functions which result from the same two situations as discussed above, but with an initialization region of a much smaller altitudinal extent. Here, the region is from 1000 km to 1750 km instead of from 1000 km to 8000 km, as in the previous cases.

The particles of the simulation shown in Figure 5.7 which did not exit the bottom boundary of the heating region (1000 km) remained in the heating region for the duration of the simulation. Because most of the particles in this shorter initialization region start lower than the initial altitudes of the previous simulations, the outflowing mass here did not have as large of a higher-energy constituent. The particles are on average more bound by gravity and a weaker transversely energizing electric field at the lower altitude.

Most of the particles of the next simulation that is shown in Figure 5.8 left the bottom boundary of the heating region (1000 km) in less than 12 min. Although also seen in previous simulations, it is most easily seen here that those particles

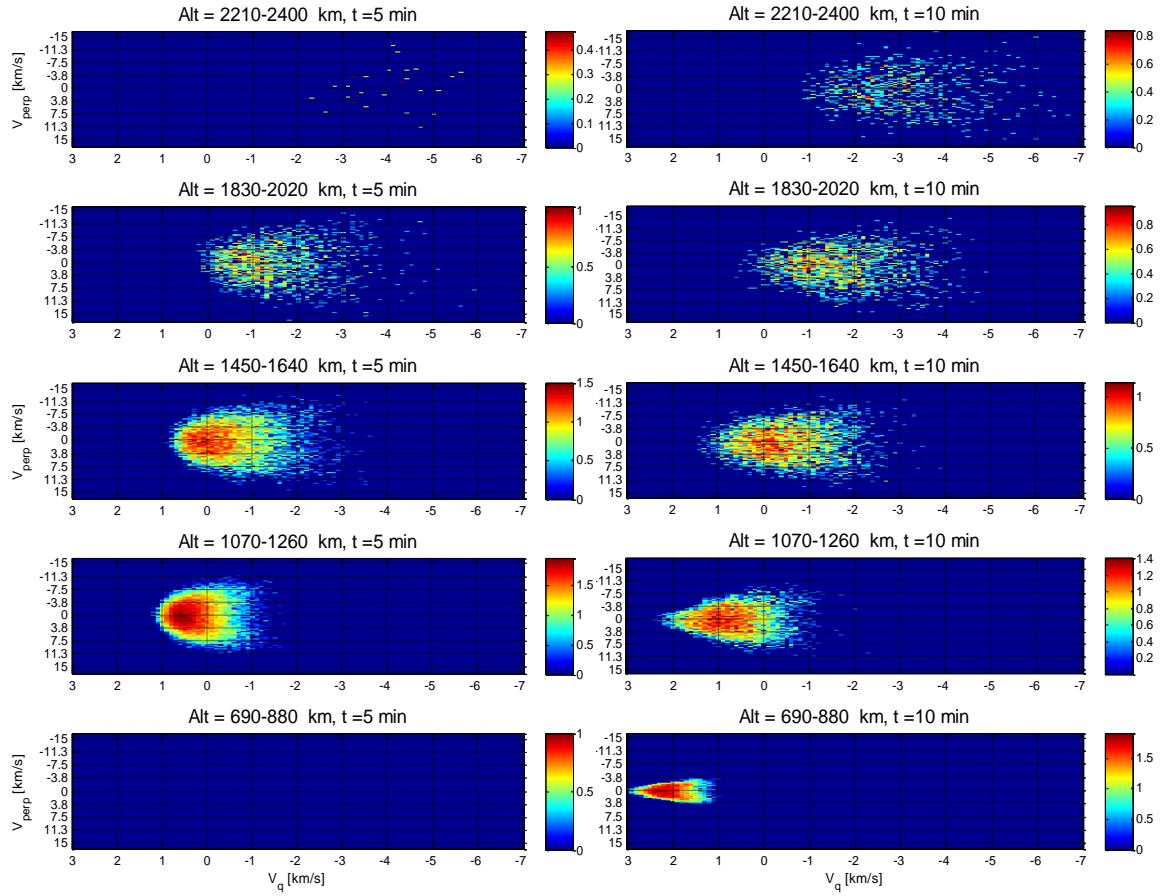


Figure 5.7: Case 5. Conic development and bulk motion which result from fully incoherent energization of about 100,000 particles that are now initialized from 1000 km to 1750 km with $E_0^2 = 2 \times 10^{-4} \text{ V}^2 \text{ m}^{-2} \text{ Hz}^{-1}$ at $t = 5$ min (left) and $t = 15$ min (right). The color axis represents the logarithm of the number of particles in each velocity bin.

which are not sufficiently transversely heated to move upwards due to the mirror force become an appreciably energized beam of ion precipitation, moving downwards with a maximum velocity of about 3 km s^{-1} after 10 min. This corresponds to a downward, field-aligned energy of 0.75 eV.

The remaining two simulations to be presented in this thesis explore the effects of parallel potentials upon these incoherently energized distribution functions. Firstly, the effects of a constant, downwardly oriented potential drop upon

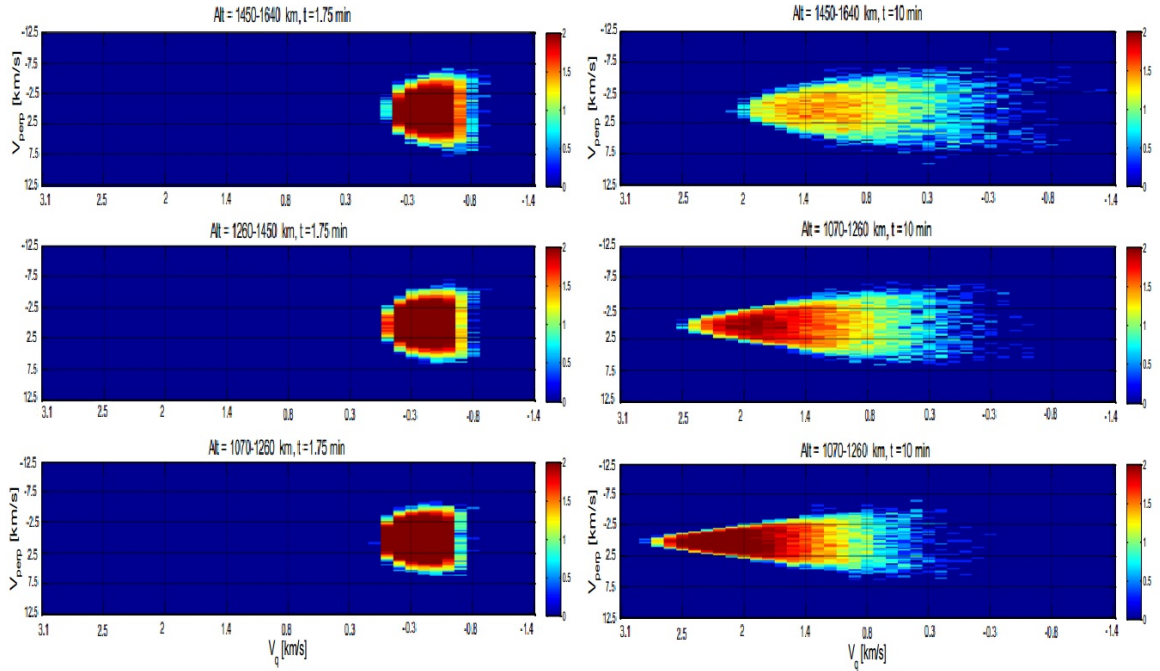


Figure 5.8: Case 6. Lower energy conic development and bulk motion which result from fully incoherent energization of about 250,000 particles initialized from 1000 km to 1750 km with $E_0^2 = 5 \times 10^{-5} \text{ V}^2 \text{ m}^{-2} \text{ Hz}^{-1}$ (a magnitude smaller than the previous case) at $t = 1.75 \text{ min}$ (left) and $t = 10 \text{ min}$ (right). The color axis represents the logarithm of the number of particles in each velocity bin. This figure serves to show what happens to the lower energy tail of the distribution function at lower altitudes.

the incoherently energized distribution functions of the group of particles initialized from 1000 km to 8000 km are examined in Case 7. In this simulation shown below in Figure 5.9, a gradual drop of magnitude $0.00667 \text{ mV m}^{-1}$ is applied over the altitude range of 3000 to 6000 km, which corresponds to a 20 V drop. This value was chosen to match the energy gained in the typical O^+ transverse energy peak, which was at the time of the simulation believed to be on the order of 20 eV. A larger value such as that displayed in Figure 5.6 would have been a better choice; this was a personal error committed due to hurried circumstances). Therefore, the environment should produce flux tubes with sufficiently energized ions

outflowing due to their ability to overcome the potential drop, and with insufficiently energized ions precipitating downward simultaneously (as was qualitatively demonstrated in Figure 5.3). This consequence is demonstrated below.

As seen in Figure 5.9, four snapshots in time for four different altitude slices are presented. A typical particle of the simulation shown in Figure 5.9 was heated for about 10 min (this is a heating time slightly smaller than in the case with the same transverse electric field and initialization region but no potential drop—the simulation of Figure 5.5). The initialization region is once again 1000 km to 8000 km altitude, and $E_0^2 = 3 \times 10^{-5} \text{ V}^2 \text{ m}^{-2} \text{ Hz}^{-1}$. Apparent in these snapshots are a low-energy counterstream near the bottom of the region, a higher-energy, crescent-shaped counterstream, and the classic transversely heated conic that has both up-flowing and downflowing components at certain altitudes.

The four altitude slices shown in the snapshots of this figure (5.9) depict from top to bottom: the region just above the parallel drop region but still within the transverse heating region (6090 km to 6720 km), a region within the parallel drop region and within the transverse heating region (4190 km to 4820 km), the region just below the parallel drop region and still within the transverse heating region (2300 km to 2930 km), and the region just below the heating region with 30 m of the 630 km region remaining in the heating region (400 km to 1030 km). The first snapshot at 0.7 min displays the classic conic in the top altitude slice, and, interestingly, the second region from the top shows a transversely heated downflow. This constituent goes on in the following snapshots to show a mirroring of some of its particles up to the top altitude slice where a few high energy particles are seen at 5 min and beyond, and most of its particles eventually contribute to the higher energy downflow that is visible after 12.5 min in the bottom altitude slice. The third altitude slice from the top at 0.7 min gets heated as expected and is seen to eventually support an appreciable outflow, viewable in the second altitude slice from the top after 25 min.

The average particle energies corresponding to the simulation in Figure 5.9 are shown in Figure 5.10. For this incoherent case which is the same as that shown in

Figure 5.5, except with a parallel potential drop, it is seen that the average particle reaches an initial absolute maximum in transverse energy of about 300 eV—the same initial peak energy as that shown in Figure 5.6. Also, there is then a similar decrease followed by an increase in the transverse energy. The transverse energy of the average particle then reaches another local maximum around 8 min of tracing with a value of only 0.8 eV—only two-thirds the transverse energy peak that is seen with no downward potential. The last transverse energy peak is 1.0 eV, which is less than two-thirds of the corresponding peak in Figure 5.5. As the transverse energy gets converted to parallel energy, the parallel energy reaches an absolute maximum of about 3.5 eV after 16 min of tracing. This is almost a factor of 5 less than the amount of parallel energy gained by the average particle in Figure 5.6. A comparison shows that maximum velocities in this case are less than half of the equivalent case of the case without the parallel drop. These relative parameters suggest that the parallel drop causes significant damping upon the outflow’s energization process, even though the voltage drop had an effective energization of 20 eV in the positive \hat{q} direction which is only 6.7% of the initial transverse energy peak. The cause of such significant damping is a potential case for further research. It is possible that, with longer runtimes, the resonance time may be increased enough to cause higher-energy outflows.

The following simulation, Case 8, that is plotted in Figure 5.11 documents a possible effect of an upwardly directed, parallel potential pulse for this incoherent case. However, the figure mainly exhibits the lower-energy conic dynamics because the initialization region is here from 1000 km to 1750 km, and the potential pulse proved to be insufficient in causing appreciable high-energy constituents of the distribution with this small electric field ($E_0^2 = 5 \times 10^{-5} \text{ V}^2 \text{ m}^{-2} \text{ Hz}^{-1}$).

The upward, parallel potential pulse was meant to be applied during the first peak in transverse energy. However, it was seen during the study that the application of the pulse at the second transverse energy peak may be much more effective in increasing the outflows. Further investigation needs to be performed in order to officially confirm and provide more quantitative details of this claim. This pulse does increase the energy of the outflow. As compared to the equivalent simulation

which only differs by the absence of the parallel pulse (Figure 5.8), both the magnitude and the rate of energization are appreciably increased. A typical particle of this simulation shown in Figure 5.11 was heated for over 11 min, and 83% exited the bottom of the simulation region (400 km) by the end of the simulation. This Figure 5.11 serves at least a dual purpose. Firstly, between the first two time slices, a visible jump in parallel bulk velocity of around 0.4 km s^{-1} shows the immediate effect of the upward pulse. Secondly, the last three figures display the evolution of the low energy, transversely heated distribution as it transitions to a downwardly directed stream.

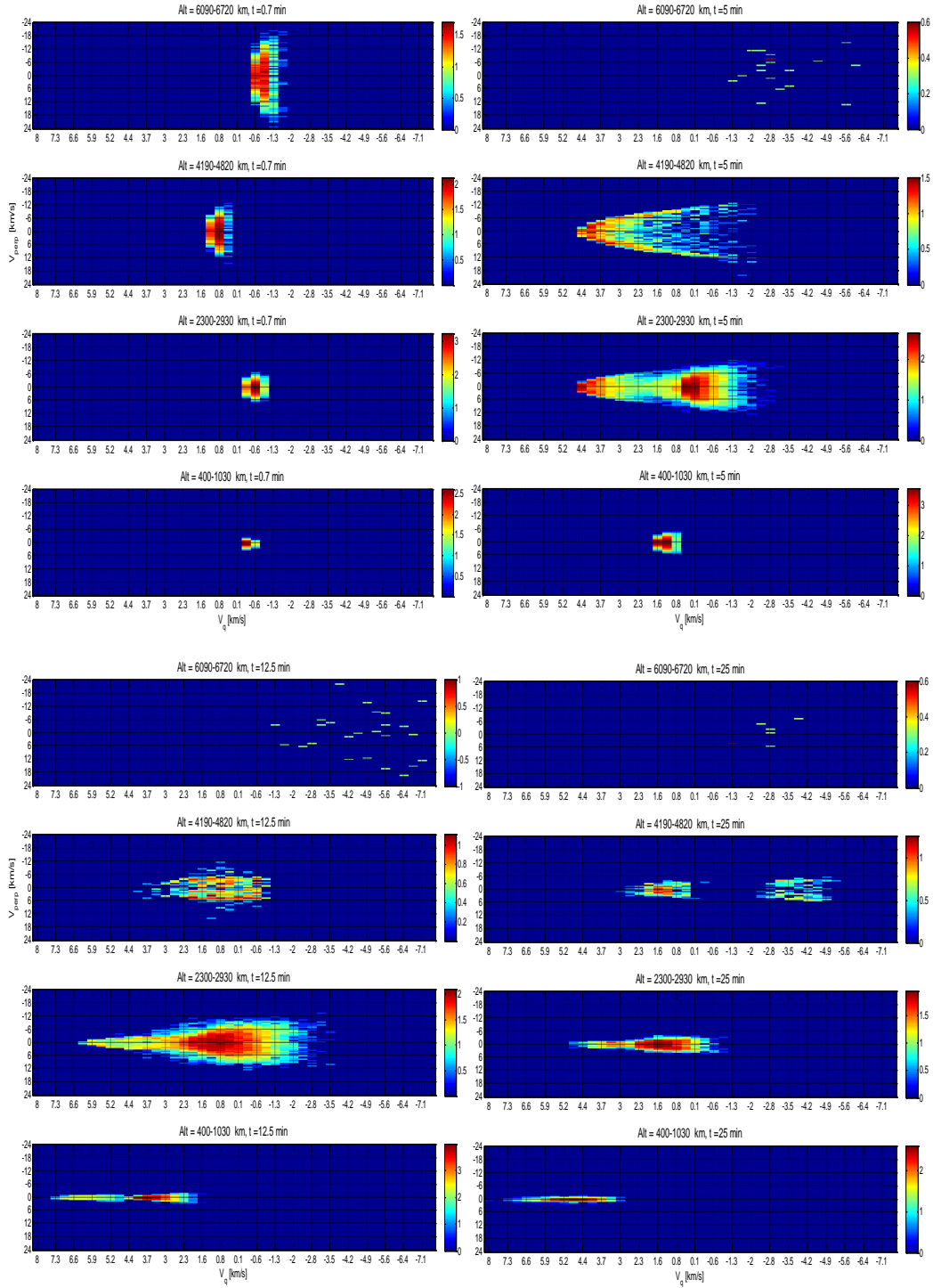


Figure 5.9: Case 7. The above four snapshots in time show the development of distribution functions due to incoherent transverse energization and a downward, gradual parallel potential drop of 0.0067 mV m^{-1} applied over the range of 3000 to 6000 km for a simulation of over 300,000 particles that are initialized from 1000 to 8000 km and traced for 25 min. The color axis represents the logarithm of the number of particles in each velocity bin. The spectral density reference value $E_0^2 = 3 \times 10^{-5} \text{ V}^2 \text{ m}^{-2} \text{ Hz}^{-1}$.

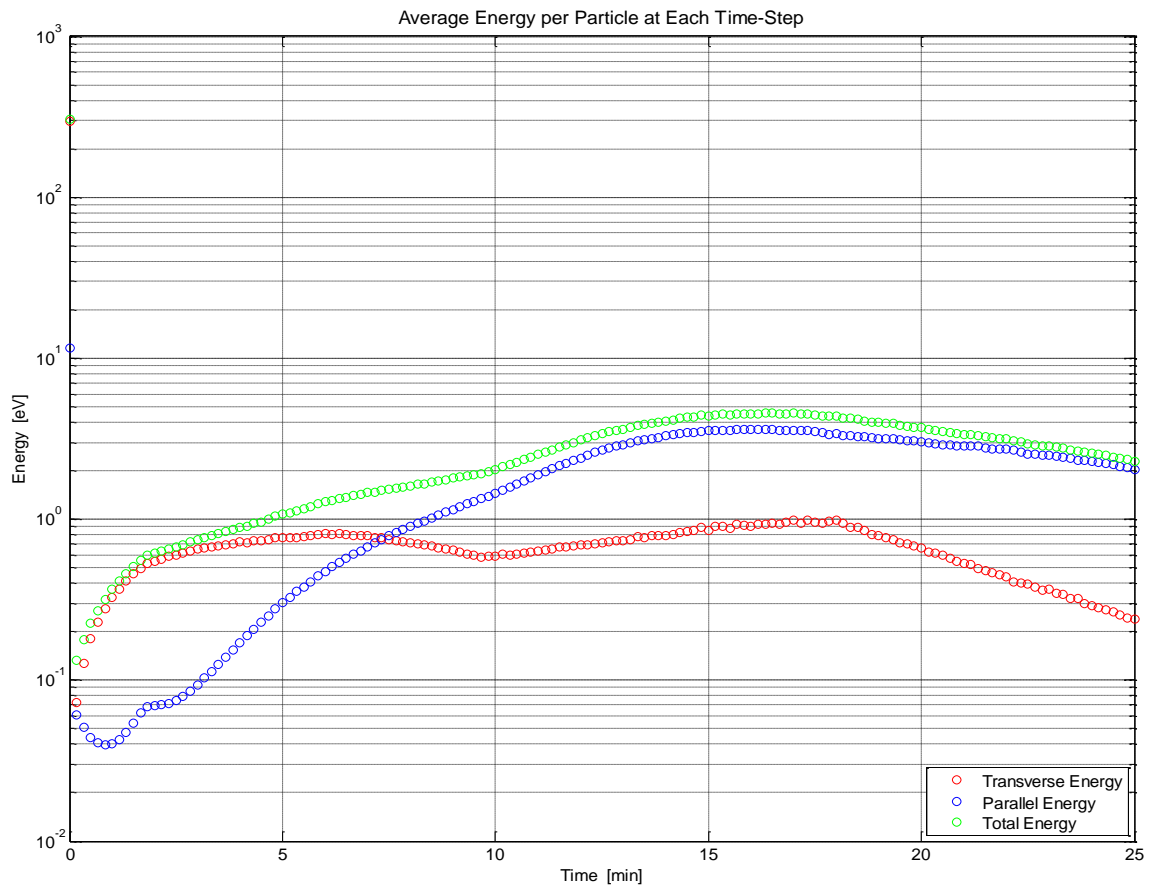


Figure 5.10: Case 7. Average particle energy at each time-step for the simulation corresponding to that shown in Figure 5.9. The energizing electric field is turned off after 18 min.

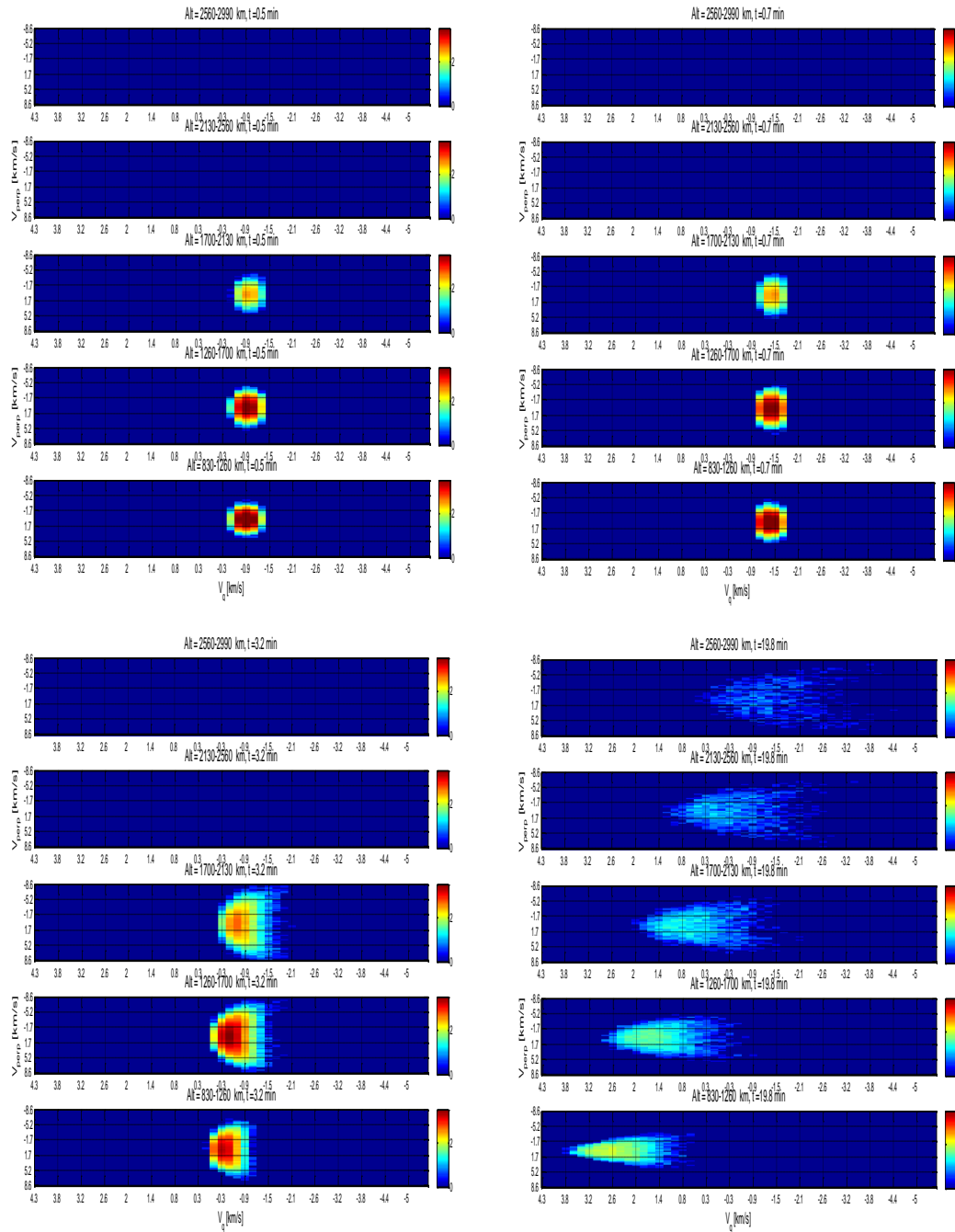


Figure 5.11: Case 8. The above five snapshots in time show the development of distribution functions due to incoherent transverse energization and an upward parallel potential pulse of 10 mV m^{-1} applied for 10 ms [Singh and Chan, 1993] for a simulation of nearly 200,000 particles that are initialized from 1000 to 1750 km and traced for 20 min. The color axis represents the logarithm of the number of particles in each velocity bin. The transverse electric field spectral density reference value $E_0^2 = 5 \times 10^{-5} \text{ V}^2 \text{ m}^{-2} \text{ Hz}^{-1}$.

Chapter 6

Conclusions and Future Work

6.1 Conclusions

A summary of the conclusions to take away from this study are presented below. Firstly, some general conclusions can be drawn from the model development process. An optimal fraction of the gyro-period for the time-step is $1/20$. The time-step is still numerically stable at least to $1/5$ of a gyro-period (and possibly to even larger fractions), and this value can possibly be implemented if efficiency is exceedingly more important than quantitative accuracy in the simulation. A fraction of $1/100$ of a gyro-period is optimal for close accuracy, but not ideal for efficiency. Regarding the analysis and comparison of the guiding center particle tracing method in Section 2.4.2, it was found that the approximation is not as sound of a calculation as the method of this study for mapping ion trajectories to the magnetosphere or for dynamic magnetic fields with short scale, significant gradients on the order of a few km and less; this is due respectively to the inaccuracies brought upon by changes in magnetic field over the distance of a Larmor radius when tracing far into the magnetosphere, and because of the large time-step used when tracing high velocity outflows that can have significant variance in magnetic field between time-steps. Also, the guiding center method requires a perfectly gyrotropic initial distribution of ions for its heating method to be valid; this requirement is absent from the model presented in this study.

6.1.1 Trajectory Mapping

The most definite conclusion to be drawn from the Chapter 4 results which map transversely heated O^+ outflows to a realistic magnetosphere is that an effective tool that can be used for obtaining ion escape probabilities and regional destination probabilities of this non-thermal acceleration process has been created. Also, the study suggested that approximately 78.5% of ions transversely heated in a narrow region that is susceptible to energetic outflows during a powerful geomagnetic storm stay below $1 R_E$ in a configuration along a field line. The remaining ions were mostly energized sufficiently enough to quickly escape the magnetosphere on open magnetic field lines due to the dynamic configuration of the magnetosphere that was caused by the simultaneously occurring dramatic reconnection and plasmoid ejection during the time of the BATSRUS model output.

6.1.2 Distribution Functions

Some generalized, qualitative conclusions can be asserted via reference to the results presented in the Monte Carlo simulations of Chapter 5. For instance, the maximum Larmor radius in model's current environment can reach well over 10 km throughout the heating process, and therefore finite radius effects of the BBELF field are significant. This happens when the energization rate is gradual enough to keep ions in the heating region for a long residence time, yet large enough to add energy with an incoherent wave field. Another conclusion is that the initialization region's altitudinal extent has a large influence on the net energization of the outflows (the ions initialized in the shorter region of this study experienced about one magnitude less energization than the higher region's ions). This is apparently due to the smaller transversely energizing wave magnitude and the stronger gravity at lower altitudes (significant restraint of outflows occurs at lower altitudes even in the absence of collisions). A common find of this study was a significantly energized ion precipitation stream for transversely energized particles that did not mirror upwards; this was an unexpected result, and further investigation should be performed to fully explain this occurrence.

Any degree of coherency causes the development of defined substructure in the velocity distribution functions of the particle group. These structures are a result of the situation in which certain ions are in phase with others in a symmetric fashion throughout the initial transverse energization due to a restriction of the energizing wave's phase and therefore a restriction of the possible ion energies. Coherent and partially coherent acceleration both cause the expected ion conic. This part of the study proved the model's capability to produce highly detailed non-Maxwellian distribution functions (as well as detailed counterstreams that are known to occur with gradual, field-aligned potential drops). In a case study, partial coherency was seen to be 89% as efficient at energizing than full coherency after 14 min of heating. Coherency causes the average particle energy to not be initially dampened, as happens with the incoherent case, but it does not ultimately cause a significantly larger total magnitude of energization (partial coherency produces an average particle energy a factor of 2.3 larger than the equivalent incoherent case after 15 min of tracing). These conclusions, as well as the initialization region's effects upon energization, support the conjecture that the total energization is mostly a function of the spatial extent of the heating region—or, at the least, its altitudinal extent (a larger spatial extent corresponds to a longer residence time in the heating region).

A comparison of the first two incoherently energized simulations that are shown in Figures 5.4 and 5.5 suggests that, after 25 min of tracing, the resulting energies of the outflows are similar—the larger spectral density reference value in the first case served to foster a faster conversion from transverse to parallel energy, but did not serve to increase the total magnitude of energization significantly in the presented situation (one magnitude larger spectral density value resulted in less than twice the final, total average energy per particle). In the case considered to be the most closely quantitative (Figure 5.5), the average heated particle energy was 18 eV after 25 min, with a maximum high energy component of ions with easily over 130 eV (field-aligned energies). These values are consistent with the following referenced expected ion outflows from observation and theory [Singh and Chan, 1993, Kintner et al., 1996, Norqvist et al., 1998, Wu et al., 1999, Hamrin et al., 2002, Zeng et al., 2006].

A downwardly oriented parallel potential drop that equates to 6.7% of the average initial transverse energy peak of a heated ion group will cause energetic counterstreaming distribution functions and will ultimately cause a damping of the average particle's final total energy that is almost a factor of 5 less energy than the identical simulation that lacks the potential drop after 25 min of tracing (at least, this can be claimed for the situations described in Figures 5.5 and 5.9). However, the parallel potential drop case may ultimately cause an increase in the total energization by increasing the residence time in the heating region, which can be confirmed or disproved with a similar comparative study which uses a longer runtime.

6.2 Future Work

This thesis has presented the initial validation of a new model. The remaining paragraphs of this document will list some necessary, general modifications, possible improvements to computational efficiency, and some capabilities and goals of the current two versions of the model.

Some appropriate, general modifications include the following. Self-consistency should be imposed upon the model via, for example, methods of Jasperse [1998] for field-aligned electric field self-consistency of the ion outflows, or of Wu et al. [1999], by designating the assumption of quasineutrality to generate currents resulting from the energized and displaced, positively charged O^+ ions. Also, collision frequency and magnitude change with altitude need to be improved, and the application of a Gaussian number generator to the collisions is necessary. Just as well, the uniform, random number generator used in the current model for incoherency, initial conditions, and collisions is generated via obtaining a seed value from the current clock time, and this can be improved to be moreMagnetic latitude uniform of a number distribution. A Gaussian distribution of initial velocities is a particularly necessary model modification. Magnetic latitude and magnetic local time are also urgent modifications. Additionally, a guiding center model should be implemented by this model in the future. This endeavor would require

the generation of a gyrotropically distributed initial assortment of ions [Chang et al., 1986], as well as a coordinate change to the use of the distance along the local magnetic field line instead of altitude (for ease of use and for comparison to other guiding center models). This quantity can be found via the relationship: $\vec{s} = xB_x/B\hat{x} + yB_y/B\hat{y} + zB_z/B\hat{z}$. The guiding center method should then be compared to the current model, and analyses of the relative inaccuracies resulting from large radius effects as well as a large time-step should be implemented. And, finally, the resonance energization by lower hybrid waves can be included.

To improve computational efficiency, integration with the newly attained cluster in ERAU's Physical Sciences Department will vastly improve the statistics produced by both current model versions. Also, model output should be written to binary format as opposed to the current ASCII .txt output file format. A fourth order predictor-corrector integration scheme should be implemented. A better, quantitative investigation of the optimal time-step dt should be performed with a wider and denser range of fractions of a gyro-period for both the comparison of the best numerical solution to the trajectories produced by the final equations of motion in Equations 2.15 and of the solvable analytical solution to the numerical solution of the third case presented in Section 3.1: Model Validation.

Some results which can readily be attained with both versions of the current model include the following. The overall flux of the outflows should be calculated via the extrapolation of the macroparticle density to a realistic ion density. An investigation into the effects of a wide range of varying initial positions and velocities can be performed. Quantitative numerical error analyses should be performed upon the current, manually designed Runge-Kutta fourth order integration scheme, and other, independently developed schemes of the same nature should be compared. Higher order Runge-Kutta integration schemes can be applied and compared. More results using only fully incoherent energization should be obtained in the future. The modeling of proton (H^+) outflows can also be performed. Better comparisons to observations and other models should be made

with a more quantitative investigation of the transverse energization process. Finally, an investigation upon residence time in the heating region should be performed with either model or both models.

Particular to the magnetospheric mapping adaptation of the model, some results that should be obtained follow. This aspect of the model has a multitude of potential applications due to the interface with CCMC: Kameleon; particle traces using output from CTIP, OpenGGCM, MAS, ENLIL, or LFM can be performed in projects to come in order to apply the tracer to other regions of the solar system including the Earth's magnetosphere and ionosphere, other planets, or the heliosphere. A better statistical simulation and analysis of O^+ outflows should be performed in order to quantitatively determine regional probabilities of the outflow destinations in the magnetosphere. The energy of the outflowing ions should be examined via alternate analyses of the current output files or via the output of velocity from the model. In addition, the use of more BATSRUS .cdf output files representing other magnetospheric configurations should take place. Lastly, the role of the presence of O^+ upon magnetic reconnection in the magnetotail can potentially be investigated.

In conclusion to this thesis report, some results that are particular to the main version of the model which produces distribution functions via the Monte Carlo technique are suggested. The distribution functions should be normalized. Better energy analysis should be performed, beginning with the development of a way to properly analyze the outflow's energy while avoiding the effects of particles leaving the simulation region. An analysis of the effects upon the rate and magnitude of energization resulting from the application of the parallel potential pulse during both the second transverse energy maximum and at the parallel energy peak should take place (and the use of other magnitudes of the pulse can be studied). Future applications should also quantitatively investigate the effects of a gradual potential drop upon the energization rate and magnitude of outflows, especially those effects resulting from a longer runtime than performed here. The energetic downflow seen in the low-energy conic should be investigated and explained. Any coherency prevents downflows. A quantitative investigation into the phenomenon

that was apparent in this study which occurs when a smaller energizing electric field causes a longer residence time and a higher consequent magnitude of energization than a larger electric field causes should be performed. A variation of the heating region extent can be performed in conjunction with an examination of the effect of residence time upon distribution functions. These studies should all be performed with the higher initialization region of this study (or one similar in extent and upper boundary). The effects of varying the power law index α of Equation 2.9 can be examined in the future as a parameter to adjust during a quantitative investigation. A combination at the upper and lower boundaries with global ionosphere and magnetosphere models can be performed (e.g., with the models of Dr. Matthew Zettergren of the ERAU Physical Sciences Department). In this way, the source plasma fueling the transverse energization process from lower altitudes can be properly accounted for, and the large-scale magnetospheric effects resulting from this important non-thermal energization process can be accurately replicated.

Bibliography

- D. N. Baker, E. W. Hones Jr., D. T. Young, and J. Birn. The possible role of ionospheric oxygen in the initiation and development of plasma sheet instabilities. *Geophysical Research Letters*, 9:1337, 1982.
- I. A. Barghouthi, A. R. Barakat, and A. M. Persoon. The effects of altitude dependent wave-particle interactions on the polar wind plasma. *Astrophysics and Space Science*, 259:117–140, 1998.
- M. Bouhram, M. Dubouloz, N. Malingre, M. Jasperse, J. R. Pottetelette, R. Senior, C. Delcourt, D. Carlson, C. W. Roth, I. Berthomier, and M. Sauvaud. Ion outflow and associated perpendicular heating in the cusp observed by interball auroral probe and fast auroral snapshot. *Journal of Geophysical Research: Space Physics*, 107(A2):SMP 4–1–SMP 4–13, 2002.
- M. Bouhram, M. Malingre, J. R. Jasperse, and N. Dubouloz. Modeling transverse heating and outflow of ionospheric ions from the dayside cusp/cleft. 1 a parametric study. *Annales Geophysicae*, 21(8):1753–1771, 2003.
- M. Bouhram, B. Klecker, W. Miyake, H. Reme, J. A. Sauvaud, M. Malingre, L. Kistler, and A. Blagau. On the altitude dependence of transversely heated o+ distributions in the cusp/cleft. *Annales Geophysicae*, 22:1787–1798, 2004.
- D. G. Brown, J. L. Horwitz, and G. R. Wilson. Synergistic effects of hot plasma-driven potentials and wave-driven ion heating on auroral ionospheric plasma transport. *Journal of Geophysical Research*, 100(A9):17499–17514, 1995.

- Tom Chang. Ionospheric and magnetospheric processes. *Massachusetts Institute of Technology*, 1991.
- Tom Chang and Bruno Coppi. Lower hybrid acceleration and ion evolution in the supraauroral region. *Geophysical Research Letters*, 8(12):1253–1256, 1981.
- Tom Chang, G. B. Crew, N. Hershkowitz, J. R. Jasperse, J. M. Retterer, and J. D. Winningham. Transverse acceleration of oxygen ions by electromagnetic ion cyclotron resonance with broad band left-hand polarized waves. *Geophysical Research Letters*, 13(7):636–639, 1986.
- C. R. Chappell, S. A. Fields, C. R. Baugher, J. H. Hoffman, W.B. Hanson, W. W. Wright, H. D. Hammack, G. R. Carignan, and A. F. Nagy. The retarding ion mass spectrometer on dynamics explorer-a. *Space Science Instrumentation*, 5:477, 1981.
- G. B. Crew and T. S. Chang. Asymptotic theory of ion conic distributions. *Physics of Fluids (1958-1988)*, 28(8):2382–2394, 1985.
- G. B. Crew, T. Chang, and J. M. Retterer. Ion cyclotron resonance heated conics: Theory and observations. *Journal of Geophysical Research*, 95(A4):3959–3985, 1990.
- Y. Ebihara, M. Yamada, S. Watanabe, and M. Ejiri. Fate of outflowing suprathermal oxygen ions that originate in the polar ionosphere. *Journal of Geophysical Research: Space Physics*, 111(A4), 2006.
- D. A. Gurnett, R. L. Huff, J.D. Menietti, J. D. Winningham, and J. L. Burch. Correlated low frequency electric and magnetic noise along the auroral field lines. *Journal of Geophysical Research*, 89(A10), 1984.
- M. Hamrin, M. Norqvist, P. Hellstrom, M. Andre, and A. I. Eriksson. A statistical study of ion energization at 1700 km in the auroral region. *Annales Geophysicae*, 20:1943–1958, 2002.
- M. M. Huddleston, C. R. Chappell, D. C. Delcourt, T.E. Moore, B. L. Giles, and M. O. Chandler. An examination of the process and magnitude of ionospheric

- plasma supply to the magnetosphere. *Journal of Geophysical Research*, 110(A1), 2005.
- B. Hultqvist, M. Oieroset, G. Paschmann, and R. Treumann. *Magnetospheric Plasma Sources and Losses*. Dordrecht: Springer Netherlands, 1999.
- J. R. Jasperse. Ion heating, electron acceleration and the self-consistent parallel E-field in downward auroral current regions. *Geophysical Research Letters*, 25: 3485–3488, 1998.
- P. M. Kintner. Observations of velocity shear driven plasma turbulence. *Journal of Geophysical Research*, 81(28):5114–5122, 1976.
- Paul M. Kintner, John Bonnell, Roger Arnoldy, Kristina Lynch, Craig Pollock, and Tom Moore. Scifer-transverse ion acceleration and plasma waves. *Geophysical Research Letters*, 23(14):1873–1876, 1996.
- M. Kivelson and C. T. Russel. *Introduction to Space Physics*. Cambridge University Press, 1995.
- David J. Knudsen, James H. Clemmons, and Jan-Erik Wahlund. Correlation between core ion energization, suprathermal electron bursts, and broadband elf plasma waves. *Journal of Geophysical Research: Space Physics*, 103(A3):4171–4186, 1998.
- M. Kosch, J. Y. Ogawa, M. T. Rietveld, S. Nozawa, and R. Fujii. An analysis of pump-induced artificial ionospheric ion upwelling at eiscat. *Journal of Geophysical Research*, 115(A1), 2010.
- E. J. Lund, E. Mobius, C. W. Carlson, R. E. Ergun, L. M. Kistler, B. Klecker, D. M. Klumpar, J. P. McFadden, M. A. Popecki, R. J. Strangeway, and Y. K. Tung. Transverse ion acceleration mechanisms in the aurora at solar minimum: occurrence distributions. *Journal of Atmospheric and Solar-Terrestrial Physics*, 62(6):467 – 475, 2000.

- T. E. Moore and J. L. Horwitz. Stellar ablation of planetary atmospheres. *Reviews of Geophysics*, 45, 2007.
- Patrik Norqvist, Mats Andre, and Magnus Tyrland. A statistical study of ion energization mechanisms in the auroral region. *Journal of Geophysical Research: Space Physics*, 103(A10):23459–23473, 1998.
- Theodore G. Northrop. The guiding center approximation to charged particle motion. *Annals of Physics*, 15:79–101, 1961.
- Theodore G. Northrop. Adiabatic charged-particle motion. *Reviews of Physics*, 1(3): 283–304, 1963.
- Theodore G. Northrop. Adiabatic theory of charged particle motion, considering first-order effects in radius of gyration and alfvén theory. *D. Reidel Publishing Company*, pages 26–44, 1966.
- John M. Retterer, Tom Chang, and J. R. Jasperse. Transversely accelerated ions in the topside ionosphere. *Journal of Geophysical Research*, 99(A7), 1994.
- M. Schulz and Lanzerotti. Lower hybrid acceleration and ion evolution in the supraauroral region. *Geophysical Research Letters*, 8(12):1253–1256, 1981.
- Nagendra Singh and C. B. Chan. Numerical simulation of plasma processes driven by transverse ion heating. *Journal of Geophysical Research: Space Physics*, 98(A7): 11677–11687, 1993.
- J.-P. St-Maurice and R. W. Schunk. Ion velocity distribution in the high-latitude ionosphere. *Reviews of Geophysics and Space Physics*, 17(1):99–134, 1979.
- R. M. Winglee. Mapping of ionospheric outflows into the magnetosphere for varying IMF conditions. *Journal of Atmospheric and Solar-Terrestrial Physics*, 62:527–540, 1999.
- X.-Y. Wu, J. L. Horwitz, G. M. Estep, Y.-J. Su, D. G. Brown, P. G. Richards, and G. R. Wilson. Dynamic fluid-kinetic (dyfk) modeling of auroral plasma outflow

- driven by soft electron precipitation and transverse ion heating. *Journal of Geophysical Research: Space Physics*, 104(A8):17263–17275, 1999.
- X.-Y. Wu, J. L. Horwitz, and J.-N. Tu. Dynamic fluid kinetic (dyfk) simulation of auroral ion transport: Synergistic effects of parallel potentials, transverse ion heating, and soft electron precipitation. *Journal of Geophysical Research: Space Physics*, 107(A10):SIA 5–1–SIA 5–26, 2002.
- W. Zeng, J. L. Horwitz, and J.-N. Tu. Characteristic ion distributions in the dynamic auroral transition region. *Journal of Geophysical Research: Space Physics*, 111(A4), 2006.
- M. Zettergren, K. Lynch, D. Hampton, J. Semeter, W. Peterson, P.-L. Blelly, M. Conde, Y. Lee, and A. Streltsov. Ionospheric plasma transport and loss in auroral current systems. 2013.